Thunderstorms in Norway

A climatological and a case study

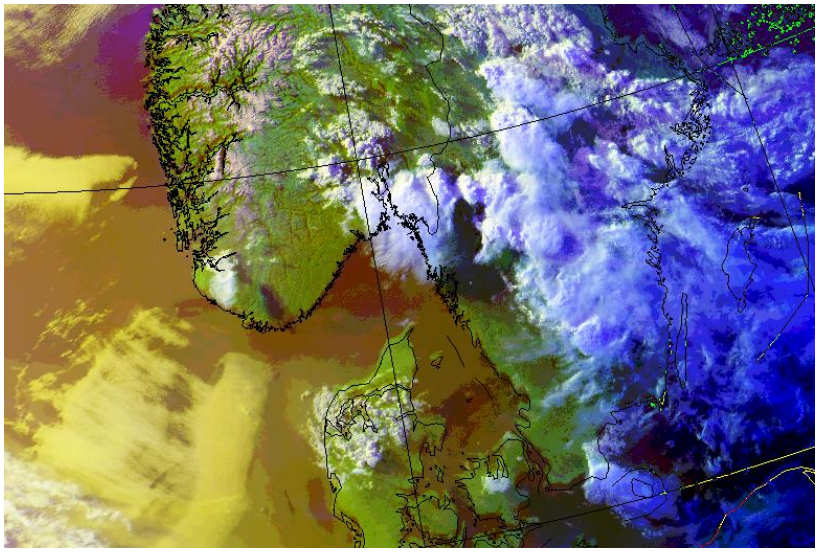

Master Thesis in Meteorology

Martin Granerød

June 1, 2011

UNIVERSITY OF BERGEN
GEOPHYSICAL INSTITUTE

The figure on the front page shows a visual satellite
image of Southern Scandinavia 19.06 UTC on 3 July 2009.

Obtained from Vegard Kristiansen.

This thesis is written in LaTeX, report style,
12 pt text and twosided format.

Acknowledgements

First of all I would like to express my gratitude to my supervisor Haraldur Ólafsson. He has given me inspiration and great support during this work. I would also say a special thanks for the opportunity to work with a topic that I have a big interest for. Haraldur also presented a poster for me in Vienna at the EGU meeting 2011.

During my work there are several persons who have helped me with precipitation data, synoptic observations, sounding data and satellite images. So thanks to Birgitte R. Furevik, Vegard Kristiansen, Trygve Aas and Jan-Inge Hansen from The Norwegian Meteorological Institute. Also thanks to Asgeir Sorteberg at The Geophysical Institute in Bergen, and Hans Bengtsson at The Swedish Meteorological and Hydrological Institute.

Thanks to my fellow students and friends for a unforgettable time at the Geophysical Institute, and for being supportive during this project. Especially, I would like to thank Gunnar Livik and Marius O. Jonassen for helping me with the modelling and other technical problems that have appeared during my work.

Finally, I would like to thank my great family and friends.

Abstract

The object of this thesis are thunderstorms in Norway. In the first part, the variability of thunderstorms in time and space is investigated, based on synoptic observations from 60 weather stations in Norway. An analysis of the annual and diurnal variability is carried out, and the long term tendency is explored on the basis of long time series from for five different locations. Some of the results are discussed with respect to the static stability of the atmosphere. There is high variability of the frequency of thunderstorms from one year to another, but there is no clear long term trend in the frequency of thunderstorms in Norway from 1957/58 to 2009. The interannual and diurnal variability confirm that thunderstorms in Southeast Norway have a continental character with a maximum activity in the late afternoon in the summer, while the west coast of Norway has a maritime character with thunderstorms observed through the whole year. The study shows that in the winter, the frequency of thunderstorms is greater in the northern part of the west coast of Norway than in the southern part of the west coast. In the autumn, the relative frequency is opposite: the southern part of the west coast has higher frequency than the northern part. This variability agrees with the frequency of low static stability. In the second part, the case of the 3 July 2009 thunderstorm in Oslo is investigated. The flow is simulated with The Weather Research and Forecasting model (WRF) with different configurations, including 7 microphysical parametrizations and 4 cumulus schemes. A predictability analysis is done for the best configuration. The 3 July case study shows that the convective precipitation is quite sensitive to the resolution, the microphysical parametrizations, the cumulus schemes and the initial data. This real case is described with respect to the temperature, moisture, convective available potential energy (CAPE) and convective inhibition (CIN). Trajectories are also calculated to find the origin of the airmasses. The predictability of the event is good in terms of prediction of the potential for convective precipitation, while the predictability of the high quantity and location of the precipitation is not as good. The 96 hour forecast gives a better forecast than the 72 hours forecast. The reason for this is traced back to a difference in temperature at levels between 600 hPa and 900 hPa over Kattegat.

Contents

Chapter 1

Introduction

Lightning strikes are a source of substantial damage and with increasing sensitivity of electronic infrastructures, the risk associated with thunder is increasing. Thunderstorms are often associated with very intense precipitation. Such events can have serious societal impacts. The importance of forecasting thunderstorms is therefore evident.

This study of thunder in Norway is composed of two parts. In the first part, the variability of thunderstorms in Norway is explored in time and space, based on observations from 60 weather stations. The second part presents a detailed study of a case of a convective afternoon summer thunderstorm in Southeast Norway, including numerical simulations with multiple configurations. There are only a few research papers on thunderstorms in Norway, Spinnangr (1941), Spinnangr (1942) and Knudsen (1974), but obviously, none of them has explored the variability in time and space of all the synoptic observations from 1957/58 to 2009.

In Chapter 2, some of the relevant theory for both the climatological and the case study is introduced. The data and observations that are used in this study is described in Chapter 3. The Weather Research and Forecasting Model(WRF) is described in Chapter 4.

The result of the variability analysis of thunderstorms in Norway, based on synoptic observations is shown in Chapter 5. The study includes the variability of thunderstorms in space, but also the annual and diurnal variability. Some of the results are discussed with reference to the static stability over parts of Norway.

In Chapter 6, the result of the detailed study of the thunderstorm event is shown

and discussed. One of the main focuses is the observed precipitation compared to the precipitation produced by the model. Different microphysical parametrizations and cumulus schemes are tested to see which of the configurations that gives the best result. A predictability analysis is also done in Chapter 7 to see how the forecast changes with different initializations. One GOOD forecast and one BAD forecast is found with 24 hours difference in the initialization. The BAD forecast is then traced back in time to find the difference between the BAD and the GOOD.

In Chapter 8 a summary is included. Future work is given in Chapter 9, and in the appendices, information of all the data is given together with a list that explains some of the acronyms used in this study.

Chapter 2

Theory

2.1 Cumulus convection

Different types of clouds have a quite different horizontal extent. A cumulus cloud have approximately a 0.5 - 10 km horizontal extent, and other types of clouds like the stratus clouds can have a horizontal extent of 100 km or more, if not always(Rogers and Yau, 1989). When there are lightnings and thunder involved, there is often a Cumulonimbus(CB) cloud present. The CB cloud is a large cumulus cloud formed by convection that can have a cloud top at 16 km height and can be 10 km or more in diameter (Rogers and Yau, 1989). The amount of energy in a CB cloud is huge, but due to difference in temperature and moisture in different places on the earth, the size of the clouds varies a lot. A typical CB cloud has a latent energy content of 6.3×10^{14}J (Rogers and Yau, 1989).

Clouds and precipitation is one of the most requested output from numerical weather prediction, but both have low predictability. Typical for a cumulus cloud is that it has generally a complex internal structure and they are generally a short lived individual rising towers. The rising towers of air are called thermals because of the ascending buoyant air inside them. Such vertically moving air in the atmosphere is referred to as convection. Rising thermals entrain("captures") environmental air and thus modify the cloud through mixing. A thermal is not in hydrostatic equilibrium, it is non-steady and highly turbulent (Holton, 2004).

2.1.1 First law of thermodynamics

The physics of a cloud is governed by the ideal gas law, Equation 2.1, and the first law of thermodynamics, Equation 2.2.

$$p = \rho RT \tag{2.1}$$

$$dq = du + dw \tag{2.2}$$

Here the R is the individual gas constant($287 JKg^{-1}K^{-1}$) for dry air, T is the temperature, p is the pressure and ρ is the density. The dq is the amount of heat change applied per unit mass of an air volume, du is the change in internal energy per unit mass and dw is the work done by/applied on the air parcel per unit mass. Setting the internal energy $du = c_v dT$ and the work done $dw = pd\alpha$, the first law of thermodynamic can be written as follows:

$$dq = c_v dT + pd\alpha \tag{2.3}$$

By differentiating the ideal gas law, Equation 2.1, when $\alpha = \frac{1}{\rho}$, leads to

$$pd\alpha + \alpha dp = RdT \tag{2.4}$$

By setting $c_v + R = c_p$ and assume the process is adiabatic, $dq = 0$. Then Equations 2.3 and 2.4 can be combined and written in an alternate form of the first law of thermodynamics:

$$c_p dT = \alpha dp \tag{2.5}$$

For moist air, the first law of thermodynamics can be written as follows:

$$c_p dT = \frac{RT}{p} dp + L dw_s \tag{2.6}$$

where w_s is the mixing ratio for moist air and L in the latent heat release.

2.1.2 Hydrostatic equilibrium

Hydrostatic equilibrium means that $\dfrac{dw}{dt} = 0$ and experiences no net force in vertical direction(Rogers and Yau, 1989), which means that the pressure gradient(buoyancy)

force equals the gravitational force, Equation 2.7.

$$\frac{\partial p}{\partial z} = -\rho g \tag{2.7}$$

Where ρ is dependent of both the moisture and temperature from the ideal gas law, Equation 2.1. In calculation of the atmosphere, the assumption of hydrostatic equilibrium is often made. As mentioned earlier, a rising thermal is in non-hydrostatic equilibrium, which means that there is a vertical acceleration and that moisture and temperature are important factors for the convection.

2.1.3 Skew-T diagram

A Skew-T diagram, Figure 2.1, is a commonly used thermodynamic diagram in meteorology. It is used for radiosonde plotting to give a vertical profile of the atmospheric condition. The Skew-T diagram is useful to evaluate the stability of the atmosphere.

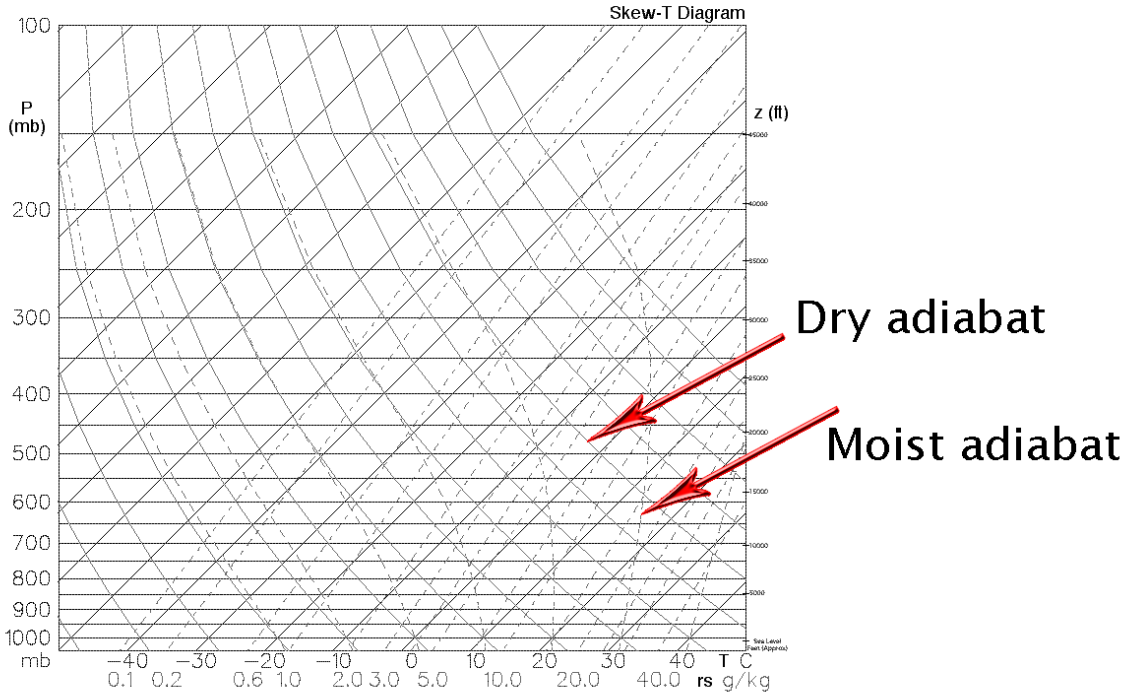

Figure 2.1: *Shows the Skew-T diagram that is often used in meteorology to present a vertical profile of the atmosphere. The temperature and moisture of a parcel in the atmospheric is plotted versus the pressure. The different lines are referred to the dry and moist adiabatic lines, the temperature and the moisture. Source: http://en.wikipedia.org/wiki/File:Skew-T.gif*

An upward moving parcel will eventually reach its convective condensation level(CCL), which is the height where the parcel is saturated by cooling through dry adiabatic lifting. If the parcel is lifted further, it will follow the moist adiabat and it may reach the level of free convection(LFC), which is the level where the parcel of saturated air becomes warmer than the surroundings. From that point, the parcel will rise freely without extreme help until the temperature of the surroundings become higher than the temperature of the parcel. This is called the equilibrium level. In general the CCL can be mixed by the lifted condensation level(LCL), but when the lifting occurs because of warming of the earth surface and not processes like e.g. orographic lifting, the CCL should be used instead of LCL(Haby, 2010).

For deep convective clouds the forced lifting is mostly due to free convection, but at the same time, the air can be lifted by orographic processes. Therefore the real condensation level lies between the lifted condensation level(LCL) and the convective condensation level(CCL) (Spinnangr, 1942).

2.1.4 Buoyancy

Buoyancy is the force that acts on the parcel vertically in response to density difference between the parcel and the surrounding air. When the buoyancy force is larger than the gravity force, the air is forced upwards. When the gravity force is larger than the buoyancy force, the air is forced downwards. The buoyancy force is essential for producing convective clouds. If the potential temperature is high, and there is a high water content in the atmosphere, the buoyancy force may be strong, and this can lead to deep convective clouds(Comet, 2002).

The potential strength of the updraft and downdraft can be estimated by using the Skew-T diagram. To find out whether there is positive or negative buoyant conditions in the atmosphere, the Lifted Index(LI) can be used. The LI can be found by lifting the parcel along the moist adiabat from its LCL to a level aloft. Then the temperature at this level is subtracted from the ambient temperature at LCL. Table 2.1 shows how the LI index indicates whether the parcel would rise or sink. A higher negative LI, indicates a higher potential strength in the updraft. Since the LI is calculated at only one level, the LI should only be used when referencing to the full sounding(Comet, 2002).

Table 2.1: *Table that shows how the lifted index(LI) indicates in which vertical direction(ascending/descending) the parcel would go.*

Positive LI	=	Negative buoyancy, Parcel would sink
Negative LI	=	Positive buoyancy, Parcel would rise

2.1.5 CAPE and CIN

The convective available potential energy(CAPE) and the convective inhibition(CIN) are two estimates that indicates whether convection will appear or not and can be found as integrals in the Skew-T diagram. For forecasters, the CAPE value is generally a more used parameter than CIN to predict summer showers.

CAPE measures the buoyant energy from the LFC and up to the equilibrium level, which is defined in Section 2.1.3. An estimated value of CAPE between 0-1000 J/kg are marginal for convection to occur. Estimated values between 1000 - 2500 J/kg support moderate convection, and estimated values higher than 2500 J/kg support strong deep convection (Wallace and Hobbs, 2006).

CIN is the energy required to lift the air parcel up to its LFC and over the capping inversion, which is a layer that prevent thunderstorms to occur. CIN can prevent convection if its value is high. For CIN values higher than 100 J/kg, there is unlikely for convection to occur(Wallace and Hobbs, 2006). Three mechanisms can destroy the capping inversion(Comet, 2002):
1: Heating of the surface
2: Moistening at low levels
3: Synoptic scale lifting, e.q a front passage.

Generally, thunderstorms are most likely to occur in the late afternoon due to maximum CAPE and minimum CIN in the early afternoon. Trentmann (2009) concluded with that the indices CAPE and CIN are useful features for forecasting the occurrence of convective precipitation, but the amount of precipitation does not seem to be correlated with these convection indices in the model simulations.

2.1.6 Stability of the atmosphere

There are different stability criteria for dry and moist air, and here the stability criteria for moist air are discussed.

The stability of the atmosphere can be seen from the actual temperature in a sounding on a Skew-T diagram. The lapse rate γ of the actual temperature determines the stability when it is compared to the lapse rate for the dry(Γ) and moist(Γ_s) adiabatic line, shown on the Skew-T diagram(Figure 2.1). There are 5 stability criteria for moist air:

a) Absolutely stable when $\gamma < \Gamma_s$
b) Saturated neutral when $\gamma = \Gamma_s$
c) Conditionally unstable when $\Gamma_s < \gamma < \Gamma$
d) Dry neutral when $\gamma = \Gamma$
e) Absolutely unstable when $\gamma > \Gamma$

When there is adiabatic vertical displacement of ascending air in an unstable atmosphere, a convective mixed layer is formed. This is called adiabatic mixing and it is typical for cumulus convection(Holton, 2004). Figure 2.2 shows a typical diurnal cycle of the boundary layer of the atmosphere on a warm summer day. The convective mixed layer is dominating during daytime. At night, there is a stable layer at lower levels. The residual layer above the stable layer is characterized by weak turbulence and pollutants remaining from the convective mixed layer.

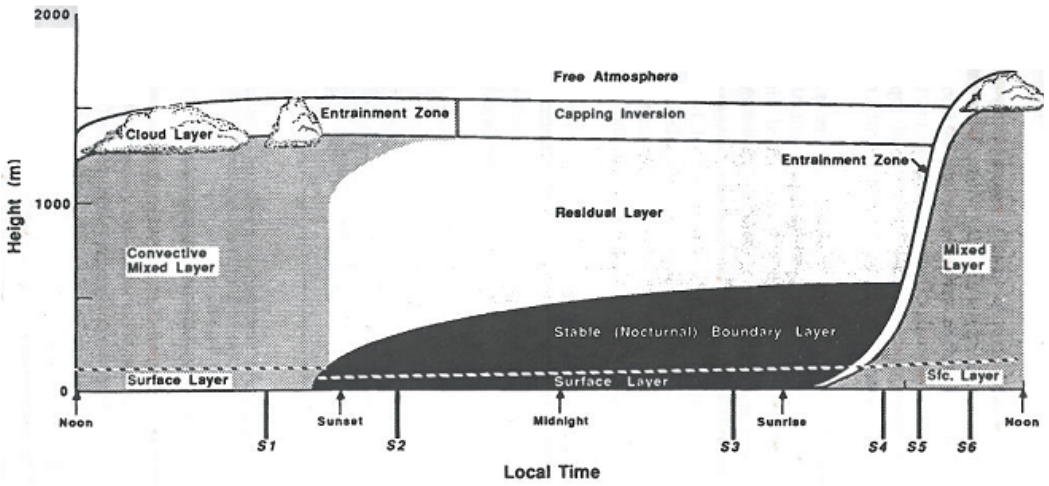

Figure 2.2: *Diurnal cycle of the boundary layer. the mixed layer start forming at S4 and continues to sunset. When a stable layer is forming close to the ground, and there is a residual layer over the stable layer. Source: Stull, R.B, An Introdution to boundary layer meteorology, page 11. (2009)*

2.1.7 The cumulonimbus cloud

If deep and moist convection is present, a cumulonimbus cloud(CB) is appearing. A schematic of a deep convective cloud is shown in Figure 2.3. The first condition for developing a CB cloud is an unstable environment. Like on a warm summer day with strong heating at the surface together with high moisture content of the atmosphere. Since there is warm rising air inside and below the cloud there has to be downdrafts on each side of it. When the thermal instability of the troposphere forms convective clouds, the vertical velocity is in the order of $10m/s$. Due to high vertical speed, the upward and downward currents are restricted to horizontal areas with diameters of several kilometres(Tuomi and Mäkelä, 2009).

The second stage is when precipitation from the cloud is present. When the gravity force of the hydrometeors is bigger than the upward buoyancy force, precipitation will start to fall. The magnitude of the precipitation loading depends on the amount of moisture and the updraft strength. The precipitation rate is also dependent on the moisture flux. When there is moisture flux over a wet surface, the precipitation rate will become higher than over a dry surface.(Yamada, 2008). The precipitation will contribute to downdraft of the air, and is the most important feature that affects the strength of the downward movement. It is not only the precipitation that contributes to downward acceleration. Evaporation of rain below the cloud base, entrainment of drier air at mid level and condensing of moisture inside the cloud contributes to further acceleration downward. Mid level moisture and the height where evaporation stops will also contribute to the downdraft(Comet, 2002).

When the cold downdraft reaches the surface, a gust front occurs and the convection cell is at the final stage of its life cycle. The strength of the downdraft will determine the wind speed at the gust front and the ability to trigger new cells. The propagation speed of the gust front depends on two things. The height of the front, and the temperature difference between the air behind and in front of the front(Comet, 2002). An anvil is also formed at the cloud top around the equilibrium level. This is because the temperature of the parcels that reach this height is lower that the surroundings, and the momentum will force the parcels back down. This leads to oscillations around the equilibrium level and the parcels will be forced to spread out. When the cloud is dominated by downdraft, it has reached the dissipation stage. The cool downdraft will cut of the inflow of warm air and the thunderstorm will dissipate rather quickly.

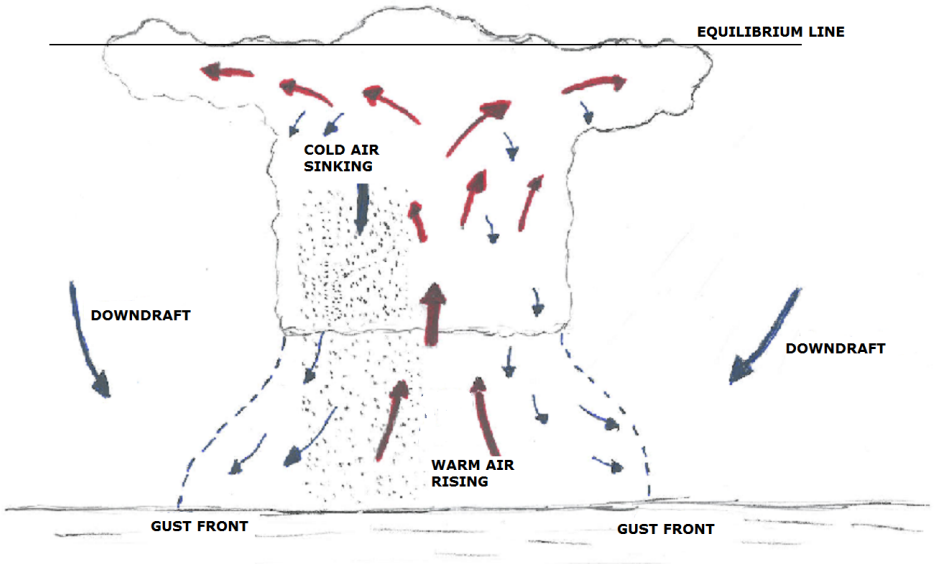

Figure 2.3: *A schematic on how the air moves in and around a convective cumulonimbus cloud. The updraft and downdraft are shown, but also the gust front and the equilibrium line.*

2.2 Thunderstorm variability

2.2.1 History

Prediction of convective afternoon summer showers are discussed in several studies in the 20th century. Some examples are given in the statements below.

Calwagen (1926) pointed out that the forecasting of summer showers was a synoptic problem, but the stability conditions of the atmosphere have to be known.

"We shall probably never be able to say exactly where the thunderstorms will occur."(Spinnangr, 1941)

"Forecasting severe thunderstorms is one of the most difficult tasks in weather prediction, due to their rather small spatial and temporal extension, and the inherent non-linearity of their dynamics and physics"(Orlanski, 1975).

"Numerical modelling has made substantial advances in the modelling of convective clouds and mesoscale convective system"(Hobbs, 1991).

"There is uncertainties of when and where the thunderstorm is going to hit. Better understanding of the physics and the dynamics is essential for better prediction"(Vaidya, 2007).

"Forecasting convective precipitation remains a challenge for current state-of-the-art numerical weather prediction models. In low mountain regions, small scale local flow systems induced by topography determine the timing and location of convection"(Trentmann, 2009).

There are several papers discussing if the annual number of thunderstorms have increased with the climate change. A study from Poland and a study from Germany(Bielec-Bkowska, 2003)(Kunz, 2009) concluded that the annual number of days with thunderstorms remain unchanged and no tendency were found over the last 50 years. There was also found that the synoptic situation had less influence on thunderstorm occurrence than usually suspected(Bielec-Bkowska, 2003). In both of these studies synoptic observations have been used. Due to large horizontal distance between the synoptic observations, all the thunderstorms are not captured in the observations. Unfortunately, there are not many research papers on variability of thunderstorms at higher latitudes.

2.2.2 Ingredients for thunderstorm development

According to Sumner (1988) a typical situation when thunder can be observed contain:

1. A supply of warm, moist air at low levels.
2. The presence of conditional or convective potential instability.
3. The existence of dry air aloft, important in aiding the release of available conditional or potential instability, and for evaporative cooling related to downdraughts.
4. Some trigger mechanism such as surface heating, low level convergence, or orographic lifting, which can cause the release of instability.
5. Pronounced shifts in wind speeds and/or direction between the surface and higher levels, wind shear.

A temperature difference on 38°C or more between the 500 and 1000 hPa levels indicates that a thunderstorm could appear(Knudsen, 1974). McIlveen (1992) claimed that the presence of ice particles in the upper part of the developing thundercloud, is fundamental to the Bergeron Findeisen process for the growth of precipitation sized particles. This is important with respect to electrical charge in the particle to produce

lightning.

2.2.3 Processes that contribute to thunderstorms in Norway

In Northern Europe, like Scandinavia, there are observed less thunderstorms than in Southern parts of Europe. This is related to the fact of the comparatively low levels of potential instability compared to South Europe(Delden, 2001). Spinnangr (1942) discussed the appearance of summer showers relative to the wind direction and concluded with that the strongest summer showers in Southeast Norway are observed when the air comes from south or east. In winter, the thunderstorm development is on the outer and middle districts to windward side of the mountains(Knudsen, 1974).

In Chapter 5, the variability of thunderstorms in Norway are shown. Below, some processes that contributes to these storms are listed.

1: The position of the mid latitude jet stream is in the middle and upper troposphere. Then warm subtropical air and cold polar air form lateral shear, this can lead to wave propagation on either side of the jet. This can again lead to vertical thermal waves that move horizontally. Then there can be simultaneous appearance of cold thermal troughs from the earth's surface and up to the middle atmosphere(Knudsen, 1974). This is known as frontogenesis where the atmosphere maintains in thermal wind balance by creating vertical circulation(Holton, 2004). The frontogenesis can provide the source of lift the air needs for upward movement(Delden, 2001). For occurrence of thunderstorm in this setting, the assumption that there are moisture available is done(Godske et al., 1957).

2: There are strong horizontal and vertical shear that strongly influences the air particles with turbulence at the cold front surface. Heat and moisture from the warm side of the front may penetrate the frontal zone and contribute to potential energy of the adjacent air. Also the warm air that is left behind the cold front in a shallow layer near the ground by the progressing cold front surface is mixed into the cold air by turbulent mixing. This can contribute to thermal convection(Knudsen, 1974).

3: Cold air that blows southwards towards Scandinavia forms a convective boundary layer. This is because of thermal convection, but turbulence caused by wind shear in the surface layer may be of some importance, specially in the initial stage. The thickness of the unstable air increases as the air moves southwards(Ólafsson and Økland, 1994). High cloud base temperature increases the amount of moisture enter-

ing the cloud(Cotton and Anthes, 1989), but higher temperature on the cloud base will weaken the updraft between the air and sea surface.

4: Other processes, like sea breeze circulation, orographic lifting and lee cyclogenesis of very humid and warm Mediterranean air are processes that could play a role in the formation of a thunderstorm(Delden, 2001).

2.3 Omega blocking

In the detailed case study in Chapter 6, the investigated thunderstorm event appear when a omega blocking event is present. Therefore some general information about the omega blocking is given below. The information in this section about omega blocking is from Comet (2009).

Figure 2.4 shows an idealized case of an omega block situation. The high pressure looks like the greek letter Ω, therefore it is called a omega blocking situation. The westerly flow is cut off by a blocking high pressure center. On each side of the high pressure there is a low pressure circulation(L1 and L2). When the westerly flow hits the first cyclonic circulation(L1) the inflow is split in two directions, equatorward and poleward. This creates the first deformation zone. South of the blocking high, there will also be produced a deformation zone. Here some of the air will go poleward and anticyclonic around the blocking height or the air will go cyclonically equatorward of the second cyclonic circulation(L2). On the eastern side of the system, the air will again form a westerly flow.

Typical weather situation for an omega block situation is that there is a warm high pressure on the poleward side of the jet stream. The western low typical produce more precipitation than the eastern low. This is because the eastern low is typically over land and the western low is typically over the sea and has more moisture supply. Omega blocks can hold for a long time and may cause severe flooding and drought.

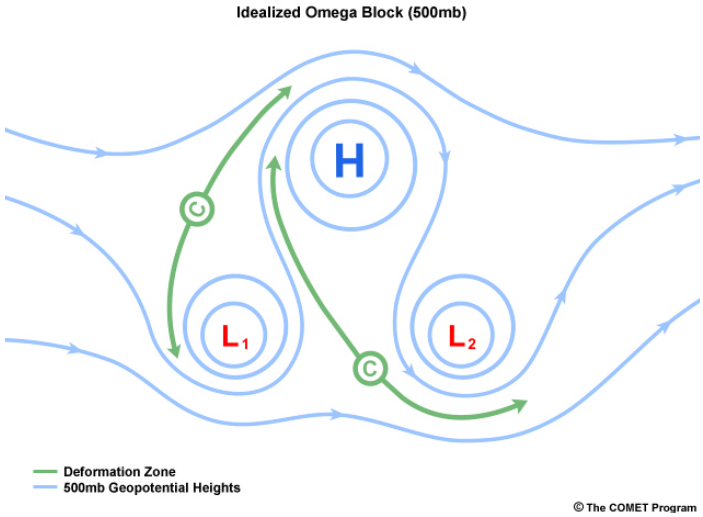

Figure 2.4: *An idealized Omega Blocking Event with one high pressure(H) and two low pressures(L). The source of this material is the Comet® Website at http://meted.ucar.edu/ of the University Corporation for Atmospheric Research, sponsored in part through cooperative agreements with the National Oceanic and Atmospheric Administration(NOAA), U.S. Department of Commerce(DOC). ©1997-2011 University Corporation for atmospheric research. All rights reserved.*

Chapter 3

Data

3.1 Observations

3.1.1 Observed precipitation

In this thesis, data from 338 weather stations are used to assess the accumulated precipitation that fell between 06 UTC on 3 July to 06 UTC on 4 July 2009. The observations are collected from `www.eklima.no`, which is a climate database of the Norwegian Meteorological Institute. See Appendix C for exact location and the amount of precipitation on all the stations.

The weather stations can be divided into three different types. There are the synoptic stations where observations of precipitation, clouds, wind, moisture, snow-depth, sight and weather type are made manually. Second there are the automatic stations, which usually consist of information about pressure, temperature, moisture, wind and precipitation. Both the synoptic stations and the automatic stations send information to the Norwegian Meteorological Institute 3-8 times every day, but some of the automatic stations transfer the data to The Norwegian Meteorological Institute every hour. The third type of station is the precipitation station that only measures the precipitation and snow depth manually at 06 UTC every day.

There are two types of precipitation gauges that measures precipitation. The recording and the non-recording. The non-recording is an open bucket. When the precipitation falls into it, an observer can manually observe how much precipitation there is in it. For the recording type, there are three types. The tipping bucket where the total precipitation can be measured by registration of the intensity of the tips. The weighing gauge that takes the weight of the water that has fallen into a bucket, and Optical

gauges that count the droplets of a defined volume.

3.1.2 Synoptic observations

The forecasting and analysis of thunderstorms can be seen from two different angles. The meteorological and the atmospheric electrical. Some research on the atmospheric electricity and thunderstorms has been done by Rott (1963). He made his thunderstorm warnings based on interpretation of characteristic features in the records of atmospheric electric potential gradient. In this thesis, the analysis is seen from the meteorological view, by using the easy accessible synoptic observations. Synoptic observations is very important, and due to these observations it is possible to do research on different weather phenomenon. In this case, thunderstorms.

Synoptic observations from 60 stations in Norway are used to map the variability of thunderstorms. The synoptic observations ww and w1/w2 are used to define the thunderstorm events, where ww is weather at present time of the observation, and w1/w2 is the weather since the last main observation. When ww = 29 or from 91 - 99, thunder is observed at the observation time. When w1/w2 = 9, thunder has been observed since the last main observation. A description of every ww and w1/w2 value is given in Table 3.1, in the last part of this chapter.

A study by Delden (2001), the observation values ww = 13 and 17 are not taken into account. Therefore in thesis, these values are excluded. Below there is an explanation of why these values are omitted. The value ww = 13 is lightning visible, but no thunder heard, and lightning is much more visible during night than during sunlight. The value ww = 17 is thunder heard, but no precipitation observed. The observer can have a workplace inside a soundproof building and other nearby noise could interrupt the observer in hearing the thunder. Some observers have also a better hearing than others.

The observations are generally taken 4 times a day, 00 UTC, 06 UTC, 12 UTC and 18 UTC. For some stations there are not observations at 00 UTC. This means that w1/w2 at 06 UTC will cover for the missing ww observation at 00 UTC at these stations.

3.2 Convection resolving models

In this thesis, reanalysis data from The European Centre for Medium-Range Weather Forecasts(ECMWF) is used[1]. Trentmann (2009) has shown that for convective situations in low mountain terrain, the WRF model underestimates the amount of precipitation compared to gauge adjusted radar observations. Trentmann (2009) also shown that the use of ECMWF data in the WRF simulations consistently gives less precipitation compared to simulations that uses data from The National Centers of Environmental Prediction(NCEP)[2].

Studies on convective events in convection resolving models indicates a significant impact of initial and lateral boundary conditions on the simulation of convective cloud precipitation(Hohenegger, 2006)(Didone, 2007)(Wulfmeyer, 2006). Both the assimilation of water vapour and the assimilation of radar data can improve forecasts by triggering convection in the model at the right time and location, and therefore reduce the errors in the initial filed(Grzeschik et al., 2008)(Leuenberger and Rossa, 2007).

3.3 HYSPLIT trajectory model

For some of the trajectories calculated in this thesis, the HYbrid Single-Particle Lagrangian Integrated Trajectory(HYSPLIT) model is used.(Draxler and Hess, 1997). This model can calculate simple trajectories, but can also be used for complex dispersion and deposition simulations. When running the model, gridded meteorological data is used on one of three different projections. The different projections are Polar, Mercator or Lambert. The model can be used directly on the Internet and it can be installed locally as well.

The HYSPLIT model has a long history. The first version was developed by Draxler and Taylor (1982). At this time the rawinsonde observations were used. A rawinsonde is a radiosonde that also measures wind speed and direction. First in HYSPLIT_3 (Draxler, 1992), the rawinsonde observations were replaced by gridded meteorological data from analysis or numerical weather prediction model. Some pre-processing of this data are required before the HYSPLIT model can run. Several features have been added to the model since then.

The model uses a terrain following σ coordinate system. Equation 3.1 expresses

[1] `http://www.ecmwf.int/research/era/do/get/index`
[2] `http://www.esrl.noaa.gov/psd/data/gridded/reanalysis/`

an equation for the vertical coordinate, σ.

$$\sigma = \frac{Z_{top} - Z_{mslp}}{Z_{top} - Z_{gl}} \tag{3.1}$$

Z_{top} is the top of the atmosphere and Z_{mslp} is the height of the mean sea level pressure. And Z_{gl} is the height of the ground level. All the heights are expressed relative to the mean sea level. A minimum of information the model requires to run is the horizontal wind components(U and V), Temperature(T), height(Z) or Pressure(P) and the pressure at the surface(P_0). In most circumstances the gridded meteorological data will contain a vertical motion field(W).

When the basic meteorological data have been processed and interpolated to the inertial model grid, trajectories can be computed. The path of a particle is computed from the average of the three dimensional velocity vectors for the initial position $P(t)$ and the first guess position $P'(t + \Delta(t))$. Equation 3.2 express the first guess, while Equation 3.3 express the final position to the air parcels.

$$P'(t + \Delta(t)) = P(t) + V(P, t)\Delta(t) \tag{3.2}$$

$$P(t + \Delta(t)) = P(t) + \frac{V(P, t) + V(P', t + \Delta(t))\Delta(t)}{2} \tag{3.3}$$

Meteorological reanalysis data from NCEP/NOAA[3] are used for trajectory calculations in this thesis and the vertical motion is calculated by the HYSPLIT model itself.

The resolution in the horizontal grid system is designed to be identical to that of the meteorological data that is used, which is $2.5^\circ * 2.5^\circ$ latitude/longitude for the NCEP data. The vertical resolution is decreasing away from the surface and has approximately 20th levels.(Draxler and Hess, 1997)

3.4 RIP4

To visualize the gridded data from the WRF model, RIP4[4] is used. RIP4 stands for Read, Interpolate and Plot. This is a Fortran program that use NCAR Graphics

[3] `http://www.ncep.noaa.gov/`

[4] `http://www.mmm.ucar.edu/mm5/documents/ripug_V4.html`

routines for the purpose of visualizing output from gridded meteorological data sets, primarily from mesoscale data sets.

Table 3.1: *Explanations for the different synoptic weather observation codes used in this study. The weather at present time(ww) at the observation and the weather since last main observation(w1/w2) are shown. Source: The Norwegian Meteorological Institute.*

Code	Description	General description
w1/w2 = 9	Thuderstorm observed with or without precipitation	
ww = 13	Lightning visible, but no thunder heard.	
ww = 17	Thunder heard during the last 10 to 15 minutes, but no precipitation observed at the station.	
ww = 29	Thunderstorms with or without precipitation.	Showers.
ww = 91	Light rain.	Precipitation at the observation time. Observed thunder during the last hour, but not during the last 10-15 minutes.
ww = 92	Middle or strong rain.	
ww = 93	Light snowfall, sleet or hail.	
ww = 94	Middle or strong snowfall, sleet or hail.	
ww = 95	Light or middle thunderstorm, with rain, sleet or snowfall, but not hail.	Precipitation at observation time. Thunderstorm at the observation time, that means during the last 10-15 minutes.
ww = 96	Light or middle thunderstorm with hail.	
ww = 97	Heavy thunderstorm with rain, sleet or snow, but not hail.	
ww = 98	thunderstorm in a dust-/sandstorm.	
ww = 99	Heavy thunderstorm with hail.	

Chapter 4

The Weather Research and Forecasting Model

In this thesis The Weather Research and Forecasting Model(WRF)[5] is used to simulate a thunderstorm that happened on 3. July 2009 over Southeast Norway. To give a description of this model, information from Skamarock et al. (2008) is used if nothing else is stated.

4.1 The WRF model

The WRF model is a numerical system designed for both research and operational weather forecasting. The development of WRF is a cooperation of different agencies aiming to provide a next generation mesoscale forecast model and data assimilation that also accelerates the transfer of research into operations. The collaboratives are the National Center for Atmospheric Research (NCAR), the Mesoscale and Microscale Meteorology Division, the National Oceanic and Atmospheric Administration's (NOAA), National Centers for Environmental Prediction (NCEP), The Earth System Research Laboratory(ESRL), The Center for Analysis and Prediction of Storms(CAPS) at The University of Oklahoma, and the Federal Aviation Administration(FAA), with the participation of university scientists. The WRF model can be used for a brand spectrum of research, such as of different parametrizations, regional climate simulations and idealized flows.

The different components of WRF can be seen in Figure 4.1. In the WRF software infrastructure, the information that is needed to satisfy the dynamic solvers before the model can run is accumulated. In the dynamic solver component, there are two

[5] `http://www.wrf-model.org/index.php`

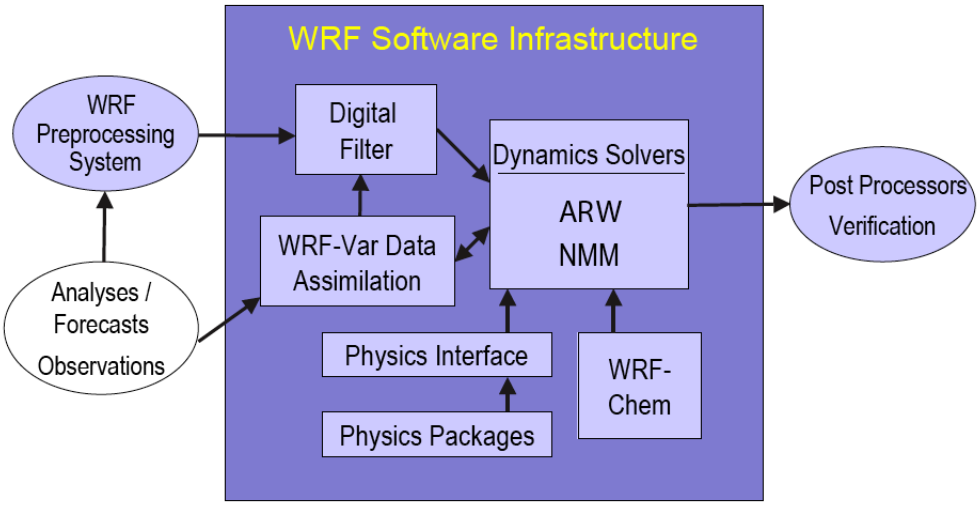

Figure 4.1: *WRF system components(Skamarock et al., 2008).*

types: the advance research(ARW) solver developed from NCAR and the nonhydrostatic mesoscale model(NMM) solver developed from NCEP. The ARW can be run for an idealized case or a real data case. In this thesis, a real case is investigated. When the dynamic solver is satisfied the WRF model can run, and the output can be simulated graphically in the Read/Interpolate/Plot program(RIP4)[6].

4.1.1 Governing equations

The ARW takes the non-hydrostatic Euler equations into account. These equations use the terrain following hydrostatic pressure vertical coordinate η(Laprise, 1992). η is defined as:

$$\eta = (p_h - p_{ht})/\mu \quad \text{where} \quad \mu = p_{hs} - p_{ht} \tag{4.1}$$

where p_h is the hydrostatic component of the pressure, p_{hs} is the value of the pressure at the surface and p_{ht} is the value at the top boundary. This coordinate system is called a mass vertical coordinate where η varies from 1 at the surface and 0 at the top boundary. Figure 4.2 shows the vertical coordinate system. The flux form variables can be written as:

[6] `http://www.eas.slu.edu/CIPS/TUTORIALS/RIP.pdf`

$$\mathbf{V} = \mu\mathbf{v} = (U, V, W), \quad \Omega = \mu\dot{\eta}, \quad \Theta = \mu\theta \tag{4.2}$$

where $\mathbf{v} = (u, v, w)$ are the covariant velocities in 3 dimentions. $\omega = \dot{\eta}$ is the contravariant "vertical" velocity. θ is the potential temperature. $\mu(x, y)$ represent the mass per unit area within the column at (x,y). In ARW, the non-conserved variables, such as the the pressure(p), the geopotential($\phi = gz$) and the inverse density($\alpha = 1/\rho$) are appearing in the governing equations.

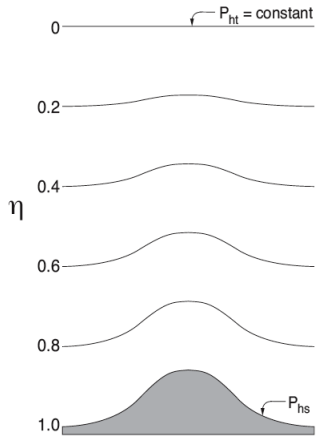

Figure 4.2: *The η vertical coordinate system in the WRF ARW dynamic solver. (Skamarock et al., 2008)*

The flux form Euler equations can then be written as:

$$\partial_t U + (\nabla \cdot \mathbf{V}_u) - \partial_x(p\partial_\eta\phi) + \partial_\eta(p\partial_x\phi) = F_U \tag{4.3}$$

$$\partial_t V + (\nabla \cdot \mathbf{V}_v) - \partial_y(p\partial_\eta\phi) + \partial_\eta(p\partial_y\phi) = F_V \tag{4.4}$$

$$\partial_t W + (\nabla \cdot \mathbf{V}_w) - g(\partial_\eta p - \mu) = F_W \tag{4.5}$$

$$\partial_t \Theta + (\nabla \cdot \mathbf{V}\theta) = F_\Theta \tag{4.6}$$

$$\partial_t \mu + (\nabla \cdot \mathbf{V}) = 0 \tag{4.7}$$

$$\partial_t \phi + \mu^{-1}[(\mathbf{V} \cdot \nabla\phi) - gW] = 0 \tag{4.8}$$

Which are prognostic equations. The terms on the right hand side(F_U, F_V, F_W and

F_θ) in Equations 4.3 to 4.6 represent the forcing terms from the model physics, turbulent mixing, spherical projections and the earth rotation. We also have the diagnostic relation for the equation of state(Equation 4.9), and the inverse density(Equation 4.10)

$$p \equiv p_0(R_d\theta/p_0\alpha)^\gamma \tag{4.9}$$

$$\partial_\eta\phi = -\alpha\mu \tag{4.10}$$

The subscripts in Equation 4.3 to 4.10 means the differentiations:

$$\nabla \cdot \mathbf{V}a = \partial_x(Ua) + \partial_y(Va) + \partial_z(\Omega a) \tag{4.11}$$

and

$$\mathbf{V} \cdot \nabla a = U\partial_x a + V\partial_y a + \Omega\partial_\eta a. \tag{4.12}$$

Here, a is a variable. R_d is the gas constant for dry air, p_0 is a reference pressure and $\gamma = c_p/c_v$ where c_p is the heat capacity of dry air at constant pressure and c_v is the heat capacity of dry air at constant voulme. Equation 4.9 and 4.10 are diagnostic equations.

If moisture is included, as it is for convection, Equation 4.1 can be written as:

$$\eta = (p_{dh} - p_{dht})/\mu_d, \tag{4.13}$$

where μ_d is the mass of dry air within the column and p_{dh} and p_{dht} is the hydrostatic pressure of the dry atmosphere and the hydrostatic pressure at the top of the dry atmosphere. Then, the variables from Equation 4.2 can be written as:

$$\mathbf{V} = \mu_d\mathbf{v} = (U, V, W), \quad \Omega = \mu_d\dot{\eta}, \quad \Theta = \mu_d\theta \tag{4.14}$$

When using these definitions, the moist Euler equations can be written as:

$$\partial_t U + (\nabla \cdot \mathbf{V}_u) + \mu_d\alpha\partial_x p + (\alpha/\alpha_d)\partial_\eta p\partial_x\phi = F_U \tag{4.15}$$

$$\partial_t V + (\nabla \cdot \mathbf{V}_v) + \mu_d\alpha\partial_y p + (\alpha/\alpha_d)\partial_\eta p\partial_y\phi = F_V \tag{4.16}$$

$$\partial_t W + (\nabla \cdot \mathbf{V}_w) - g[(\alpha/\alpha_d)\partial_\eta p - \mu_d = F_W \tag{4.17}$$

$$\partial_t \Theta + (\nabla \cdot \mathbf{V}\theta) = F_\Theta \tag{4.18}$$

$$\partial_t \mu_d + (\nabla \cdot \mathbf{V}) = 0 \tag{4.19}$$

$$\partial_t \phi + \mu_d^{-1}[(\mathbf{V} \cdot \nabla\phi) - gW] = 0 \tag{4.20}$$

$$\partial_t Q_m + (\nabla \cdot \mathbf{V} q_m) = F_{Q_m} \tag{4.21}$$

The diagnostic relation for the equation of state is now:

$$p = p_0(R_d\theta_m/p_0\alpha_d)^\gamma \tag{4.22}$$

and for the inverse density:

$$\partial_\eta \phi = -\alpha_d \mu_d \tag{4.23}$$

Here the $\alpha = \alpha_d(1 + q_v + qc + q_r + q_i + ...)^{-1}$, where the indexes are mixing ratios for water vapour, cloud, rain and ice. The $Q_m = \theta(1 + (R_v/R_d)q_v) \approx \theta(1 + 1.61q_v)$ and $Q_m = \mu_d q_m$, where $q_m = q_v, q_c, q_r, q_i$.

In the final form of the equations(not shown), perturbation variables are defined to reduce truncation errors, and effects like map projection and Coriolis are taken into account.

4.1.2 Initial conditions

WPS is the WRF model preprocessing system. Inside WPS, the model domains are defined and the static files are created from 2D terrestrial data. WPS also handles the interpolating of meteorological data to the model domain. The WPS defines a physical grid that includes projection, location, number of grid points and grid distances and interpolate the static field to its domain. The WPS horizontally interpolates the meteorological data onto the projected grid. Information of the atmosphere in 3D is the output from WPS at different times. This will be sent into the ARW. This data contains fields like temperature, relative humidity and the horisontal components of momentum, but also other fields are also included. Then the ARW real-data processor interpolates vertically downwards for every grid column.

4.1.3 Boundaries

The lateral boundary conditions specified in the outer coarse grid is split into two zones: the specified zone and the relaxation zone. The specified zone has the information from the WPS, which have information about horizontal wind components, potential temperature, humidity and perturbation fields that are given on all four sides of the coarse domain. The relation zone is where the model is nudged or relaxed towards the large scale field.

There can be smaller domains inside the coarse(parent) domain, and this is called nested grids. The nested grid have their information from the parent domain.

4.1.4 Discretization

In the WRF ARW solver, a Arakawa C grid staggering discretization is used, shown in Figure 4.3. The mass and velocity points have a half grid length between them. The Θ is located at the mass points and the wind components u, v and w are located at the u, v and w points. The pressure p and the inverse density α are computed at mass points as diagnostic variables. The geopotential is defined at the w points, and the model has a constant horizontal grid length, Δx and Δy.

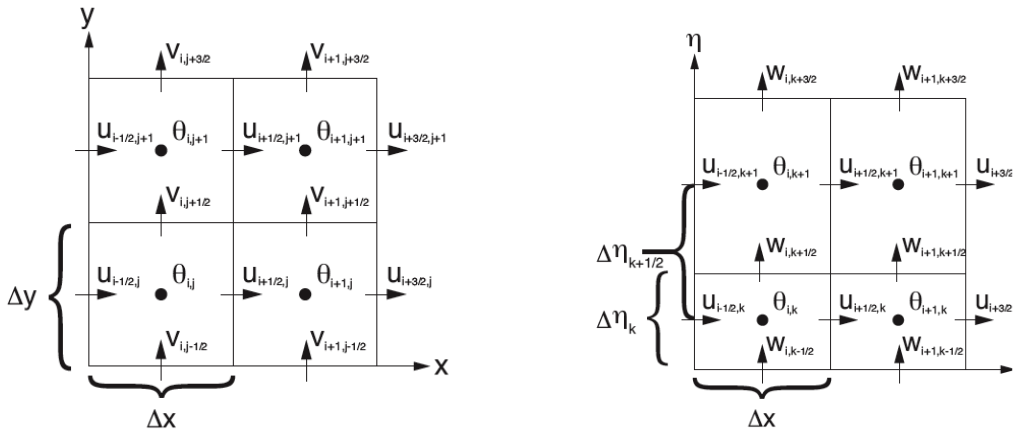

(a) *WRF ARW horizontal grid.* **(b)** *WRF ARW vertical grid.*

Figure 4.3: *The horizontal and vertical grid in the ARW dynamic solver for the Arakawa C grid staggering, (Skamarock et al., 2008).*

Table 4.1: *A overview of the microphysical parametrizations in the WRF model(Skamarock et al., 2008).*

Scheme	Number of moisture variables	Ice phase processes	Mixed phase processes
Kessler	3	N	N
Purdue Lin	6	Y	Y
WSM3	3	Y	N
WSM5	5	Y	N
WSM6	6	Y	Y
Eta GCP	2	Y	Y
Thompson	7	Y	Y

4.1.5 Stability and time split

WRF ARW uses a time split integration scheme because of the variable wavelength of the atmospheric waves. The frequency modes are split into a high frequency modes and a low frequency mode. The high frequencies usually need shorter time step than the stable low frequency part. The time split method, which are explicit numerical schemes is used on the high frequency modes to improve computational efficiency. For low frequency wavelength, the third order Runge-Katta time integration scheme is used. They are both limited by the Courant number $u\Delta t/\Delta x$.

4.2 Microphysical schemes

The microphysics in the WRF model include resolved water vapour, cloud and precipitation processes. In the ARW version, microphysics are taken as an adjustment process at the end of every time step to have the final saturation of every time step taken into account. Table 4.1 shows a summary of the parametrizations, including number of moisture variables and whether ice phase and mixed phase processes are included. Mixed phase processes mean processes involving both water and ice. For convective and icing situations, the mixed phase schemes should be used for grid sizes less than 10 km. A description of all the seven different schemes used in this study is given below.

Kessler scheme(Kessler, 1969): A warm cloud scheme that takes water vapour, cloud water and rain into account. The production, fall, evaporation of rain, the growth, autoconversion of cloud water and the production of cloud water from condensation are the included microphysical processes.

Purdue Lin scheme(Lin et al., 1983)(Rutledge and Hobbs, 1984): This scheme has six types of moisture variables. Water vapour, cloud water, rain, cloud ice, snow and graupel. It also includes saturation adjustment and ice sedimentation. This scheme is a often used scheme for research studies.

WRF single moment 3-class(WSM3-scheme)(Hong et al., 2004)(Hong and Lim, 2006)(Dudhia, 1989): This scheme predics three hydrometers, vapour, cloud water/ice and rain/snow. This scheme do not allow supercooled water to exist. Assuming cloud water and rain at temperatures above freezing level and cloud ice and snow at temperatures below freezing level. A diagnostic relation is used for ice number concentration that is based on ice mass content rather than temperature. It is considered to be an efficient scheme for the inclusion of ice processes.

WSM5 and WSM6 -scheme(Hong et al., 2004)(Hong and Lim, 2006)(Dudhia, 1989): Same as WSM3-scheme, but WSM5 allows supercooled water to exist. It has also a gradual melting of snow falling below the freezing line, and the ice and water saturation are separately treated. The WSM6 scheme is the same as WSM5, but it also takes graupel into account.

Eta grid-scale Cloud and precipitation scheme[7]. This scheme predicts change in water vapor and total condensate in the forms of cloud water, rain, cloud ice, and precipitation in the forms snow, sleet or graupel.

Thompson scheme(Thompson et al., 2004): This is a bulk microphysical parametrization that incorporates a large number of improvements to both physical processes and computer coding.

4.3 Cumulus schemes

The cumulus schemes, Table 4.2, are responsible for the sub-grid scale effects of convective and shallow clouds. In these schemes, the unresolved updrafts and downdrafts and the compensating motion outside the clouds are represented. All of these schemes influence the convective component of surface rainfall. Theoretically, cumulus schemes are only valid for a grid size larger than 10 km because of the latent heat release in convective columns. Generally, these schemes should not be used on a grid size smaller than 5 km. A description of all the four schemes used in this study is given below.

[7] `http://meted.ucar.edu/nwp/pcu2/etapcp1.htm`

Table 4.2: *An overview of the cumulus schemes in the WRF model(Skamarock et al., 2008).*

Scheme	Cloud detrainment	Type of scheme	Closure
Kain-Fritsch	Y	Mass flux	CAPE removal
Betts-Miller-Janjic	N	Adjustment	Sounding adjustment
Grell-Devenyi	Y	Mass flux	Various
Grell-3	Y	Mass flux	Various

Kain-Fritsch scheme: The modified version of the Kain (2004) scheme is based on the Kain and Fritsch (1990) scheme and the Kain and Fritsch (1993) scheme, but has been modified later on. This scheme takes moist updrafts and downdrafts into account, and includes the effects of detrainment, entrainment and relatively simple microphysics.

Betts-Miller-Janjic scheme: This scheme is derived from the Betts-Miller convective adjustment scheme(Betts, 1986)(Betts and Miller, 1986). In this scheme, the deep convection profiles and the relaxation time are variables and depend on the cloud efficiency, that is a non dimensional parameter that characterizes the convective regime(Janjic, 1994). The cloud efficiency depends on the entropy change, precipitation and mean temperature of the cloud.

Grell-Devenyi scheme(Grell and Devenyi, 2002): The scheme is all mass flux type scheme, but with differing updraft and downdraft entrainment and detrainment parameters, and precipitation efficiencies. The dynamic control closure is based on convective available potential energy CAPE, low level vertical velocity or moisture convergence. The moisture convection balances the cloud rainfall to the integrated vertical advection of moisture. This scheme is an ensemble cumulus scheme where multiple cumulus schemes and variants are run inside each grid. Then a mean is taken of all the runs to give a feedback to the model.

Grell3- scheme: It has a lot common with Grell-Devenyi scheme, but the quasi-equilibrium approach is no longer included among the ensemble members. The scheme is distinguished from other cumulus schemes by allowing subsidence effects to be spread to neighbouring grid columns, making the method more suitable to grid sizes less than 10 km.

4.4 Model setup

In Figure 4.4, the 4 domains used in this study are shown with 27 km, 9 km, 3 km and 1 km resolution. The simulation for the case study starts at 00 UTC on 2 July to 00 UTC on 5 July.

For the predictability analysis, the largest domain with resolution on 27 km is used. The model starts at 00 UTC on 28 June and ends at 00 UTC on 5 July.

For all the simulations, data from The European Centre for Medium Range Weather Forecast(ECMWF) is use, which have a temporal resolution of 6 hours and a 0.5° horizontal resolution.

Figure 4.4: *The domains with resolution on 27 km, 9 km, 3 km and 1 km used in the simulations with the WRF model.*

Chapter 5

Thunderstorms in Norway in Time and Space

The first part of this chapter shows the variability of thunderstorms in time and space over Norway based on available synoptic observations, discussed in Chapter 3. The second part shows time series of thunderstorm variability for six different places: Oslo, Bergen, Flesland, Vigra, Bodø and Karasjok, based on data from 1957/1958 to 2009. In the third part a discusion of the annual and diurnal variability for these places is shown, and some of the results are discussed with reference to the static stability over Norway. In the last part, there is a general discussion and a conclusion of the variability of thunderstorms in Norway.

5.1 Variability in time and space

The location of all the weather stations discussed in this text is shown in Figure 5.1. For exact location of all the stations used, see Appendix A. In Figure 5.2, all the observations are used to show the frequency of thunderstorms in Norway. The dark blue column shows the thunderstorms observed from January to April, the blue column shows the thunderstorms observed from May to August and the green column shows the thunderstorms observed from September to December. These three periods are chosen because the thunderstorms are formed in different ways throughout the year. Between January and April, the thunderstorms are mostly associated with extra-tropical cyclones, but cold air outbreaks may exist. From May to August, afternoon convection and extra-tropical cyclones have a big influence on the appearance of thunderstorms, and from September to December most of the thunderstorms appear because of extra-tropical cyclones.

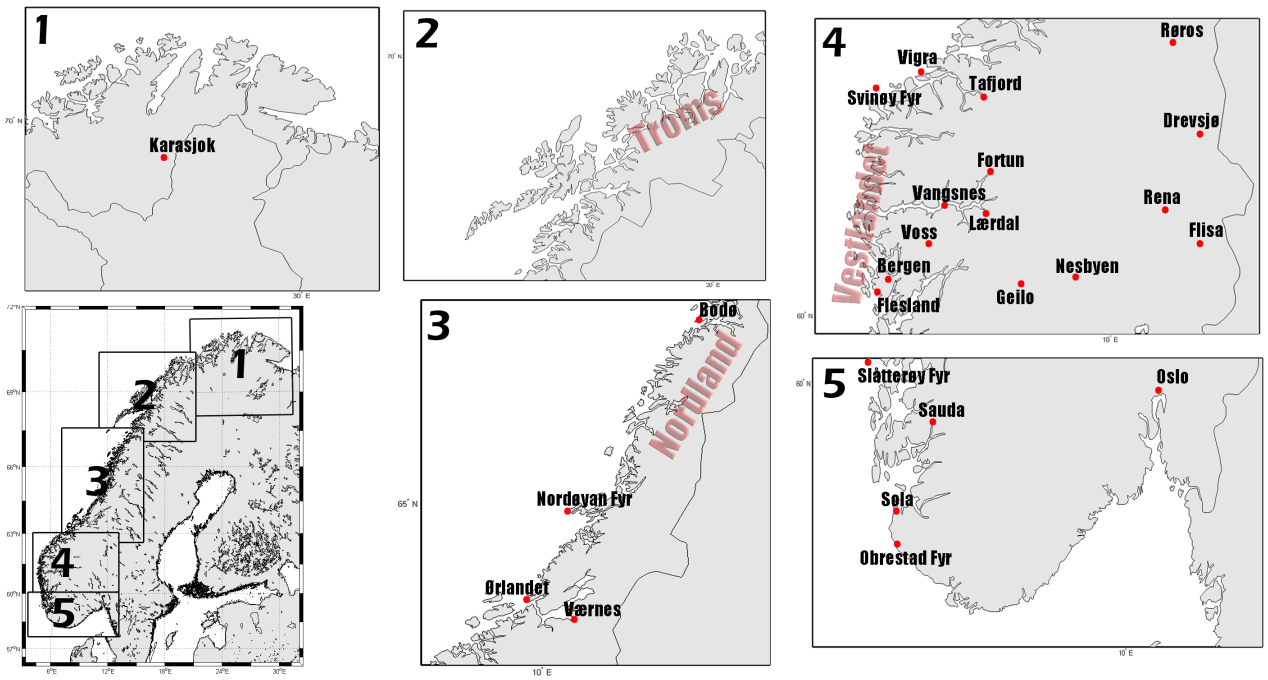

Figure 5.1: *A map that shows the location of all the stations with synoptic observations discussed in this study.*

There are several interesting factors to observe from Figure 5.2. The observations at the northern most latitudes are shown in Figure 5.2a and 5.2b. Generally, the locations in Troms and Nordland have more observations of thunderstorms than further north. In coastal areas there are only few thunderstorms observed throughout the whole year. Inland, the highest frequency is observed between May and August.

Locations in the central part of Norway, Figure 5.2c, have a higher frequency of thunderstorm observations than locations further north. At the inland stations, Røros and Værnes, thunderstorms are relatively common between May and August, and less common from January to April and September to December. In Røros, there are no observations of thunderstorms from January to April and September to December. In coastal areas there is a relatively high frequency of thunderstorm observations throughout the whole year. There are fewer thunderstorms observed at the lighthouses Svinøy Fyr and Nordøyan Fyr than at Vigra, that is located closer to the mountains.

For stations in the fjords, the observations in the Central part of Norway and on Vestlandet show similar patterns. Tajord, Vangsnes, Lærdal and Fortun have from January to April and September to December very few observations of thunderstorms, and most of the thunderstorms appear between May and August.

On Vestlandet, Figure 5.2d, there is a high frequency of thunderstorms throughout the whole year. Generally there is observed a higher number of thunderstorms between September and December, than from January to April and May to August. In Voss, there are in general observed few thunderstorms, and the highest frequency is observed from May to August. So the tendency in Voss is quite like the tendency in the fjords further north. In the coastal areas there are observed less thunderstorms at the lighthouse Slåtterøy Fyr and Flesland than in Bergen that is located closer to the mountains. This pattern is the same that was observed for Central-Norway, but in general, the frequency of observed thunderstorms is higher on Vestlandet.

Stations southwest on Vestlandet are shown in Figure 5.2e. Stations located near the coast, like Sola and Obrestad Fyr has a high number of thunderstorms from May to August and September to December. Between January and April the frequency is lower. An interesting location is Sauda, which is located in a fjord. Compared to locations inside fjords further north on Vestlandet, Sauda has not the same pattern. In Sauda there are observed more thunderstorms throughout the whole year, and not just between May and August.

In Figure 5.2e and 5.2f, the stations in South and Southeast Norway are shown. For the inland stations in the Southeast, like Drevsjø, Flisa, Rena, Nesbyen and Geilo, there is a relatively high number of thunderstorms observed between May and August. Between September and December there are some observations of thunderstorms, and from January to April there are very few observations of thunderstorms in this area. Closer to the coast in Southeast Norway, the absolute highest frequency of thunderstorms is still between May and August. There are almost none observations of thunderstorms from January to April, and from September to December there are some observations of thunderstorms. So the main difference between mountainous areas and locations closer to the coast is the number of thunderstorms, and not the trend throughout the year. In general, there are observed fewer thunderstorms in the mountainous areas than closer to the coast.

To give a better overview of the thunderstorm variability in Norway in time and space, all the data from Figure 5.2 is projected onto a regular horizontal grid. The Natural Neighbour interpolation method by Sibson (1981) is used, which is based on the Voronoi tessellation. The result is presented for individual seasons in Fig 5.3 to 5.5. In these figures the number of thunderstorms is divided by the total number of

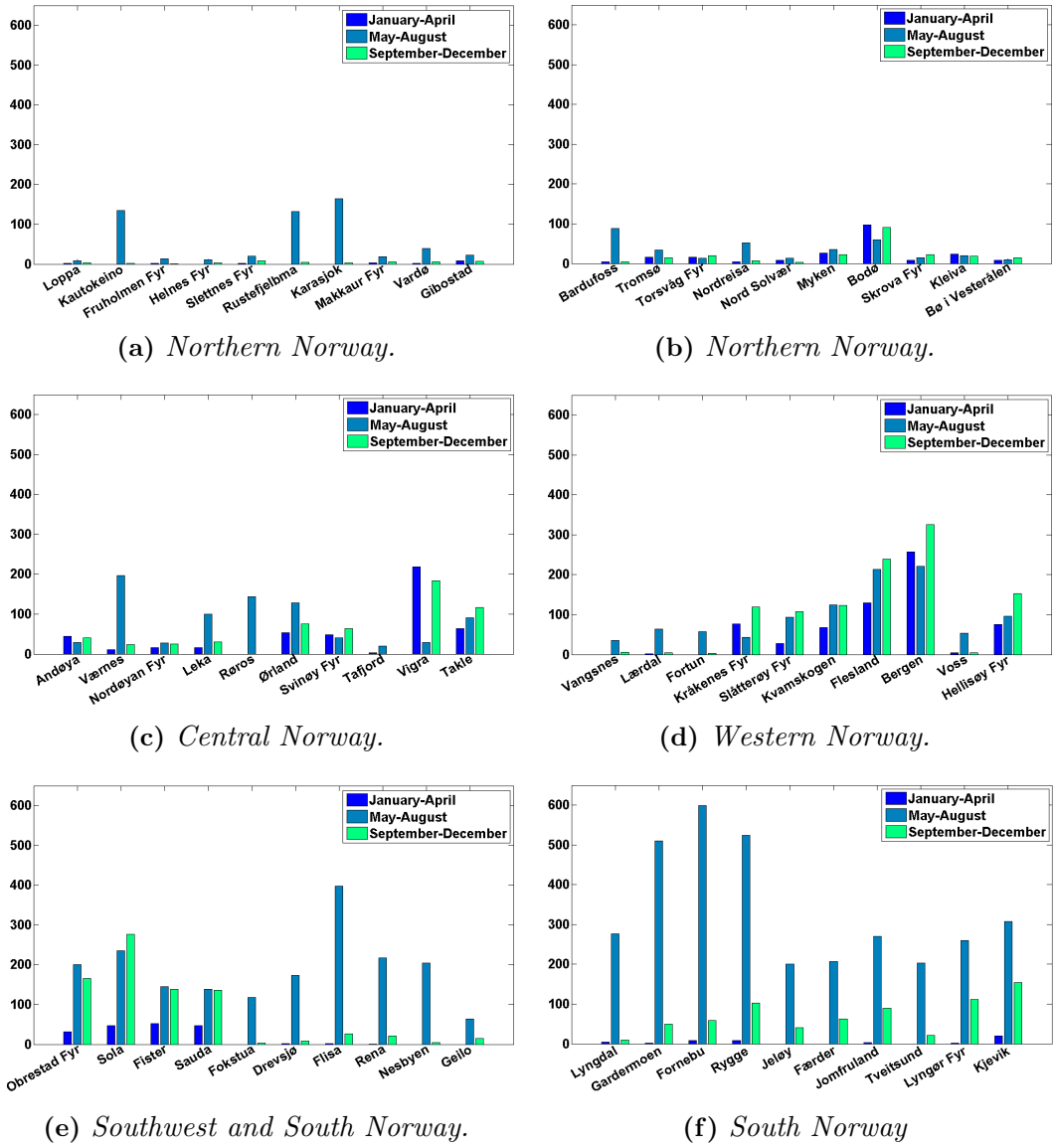

(a) *Northern Norway.* **(b)** *Northern Norway.*

(c) *Central Norway.* **(d)** *Western Norway.*

(e) *Southwest and South Norway.* **(f)** *South Norway*

Figure 5.2: *Observed thunderstorms in Norway from 1960 to 1990 based on data from The Norwegian Meteorological institute from 60 meteorological stations. The dark blue column shows the number of observed thunderstorms from January to April, the blue column shows the number of thunderstorms from May to August and the green column shows the number of observed thunderstorms from September to December.*

observations and multiplied by 1000. Thus, the frequency of thunderstorms is given in promille of observations.

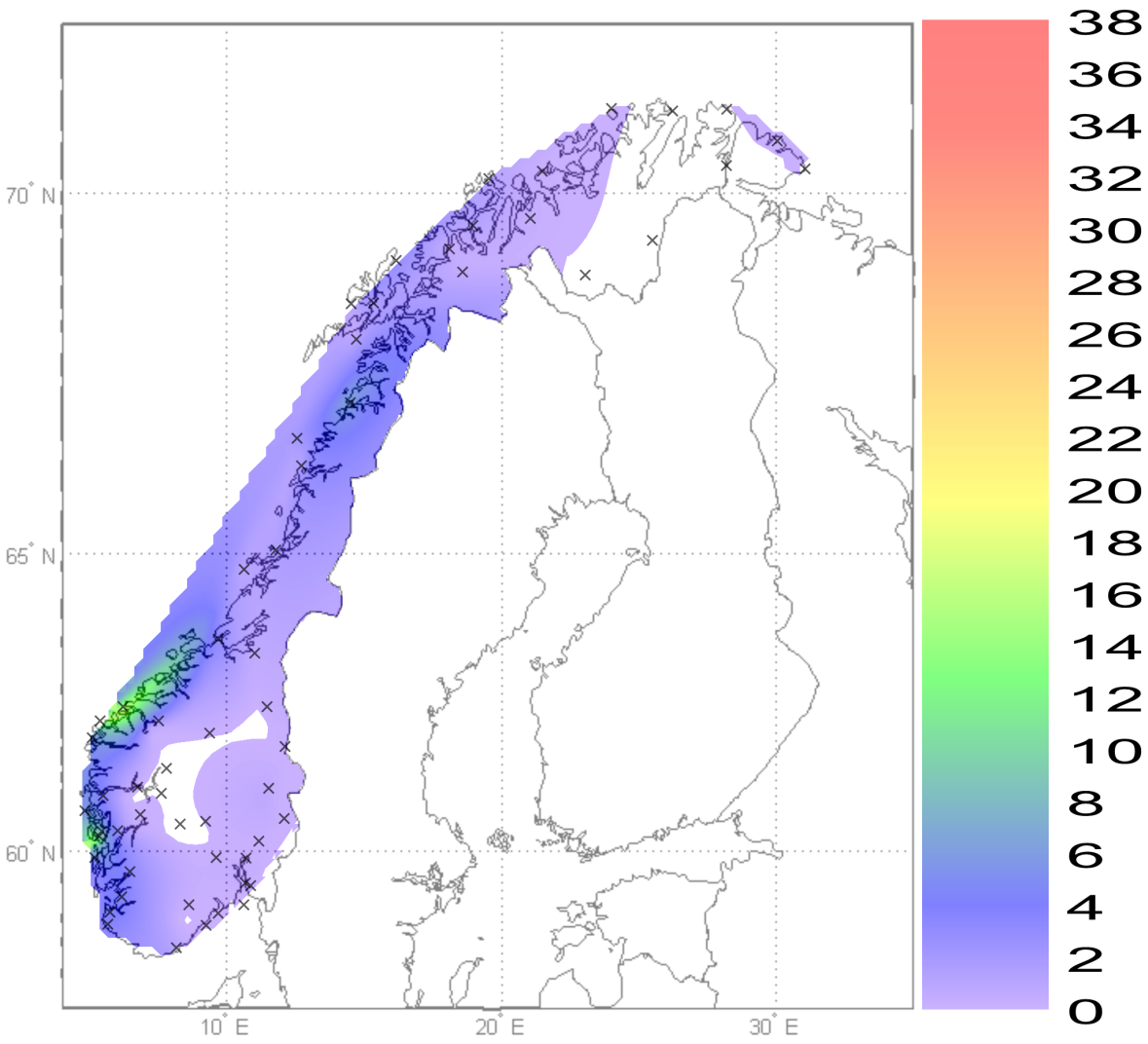

Figure 5.3: *Frequency of observed thunderstorms in promille over Norway from January to April. Based on data between 1960-1990, retrieved from The Norwegian Meteorological Institute.*

5.2 Time series for five different places

In Figure 5.6, the observed thunderstorms from 1957/1958 to 2009 in six different places is shown. The places are Karasjok, Bodø, Vigra, Bergen, Flesland and Fornebu(Oslo), shown in Figure 5.1. In Figure 5.6a, the frequency is shown, and in Figure 5.6b the frequency is shown when the moving window method is used to smooth the curve.

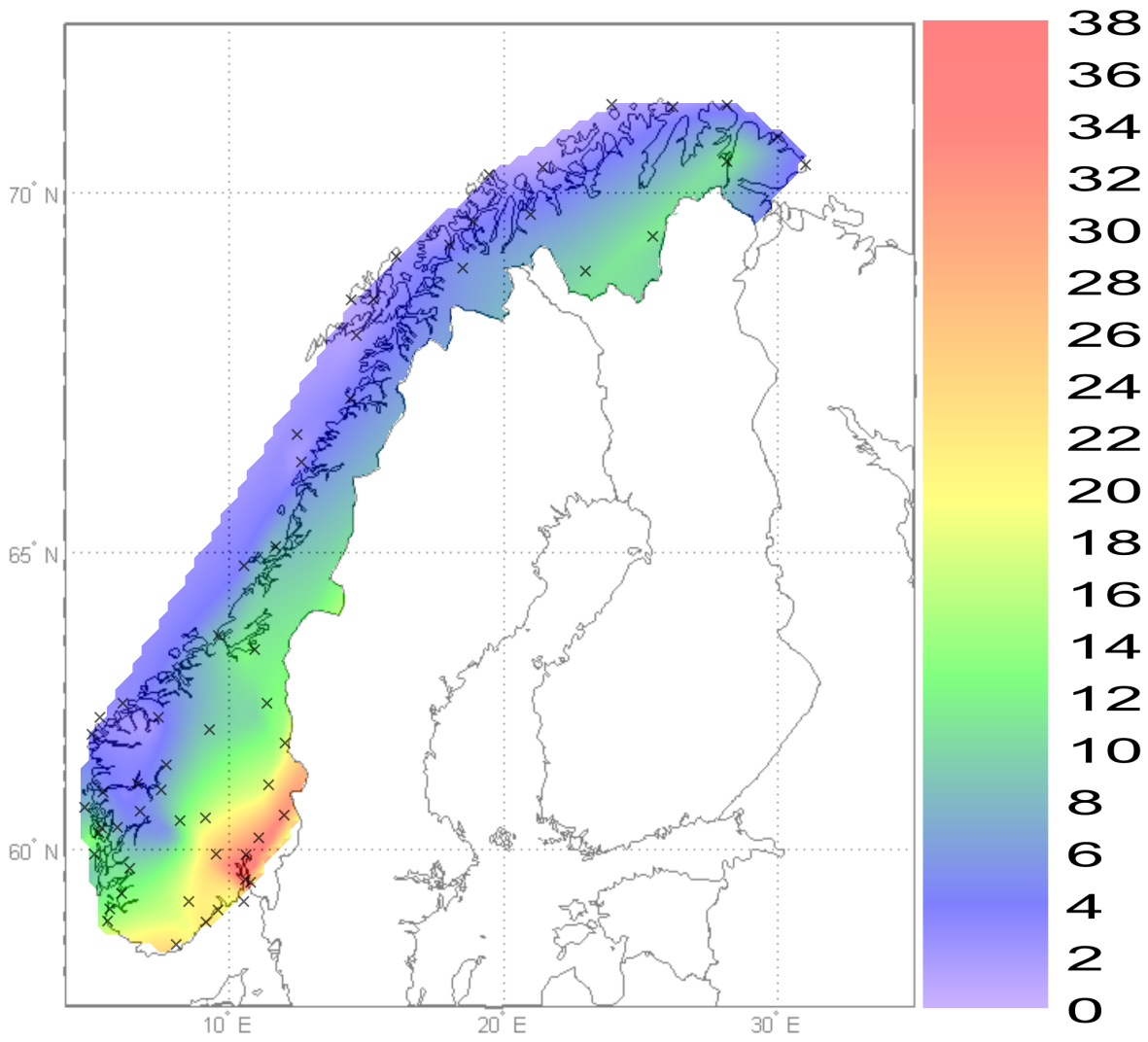

Figure 5.4: *Frequency of observed thunderstorms in promille over Norway from May to August. Based on data between 1960-1990, retrieved from The Norwegian Meteorological Institute.*

The first thing to recognize is that there is a high interannual variability of thunderstorms, and there is not a clear long term tendency of the frequency of thunderstorms in these places. The second thing to notice is that the number of thunderstorms every year differs more for the places in the south than further north, but this is also due to the fact that there is generally a higher number of thunderstorms observed in the south than in the north. Karasjok has the lowest number of thunderstorms, thereafter Bodø and then Vigra. There are observed more thunderstorms in Bergen and Flesland than in Oslo. This is associated with the fact that in Bergen the frequency

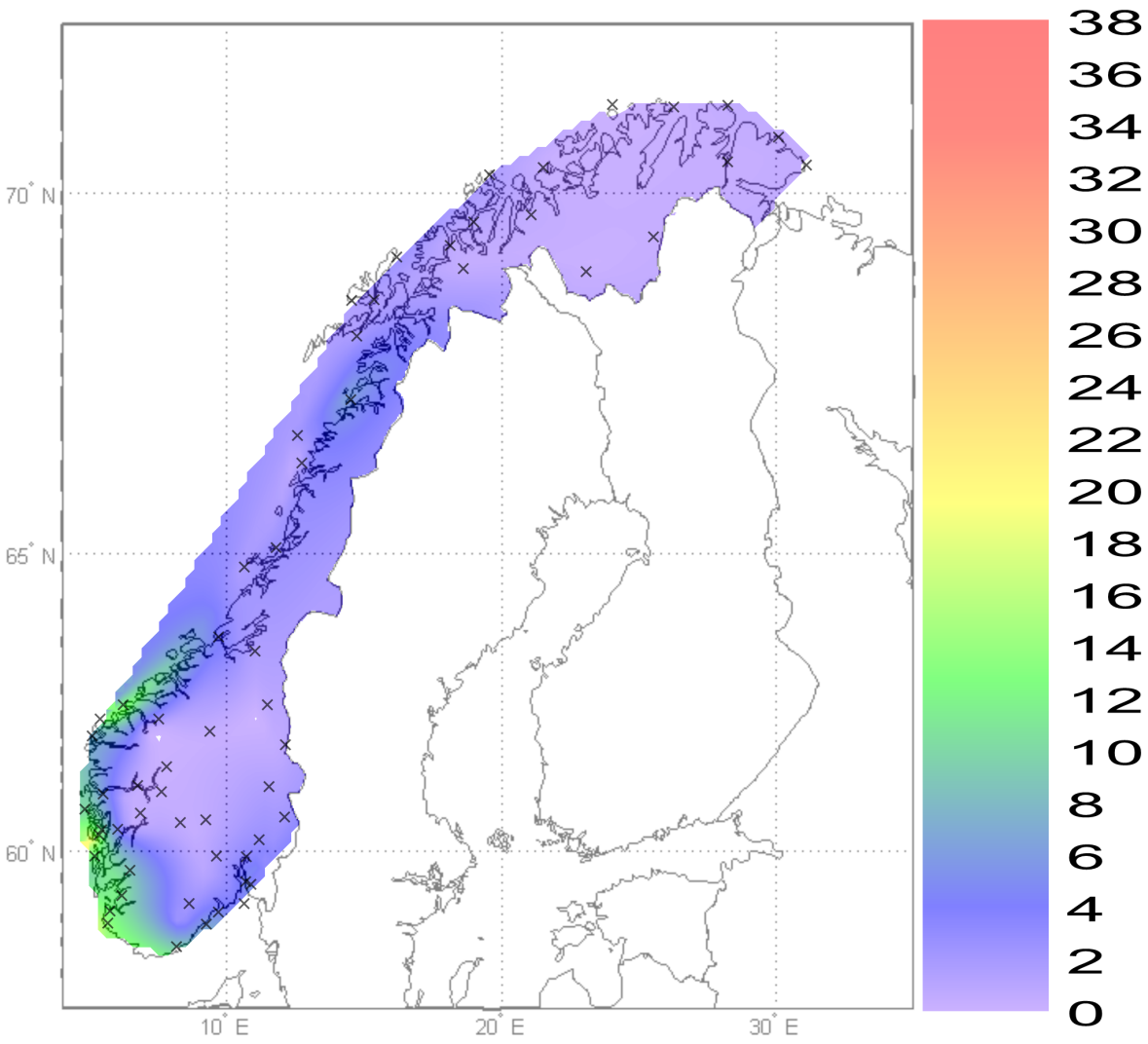

Figure 5.5: *Frequency of observed thunderstorms in promille over Norway from September to December. Based on data between 1960-1990, retrieved from The Norwegian Meteorological Institute.*

of thunderstorms is relatively high throughout the whole year, while in Oslo nearly all the thunderstorms are observed in the summer, as shown in Figure 5.2. Note that there are observed fewer thunderstorms at Flesland than in Bergen.

The frequency in Bergen shows a peak of thunderstorms in 1990, and the same jump is shown for the nearby station at Flesland. Suggesting that this peak is real, and not a manifestation of an inconsistency in observations.

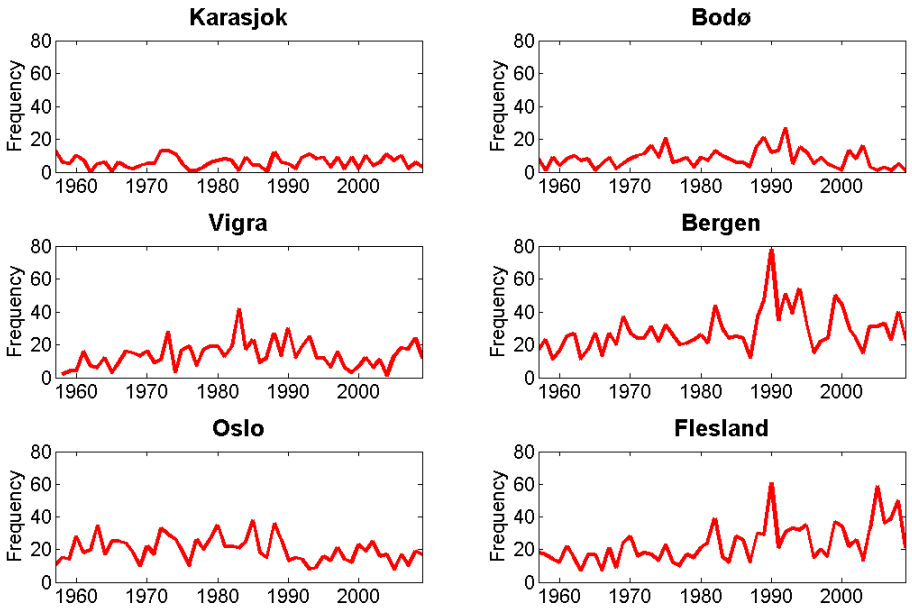

(a) *Without a moving window.*

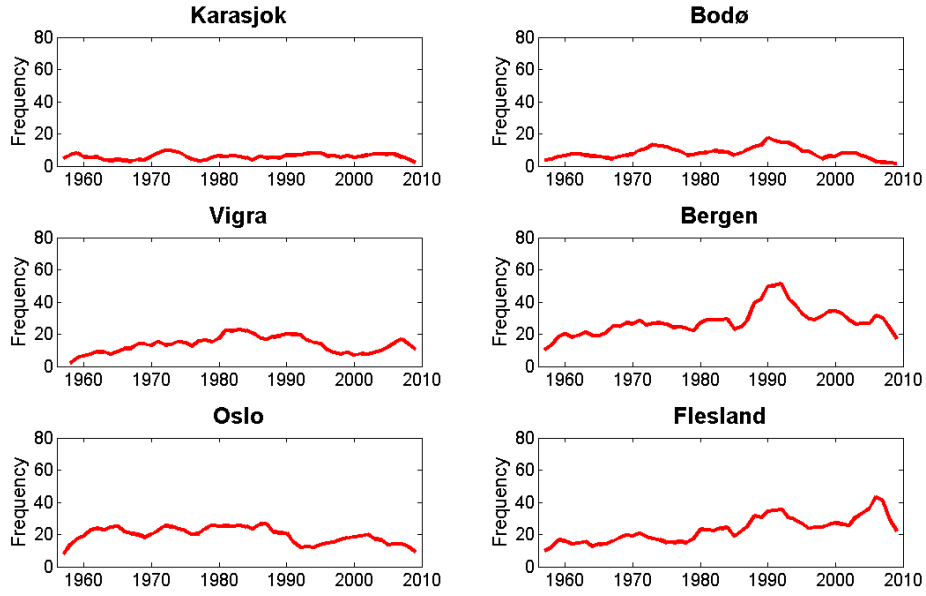

(b) *With a moving window.*

Figure 5.6: *Frequency of thunderstorms for six different places in Norway. (a) shows the variation for each year from 1957 to 2009, (b) shows the variation when there is used a moving window. For Vigra data from 1958 to 2009 is used. Data retrieved from The Norwegian Meteorological Institute.*

5.3 Discussion of the mean annual variability

In this section, the annual variability is shown and discussed. Data from five locations is used, Karasjok, Bodø, Vigra, Bergen and Fornebu. In Figure 5.7, all the data from

1957/1958 to 2009 for every station is used to show the mean annual variability.

For the inland stations, Karasjok has most of the thunderstorm observations between June and August. Oslo has most of the thunderstorm observations from May to September. Karasjok has very few thunderstorm observations from January to May and September to December. In Oslo there are observed few thunderstorms from January to April and October to December. This pattern in Oslo and Karasjok is due to a longer summer season in Oslo than in Karasjok because Oslo is located further south. The fact that only few thunderstorms are observed in the winter months is probably due to too cold temperature at low levels, and too high static stability.

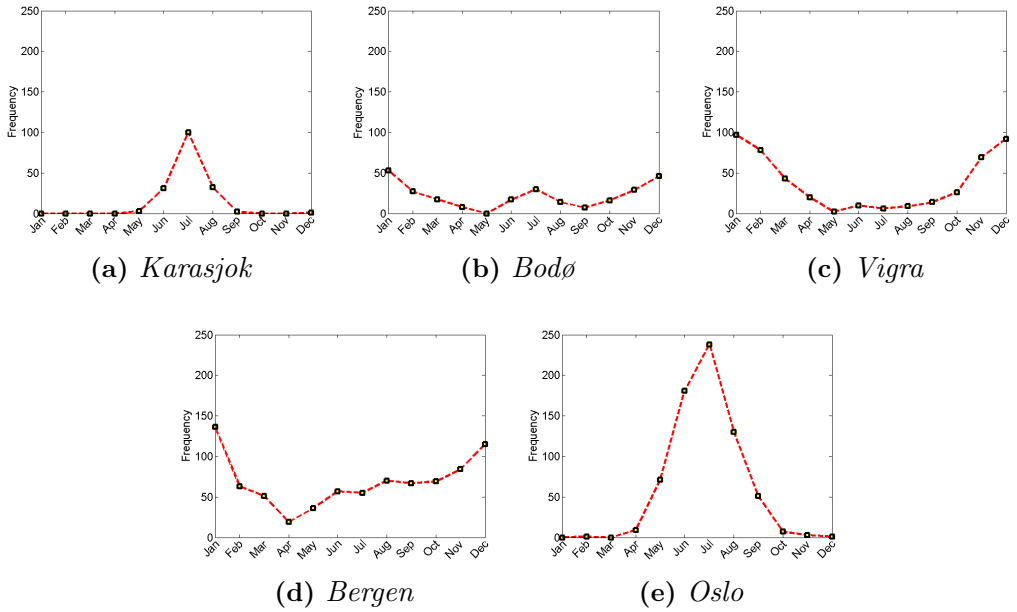

(a) *Karasjok* **(b)** *Bodø* **(c)** *Vigra*

(d) *Bergen* **(e)** *Oslo*

Figure 5.7: *Mean annual variability of thunderstorms for five different places from 1961 to 1990. Based on synoptic data retrieved from the Norwegian Meteorological Institute.*

In Bodø there are observed two maxima, one absolute maximum in January and one local maximum in July. The local maximum in July is probably due to the summer time heating in the afternoons. The absolute maximum in January is to some extent due to cold air outbreaks from the north. Advection of air in extra-tropical cyclones is also a reason for the appearance of thunderstorms, both in January and July. There are also observed two minima, the absolute minimum in May, and a local minimum in September. Below, there is a possible reason of why the frequency of thunderstorms in May will be lower than in September. Since the appearance of thunderstorms is dependent on the atmospheric conditions in the lower level of the atmosphere, and

since the sea surface temperature(SST) has a big impact on the atmospheric condition in the lower levels, the SST can explain why the absolute minimum is observed in May and why the local minimum is observed in September. This is because the SST in May is lower compared to in September. The sea will gain more heat from the atmosphere in May than in September. This will reduce the temperature in the lower levels of the atmosphere more in May, than in September, and contribute to a more stable atmosphere in May.

At Vigra most of the thunderstorms are observed from January to April, with a maximum in January. This is due to the same reasons that were mentioned for Bodø in January. In Vigra, the frequency of thunderstorms is relatively low between May and September. Low appearance of thunderstorms due to surface heating in the afternoon can explain this. From September/October, the frequency of thunderstorms is still relatively low. From November, the frequency becomes higher, and this is probably due to extratropical cyclones and probably some cold air outbreaks. In Bergen the absolute maximum is in January. This is associated with westerly winds in extra-tropical cyclones, but also in some extent due to cold air outbreaks. The only minimum point in the observations from Bergen is in April. This is probably due to the same reason that was suggested for Bodø, but here there is not a minimum in September as well, this could be due to a lower latitude with a longer summer season or a higher frequency of extra-tropical cyclones.

5.4 Discussion of the mean diurnal variability

In 5.8 the mean diurnal variability of thunderstorms is observed for Karasjok, Bodø, Vigra, Bergen and Oslo. The observations from 00 UTC, 06 UTC, 12 UTC and 18 UTC are used, but at Vigra only the observations from 06 UTC, 12 UTC and 18 UTC are used.

The diurnal cycle of thunderstorms in Karasjok and Oslo, with the highest frequency in the afternoon or in the late evening, indicates that the observed thunderstorms in Oslo and Karasjok are due to summer time afternoon convection. Off course, not all thunderstorms in this areas, specially in the Oslo area, appear because of warm summer day convection. Also advection of warm and humid airmasses at low tropospheric levels and/or advection of cold air at middle to upper tropospheric levels can contribute to thunderstorms. Therefore there are also thunderstorm observations in

the morning hours.

In Bergen, Bodø and Vigra there is a high frequency of thunderstorms throughout the whole day. This is because the main factor that gives thunderstorms in these areas is not summer time convection in the afternoon, but advection of airmasses. Either as cold air outbreaks or extratropical cyclones.

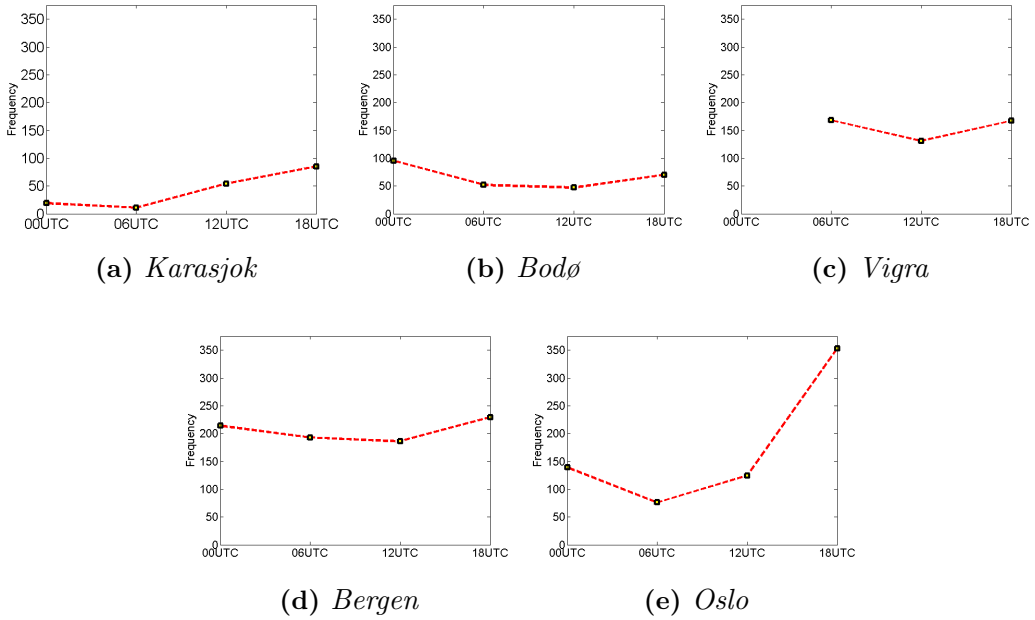

(a) *Karasjok* **(b)** *Bodø* **(c)** *Vigra*

(d) *Bergen* **(e)** *Oslo*

Figure 5.8: *Mean diurnal variability of thunderstorms for five different places from 1961 to 1990. Based on synoptic data retrieved from the Norwegian Meteorological Institute.*

5.5 Discussion of the stability

A remarkable and unexpected feature of the seasonal variability is the difference between the northern and southern part of Vestlandet. In this section, a stability plot of the atmosphere is shown to explore the difference between the thunderstorm observations for the northern part on Vestlandet with the southern part on Vestlandet. From Figure 5.2 it was shown that Vigra has more observed thunderstorms than Sola from January to April, and Sola has more observed thunderstorms than Vigra from September to December. Figure 5.9 shows a mean number of days each year from 1996-2008 which has a temperature difference of 38°C or more between 500 hPa and the ground level at Sola, Ørlandet and Bodø.

Overall, Ørlandet has the highest number of unstable days, followed by Bodø and then Sola. Ørlandet has a higher number of days with unstable air in the period from January to April, than for the period from May to August and September to December. In Bodø and Sola the tendency is different. The highest number of days with unstable air is from May to August, followed closely by the other seasons.

At Ørlandet, there are 4 more days with unstable air in the mean every year from January to May than September to December. At Sola, the difference is 0 days. This corresponds with the previous finding that there are more thunderstorms at Vigra than at Sola from January to April and less from September to December.

To connect this stability study to observed thunderstorms it has to be considered that the sounding on Ørlandet is approximately 120 km from Vigra, and this distance may reduce the representativeness of the Ørlandet sounding for Vigra.

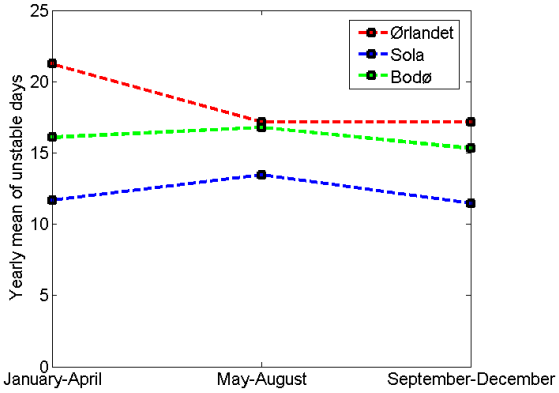

Figure 5.9: *Stability plot of the atmosphere that shows a mean number of days each year where the temperature difference between the 500 hPa level and the ground level is 38° C or bigger for three different stations, Ørlandet, Sola and Bodø. Based on data from soundings from 1996-2008 at 00 UTC and at 12 UTC, obtained from Birgitte Furevik at The Norwegian Meteorological Institute.*

5.6 Discussion of general variability

For the stations in Northern Norway, the highest frequency is observed inland between May and August. The study on the annual and diurnal variability of Karasjok shows that this is due to summer time afternoon convection. The few thunderstorms that

are observed from January to April and September to December are probably due to advection of airmasses in extratropical cyclones or from cold air outbreaks.

The thunderstorm observations at the inland stations on Vestlandet and in Central Norway between May and August are probably due to summertime afternoon convective heating. These stations have few thunderstorm observations from January to April and September to December due to too cold low level temperatures, which contribute to a more stable atmosphere. In the coastal areas the frequency of thunderstorms is mainly due to advection of air in extratropical cyclones and cold air outbreaks. Stations located in areas in front of the mountains without orographic disturbances, such as lighthouses or Flesland, have generally fewer thunderstorm observations than stations located in an area with much orographic disturbances, such as Bergen. The effect of the topography can explain this. As an example, the mountains surrounding Bergen influence the air flow and contribute to a higher frequency of thunderstorms. At Flesland, which is located approximately 8-10 km south of Bergen has not the same effect due to less orographic influence.

This topography effect can also have an influence on the thunderstorm appearance inland, but the thunderstorm observations inland is mainly observed between May and August. Therefore there is appropriate to consider local surface heating as the main reason. On the other hand, in Sauda, in Southwest Norway it seems to be that both the summer time afternoon convection and the topography influence the thunderstorm frequency because there are observed thunderstorms throughout the whole year. The fact that Sauda is located further south can also influence the frequency of thunderstorms.

In general, the high frequency of thunderstorms at Vestlandet throughout the whole year can be explained with 4 factors. First, the extratropical cyclones produce thunderstorms throughout the whole year. Second, some thunderstorms in the winter and autumn are due to cold air outbreaks. Third, summer time afternoon convection is present from May to September because of a longer summer season at this latitude compared to further north. Finally, locations at the coast in areas with much orographic effect will have an influence on the frequency.

In Southeastern Norway, summertime afternoon convection is the main reason for thunderstorms between May and September. The study on the annual and diurnal variability supports the idea that Oslo has mainly convective summer afternoon events

since nearly all the thunderstorm observations are in the evening. The map, Figure 5.5, shows that there are also some thunderstorms from September to December. The study on the annual variability for Oslo shows that the thunderstorms observed from September to December, are mainly observed in September. This appears as an extension of the summer season. As mentioned earlier, advection of airmasses can also contribute to thunderstorms in this area. In the winter, the temperature at low levels is generally too cold, and the requirements for thunderstorms is not fulfilled.

5.7 Conclusions

A study of the frequency of thunderstorms for five different places in Norway shows that the interannual variability is large and there is not a clear long term trend.

This study has also shown that in the Southeastern part of Norway, most of the thunderstorms is observed from May to September, and there were hardly any observations of thunderstorms from January to April and September to December. At Vestlandet, thunderstorms are observed through the hole year, but at stations further inland away from the coast, the thunderstorms are generally observed between May and August. In general, one may say that Southeast Norway has a nearly continental character, and Vestlandet has a maritime character.

It is also shown that there are observed fewer thunderstorms at northern latitudes compared to further south. This is presumably due to changes in the meteorological conditions, which among other factors are the dependent on the latitude. The thunderstorm observations seem also to be dependent on the topography. In Northern Norway, there are generally few thunderstorm observations, and the highest frequency is mainly observed at the inland stations between May and August due to summer time afternoon convection.

Chapter 6

The 3 July 2009 Oslo Thunderstorm

6.1 Observations

From the climate study of thunderstorms in Norway, described in Chapter 5, the Oslo area has a thunderstorm frequency of 36‰in the summer season. Some of those storms are quite intensive. On 3 July 2009, an intensive thunderstorm hit Oslo, after several days with warm and fair weather. A big part of Southeast Norway and South Sweden were affected by the convective weather. Heavy rain, strong winds, lightnings and thunder were observed around 18 UTC on 3 July in Oslo. On Blindern, one of the weather stations in Oslo, there was observed 15.5 mm of rain in less than 1 hour. The temperature dropped from 28.6°C to 19°C in association with the onset of the rain that afternoon, and the strongest observed gust wind was 21.6 m/s. Numbers from SINTEF[8], tell us that there were observed around 2000 lightning strikes during one hour when the weather was on its worst. There were many consequences of this weather. Over 40000 houses lost their electricity, streets were overflowed with water and trees fell over because of lightning or the strong wind gusts. The southern part of Sweden was also affected by this weather, and here one man died. In the rest of this chapter the focus will be on this weather event.

In Figure 6.1, the temperature and precipitation at Blindern in Oslo the last 14 days before this event are shown. It had been very warm with daytime temperatures over 25°C degrees for 8 days, and low humidity with 12 days without any precipitation. After the convective events on 3 and 4 July(Figure 6.1), there is a sudden change in the weather, with daytime temperatures below 20°C and some precipitation.

The satellite images(Figure 6.2), show the convective clouds are forming throughout

[8] http://www.sintef.no/

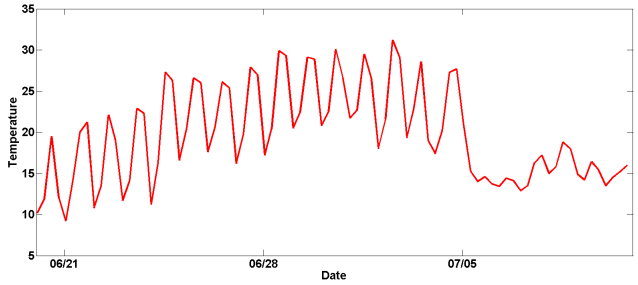

(a) *Temperature °C*

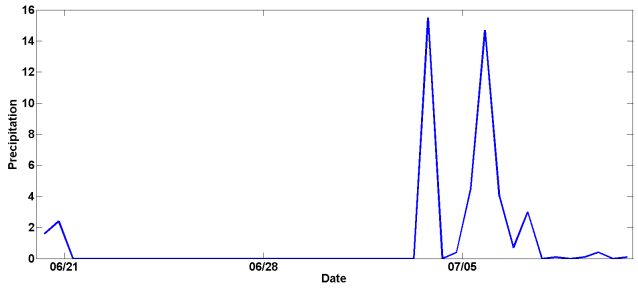

(b) *Precipitation mm*

Figure 6.1: *Variability in temperature [°C] in (a), and precipitation [mm] i (b) from 20 June to 10 July 2009 at the meteorological station Blindern in Oslo. Data retrieved from The Norwegian Meteorological Institute.*

the day at four different times. From those pictures it is easy to see that it was a fair weather situation at 09.16 UTC on 3 July over large areas in Southeast Norway. Later on, some convective clouds had been forming north and east of Oslo at 12.04 UTC, as shown in Figure 6.2b. Between 12.04 UTC and 19.06 UTC there had been further development of convective clouds, and in Figure 6.2c, the big convective cloud south of Oslo is the thunderstorm that hit Oslo 1 hour earlier. At 01.57 UTC 4 July(Figure 6.2d), the convective event is over and most of the clouds have disappeared, but there are still some convective clouds in Northern Skagerrak and northeast of Oslo. It is clear that the precipitation this day came from convective cells.

Data from 338 precipitation gauges, retrieved from The Norwegian Meteorological Institute(MET) and The Swedish Meteorological and Hydrological Institute(SMHI) at 18 UTC on 3 July and at 06 UTC on 4 July are used in this study. This data is interpolated and plotted(Figure 6.3a). The black dots indicate the locations of the precipitations gauges. A cubic interpolation is used to interpolate the precipitation. To give a better overview for the Oslo area, Figure 6.3b shows a zoomed in area over Southeast Norway.

Hovmöller diagrams are usually used to trace anomalies, in this context, the diagrams

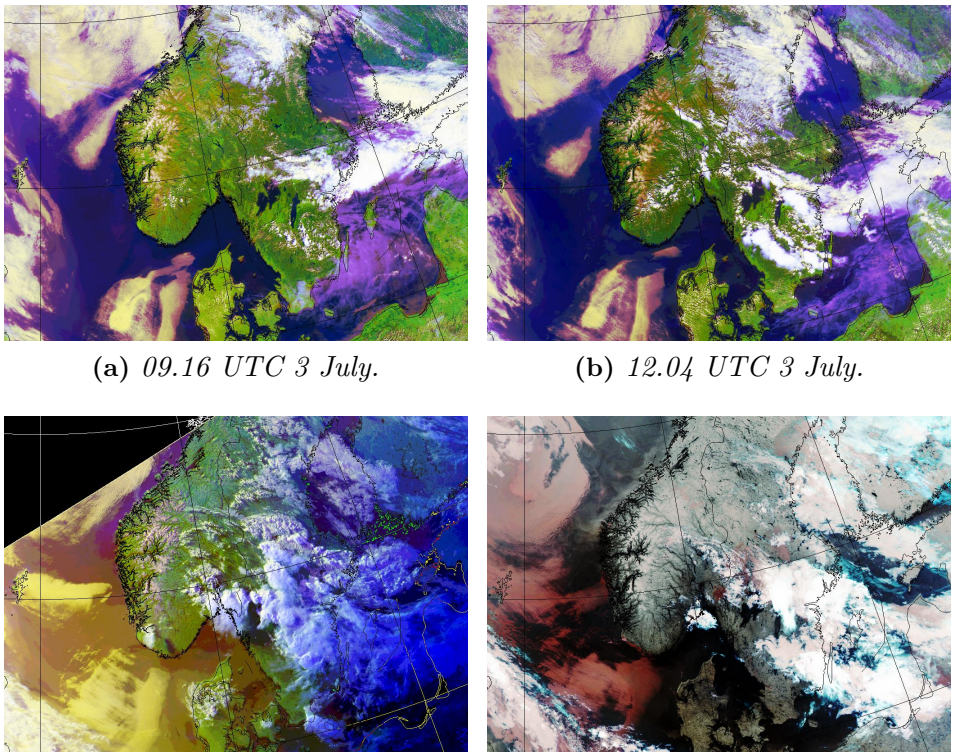

(a) *09.16 UTC 3 July.* **(b)** *12.04 UTC 3 July.*

(c) *19.06 UTC 3 July.* **(d)** *01.57 UTC 4 July.*

Figure 6.2: *Satellite pictures from 3 and 4 July over Southern Scandinavia at different times. At 09.16 UTC on 3 July in (a), at 12.04 UTC on 3 July in (b), at 19.06 UTC on 3 July in (c) and at 01.57 UTC on 4 July in (d). The pictures retrieved from The Norwegian Meteorological Institute, by Vegard Kristiansen.*

are used to show the change in the weather situation. The evolution in geopotential and temperature over time at 1000 hPa for longitudes from 0° to 45°E (Figure 6.4), shows a change in the weather situation after the convective events on 3 and 4 July. Figure 6.4a and 6.4b shows that the geopotential height lowers from 160 m to 40 m, and the temperature lowers approximately 4°C in the area around 10°E between 3 and 5 July.

Figure 6.5 shows that there is a tongue of warm air at 1000 hPa and 500 hPa. This means that there is not a typical thunderstorm situation with cold air at 500 hPa and warm air at the ground, but there is warm air from 1000 hPa and up to at least 500 hPa. The temperature difference between 1000 hPa and 500 hPa is however high enough to produce thunderstorms. As discussed earlier, the temperature difference between 1000 hPa and 500 hPa must be around 38°C or more to produce thunderstorms. The observed ground temperature was 28.6°C and NOAA[9] reanalysis(Figure

[9] `http://www.noaa.gov/`

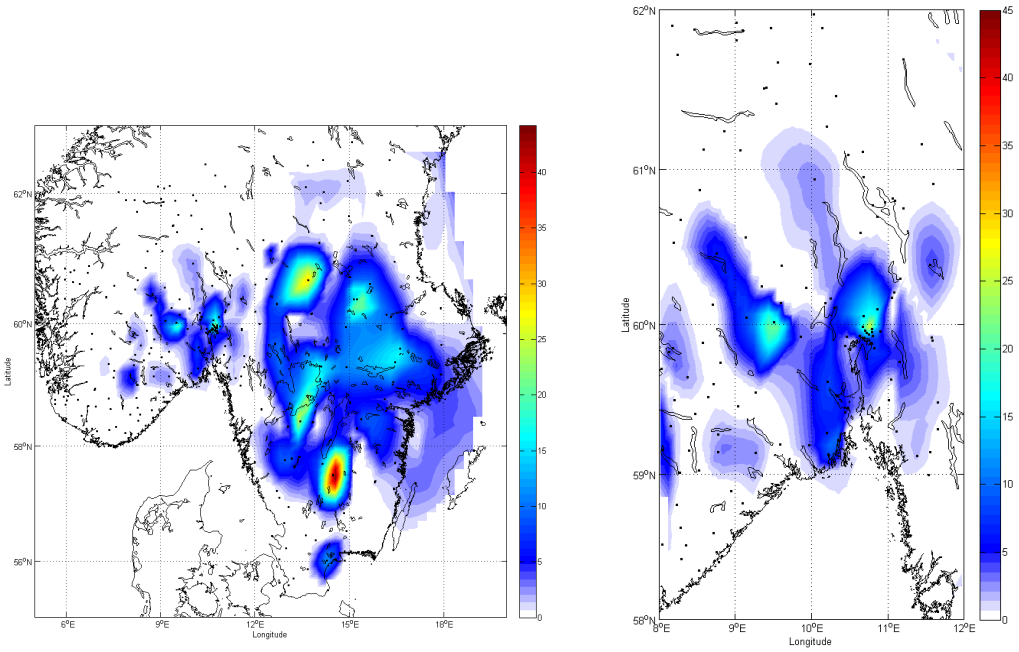

(a) *Southern Scandinavia.* **(b)** *Southeast Norway.*

Figure 6.3: *Interpolated observed precipitation[mm] between 06 UTC on 3 July to 06 UTC 4 on July from 338 different precipitation gauges over Southern Scandinavia. The black dots are the locations for the precipitation gauges. Data retrieved from The Norwegian Meteorological Institute and the Swedish Meteorological and Hydrological Institute.*

6.5b), gives a temperature of -15°C at 500 hPa. This gives the temperature difference of 43.4°C. Figure 6.5a shows the NOAA reanalysis of the temperature at 1000 hPa.

The variation of relative humidity(RH) over time(Figure 6.6), shows the change in RH at 1000 hPa and 700 hPa at longitudes between 0 and 45°E between 15 June to 15 July 2009. A interesting part is that at approximately 10°E in Figure 6.6a, the RH varies from 65% to 90% from 2 July to 5 July. At 700 hPa(Figure 6.6b), the RH has a tendency that goes from 24% to 48%. This means that a high RH in the lower troposphere, and a lower amount of RH in middle to upper troposphere might have been important for the development of the severe thunderstorm. The sounding(Figure 6.7), from WRF confirms that the RH was high in the lower troposphere.

6.2 The synoptic situation

This section gives a brief description of the synoptic situation on 3 July 2009 over Europe and The North Atlantic. The circulation at 500 hPa is discussed together with

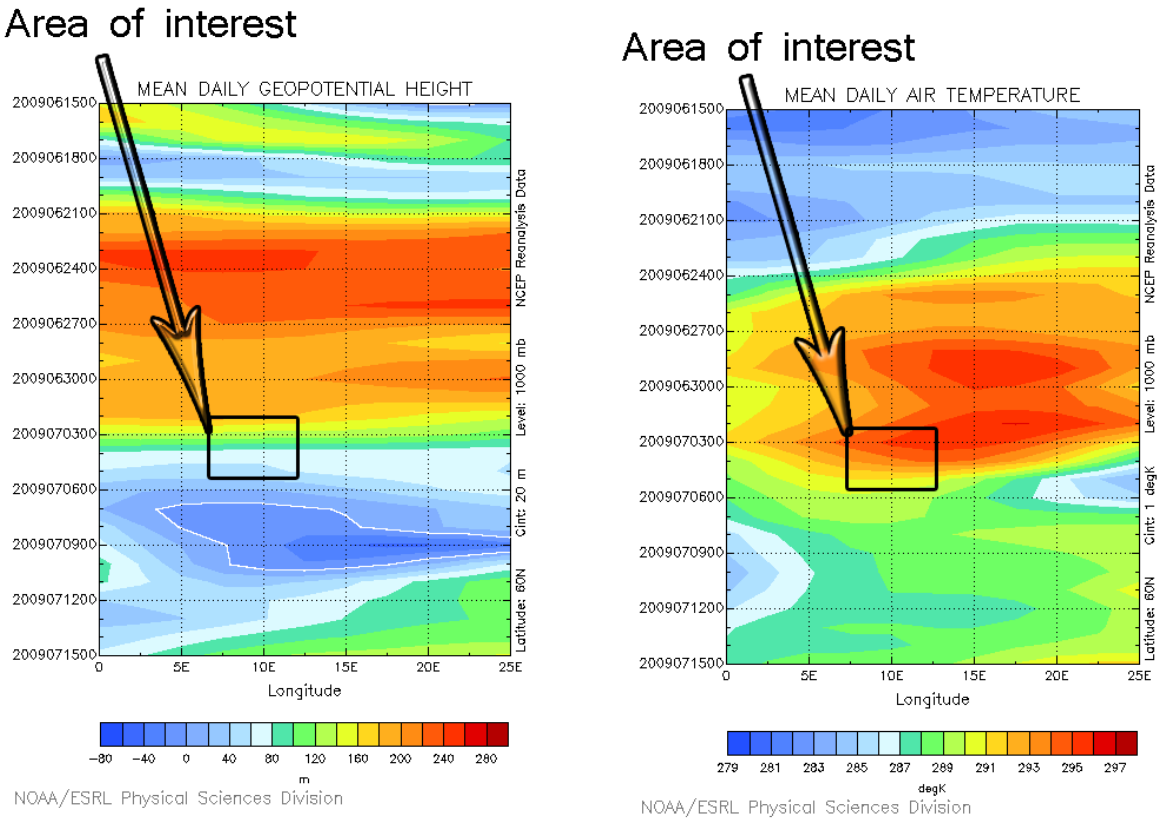

(a) *Geopotential height at 1000 hPa.*

(b) *Air temperature at 1000 hPa.*

Figure 6.4: *Hovmöller diagrams for longitudes from 0° to 45°E at 1000 hPa from 15 June to 15 July 2009. The mean geopotential height[m] in (a), and the mean air temperature°C in (b). Data retrieved from NCEP/NCAR, acquired from NOAA.*

the temperature anomaly from the climatological mean(1968 - 1996). A surface analysis of the situation is given, and at the end a description of what the meteorologists have based the forecast on.

6.2.1 The 500 hPa circulation and the temperature anomaly

Figure 6.8 shows the geopotential height(Figure 6.8a) and the geopotential height anomaly from the climatological mean (1968-1996)(Figure 6.8b) at 500 hPa over Europe and The North Atlantic. There is a stable high pressure situation over Northwestern Europe. West of the British Isles there is a low pressure system with strong geopotential gradients. Over Russia there is also a low pressure situation with strong geopotential gradients. This situation looks very similar to an omega blocking, where the high pressure cuts off the westerly flow with lows to each side. Omega blocking events are discussed in Chapter 2. In this case, the high pressure situation over South-

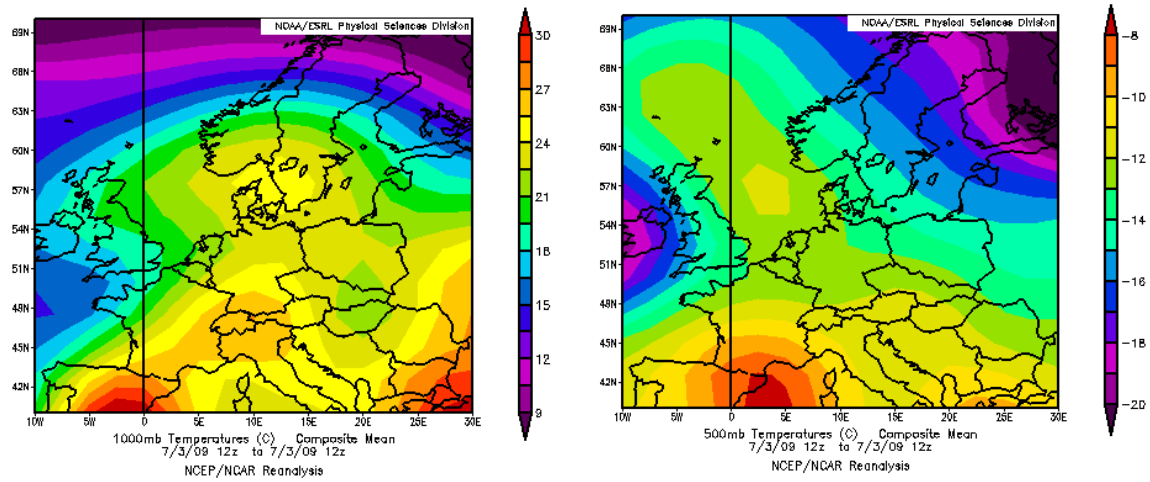

(a) *Air temperature at 1000 hPa.* **(b)** *Air temperature at 500 hPa.*

Figure 6.5: *Air temperature[°C] for 6 hourly reanalysis data composites from 12 UTC to 18 UCT on 3 July 2009. At 1000 hPa in (a) and at 500 hPa in (b). Data retrieved from NCEP/NCAR, acquired from NOAA.*

east Norway is most interesting and the geopotential height gradient in this area is relatively weak with a difference between 5750 m to 5775 m over approximately 500 km. The geopotential height anomaly shows that the geopotential height on 3 July is higher than the climatological mean(1968-1996) in Southern Scandinavia. In Southeast Norway there is a average aberration between 125 - 150 m.

At 500 hPa, the temperature anomaly was between 3-5°C higher than the climatological mean(1968-1996) in Southeast Norway(Figure 6.9a). As also shown, the temperature anomaly was as high as 6°C in the Norwegian Sea. At lower altitudes, at 850 hPa, the temperature anomaly is higher than in 500 hPa(Figure 6.9b). Here the temperature anomaly goes from 6-8°C. It is also clear that the temperature anomaly is negative in the low pressure systems.

6.2.2 Surface analysis

The synoptic situation on the ground and the observations over Europe and North Atlantic at 12 UTC on 3 July are shown in Figure 6.10. There is a high pressure situation over Southern Scandinavia and Northern Germany that influences the surface circulation on the whole continent with calm winds throughout central parts of Europe. Over the British Isles there are several fronts. As observed at the 500 hPa and 850 hPa levels, a low pressure system is over the Atlantic Ocean and Russia.

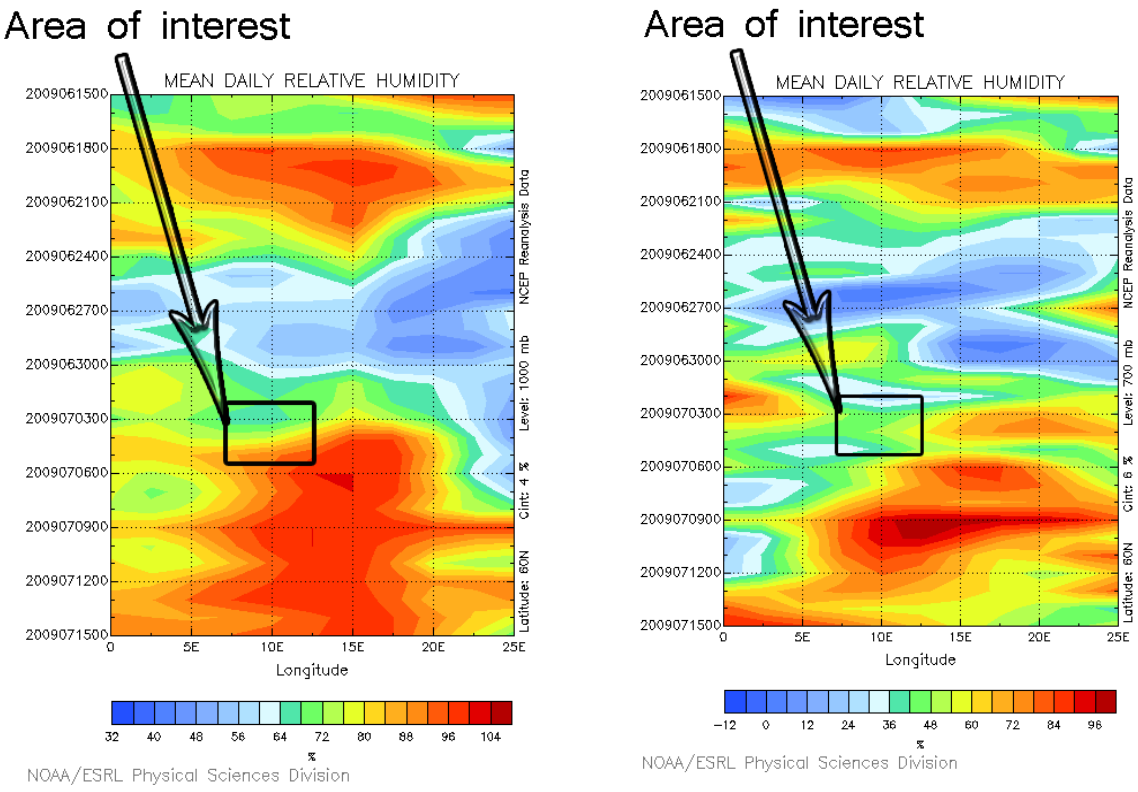

(a) *Relative humidity at 1000 hPa.*

(b) *Relative humidity at 700 hPa.*

Figure 6.6: *Hovmöller diagram of relative humidity[%] from 15 June to 15 July 2009 at longitudes from 0° to 20°E. The Relative humidity at 1000 hPa in (a), and the relative humidity at 700 hPa in (b). Data retrieved from NCEP/NCAR, acquired through NOAA.*

The observations show that there are thunderstorms all over Europe this day. From Ukraine in the east, to Holland in west. Thunderstorms are also observed further south in Croatia and northward to Southeast Norway and Central Sweden. A greater part of the observations over the continent has temperatures over 25°C.

6.2.3 Precipitation

For forecasters it is not easy to give a good forecast of summer showers. Together with other models the meteorologists at The Norwegian Meteorological Institute use The High Resolution Limited Area Model(HIRLAM)[10], which is a hydrostatic model, of which the dynamical core is based on a semi-implicit semi-Lagrangian discretisation of the multi-level primitive equations, using a hybrid coordinate in the vertical.

[10] `http://hirlam.org/`

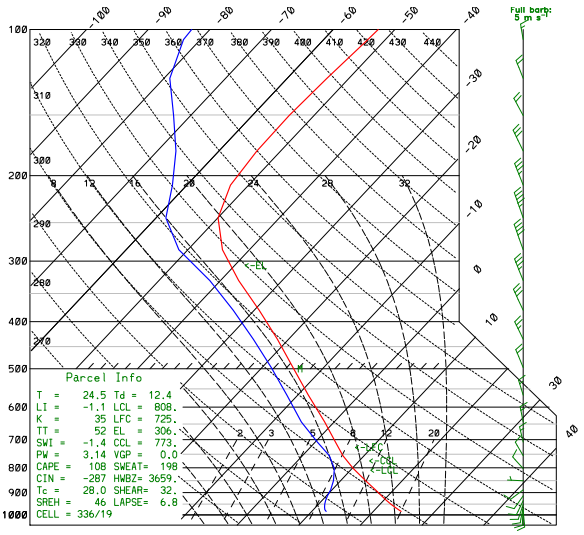

Figure 6.7: *Sounding produced with WRF. At Fornebu(59.9°N,10.6°E) at 18 UTC on 3 July 2009. The red line is temperature and the blue line is the dew point temperature. Information about the parcel is shown in a box down in the left corner, and a horizontal wind barb is located to the right.*

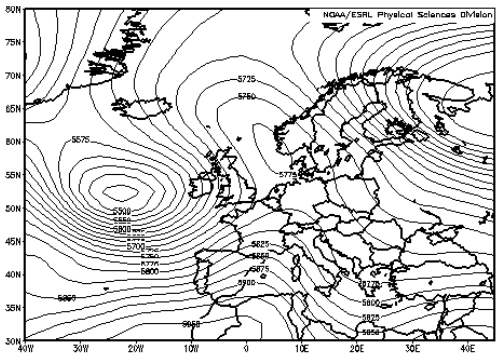

(a) *Geopotential height at 500 hPa*

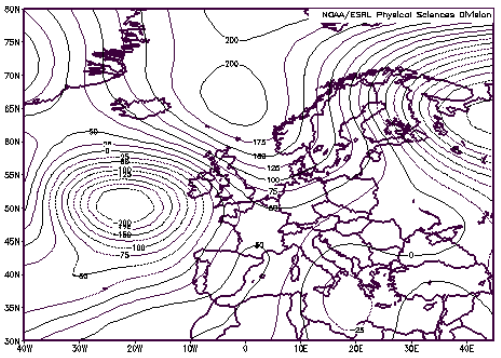

(b) *Geopotential height anomaly at 500 hPa*

Figure 6.8: *The geopotential height[m] at 500 hPa in (a), and The geopotential height anomaly[m] from the climatological mean(1968-1996) at 500 hPa in (b). Both valid for 3 July 2009, and with intervals of 25 m. Data retrieved from NCEP/NCAR, acquired through NOAA.*

HIRLAM is a research cooperation of several European meteorological institutes.

Figure 6.11 shows the forecasted precipitation based on the operational HIRLAM simulations, initialized at different times. They all show some variable convective activity from 1-4 mm in the Southeast Norway area, but no extremes. Only one simulation shows precipitation in the Oslo area, and that is the simulation initialized at

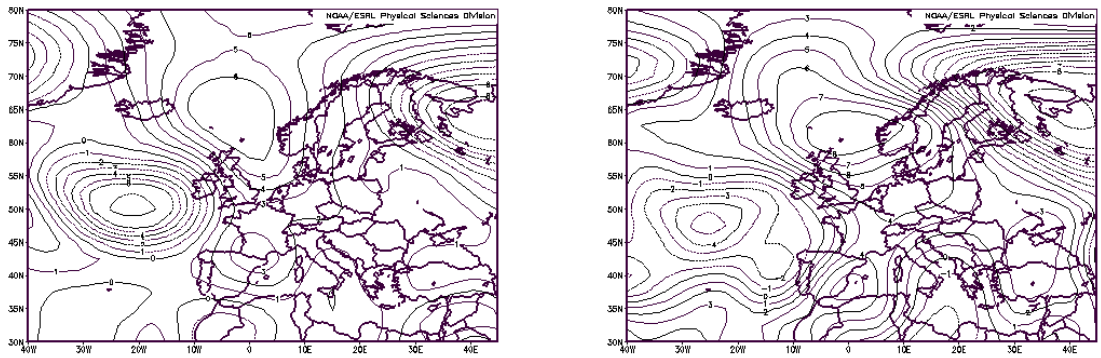

(a) *500 hPa* **(b)** *850 hPa*

Figure 6.9: *The temperature anomaly[°C] from the climatological mean(1968-1996). At 500 hPa in (a), and at 850 hPa in (b). Both valid for 3 July 2009, with intervals of 1 °C. Data retrieved from NCEP/NCAR, acquired through NOAA.*

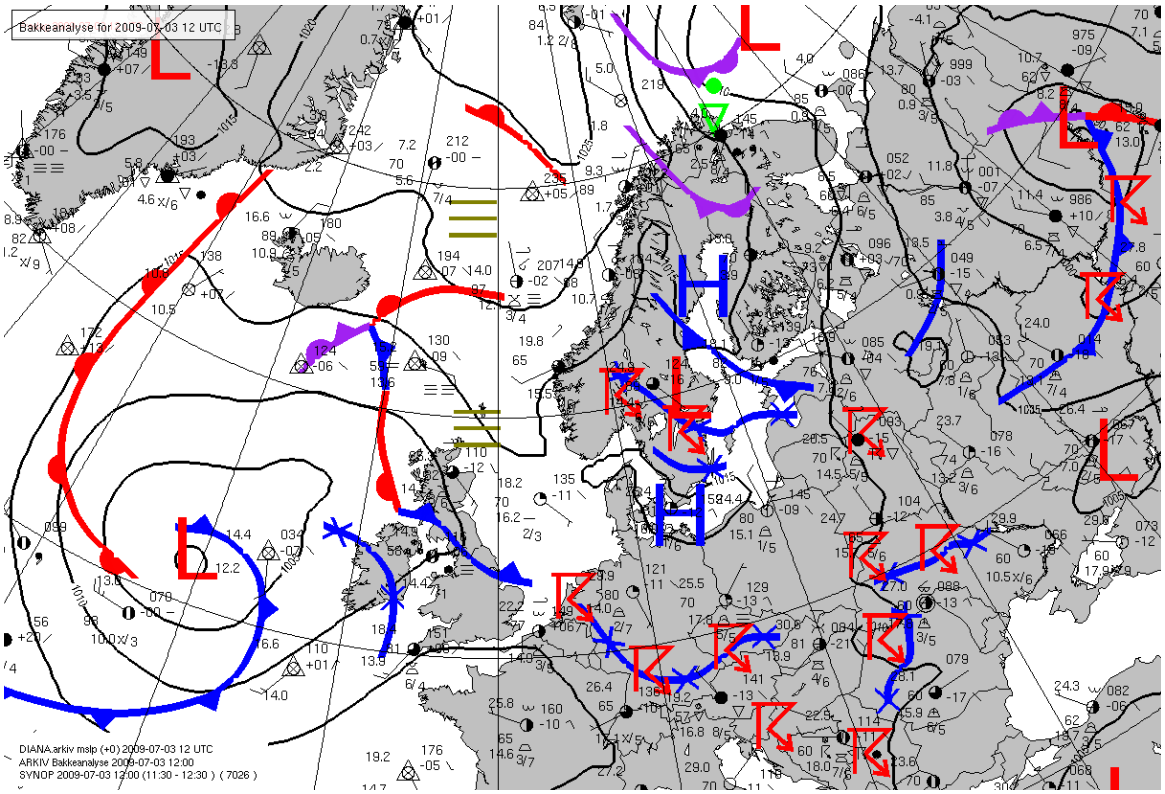

Figure 6.10: *Synoptic weather chart with observations at 12 UTC 3 July 2009. Retrieved from The Norwegian Meteorological Institute, by Trygve Aas.*

00 UTC 3 July(Figure 6.11e).

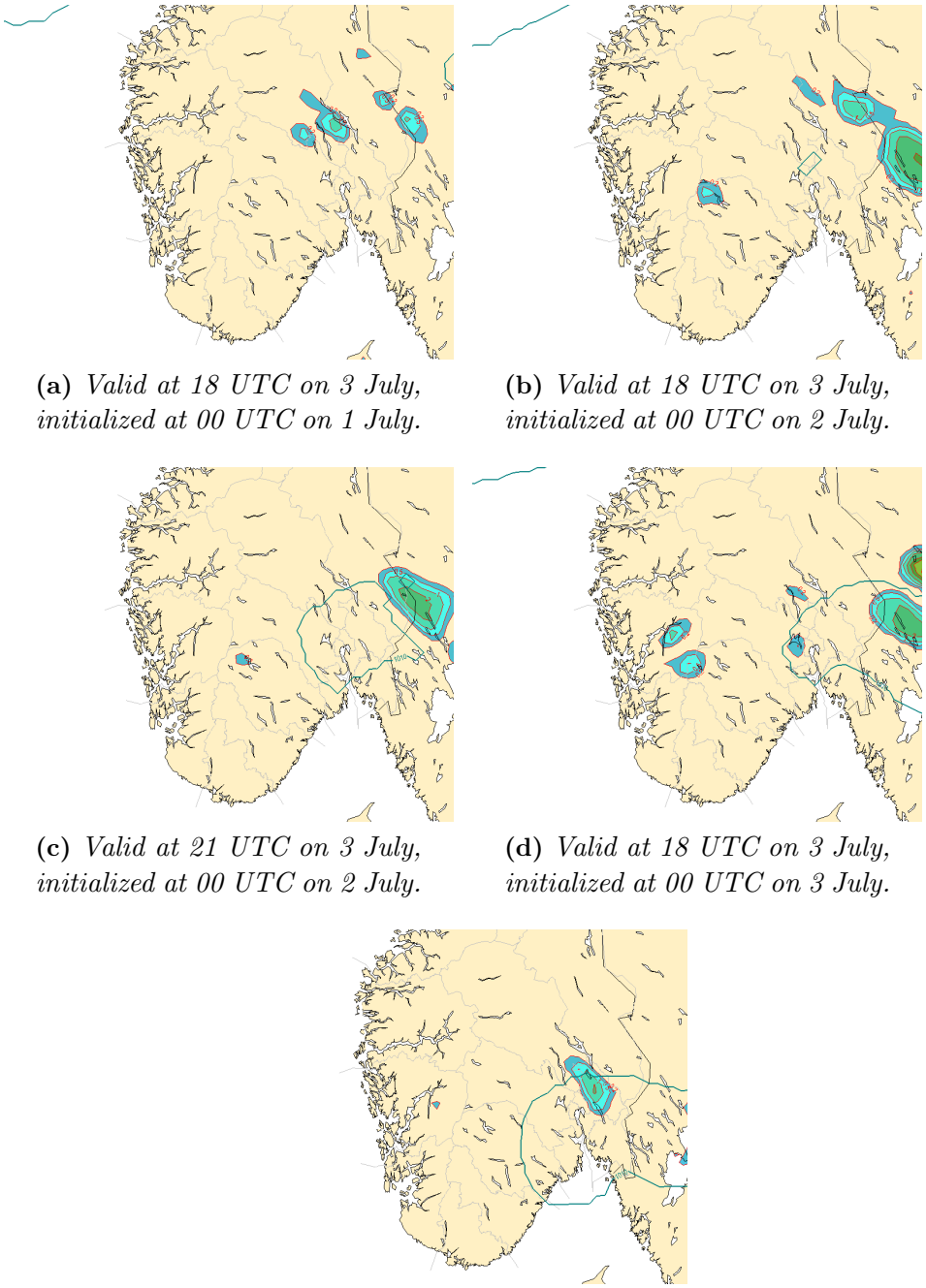

(a) *Valid at 18 UTC on 3 July, initialized at 00 UTC on 1 July.*

(b) *Valid at 18 UTC on 3 July, initialized at 00 UTC on 2 July.*

(c) *Valid at 21 UTC on 3 July, initialized at 00 UTC on 2 July.*

(d) *Valid at 18 UTC on 3 July, initialized at 00 UTC on 3 July.*

(e) *Valid at 21 UTC on 3 July, initialized at 00 UTC on 3 July.*

Figure 6.11: *Predicted 3h accumulated precipitation valid at 18 UTC(a,b and d) and 21 UTC(c and e) on 3 July 2009 from the High Resolution Limited Area Model(HIRLAM) with 12 km resolution. Based on initializations from 18 UTC on 1 July(a), at 18 UTC and 21 UTC on 2 July in (b) and (c), and at 18 UTC and 21 UTC on 3 July in (d) and (e). Precipitation varies from 0-4 mm. Retrieved from The Norwegian Meteorological Institute, Jan-Inge Hansen.*

6.3 The visualization

6.3.1 Trajectories

To trace the airmasses, trajectory calculation from RIP4 is used. Figure 6.12a, shows trajectories that are calculated backwards from 18 UTC on 3 July to 00 UTC 2 July at low and middle tropospheric levels. Warm air was transferred northwards from southwest, to the west coast of Norway. From here the air was transferred southeast over the mountains and to the Oslo area. To calculate the trajectories further backwards, the HYSPLIT model is used(Figure 6.12b), and here the trajectories are calculated backwards to 00 UTC 25 June. The HYSPLIT calculations are not as accurate as the WRF calculations, and the error is mostly due to the atmospheric data that is used, and not the model itself. Since the trajectories from the WRF model and the HYSPLIT model follow roughly the same track in the start, the HYSPLIT model is used to find the track of the parcel further back in time. From the WRF simulation the trajectories are calculated backwards at 2 different altitudes, and at 3 different altitudes by the HYSPLIT model. In both figures, the red lines are at 8000m, the blue lines are at 5000 m and the green line is at 1000 m.

The air parcels over Southeastern Norway at different altitudes come from three different geographical locations. The air in 5000 m and 8000 m have followed almost the same path from the warm areas in The North Atlantic close to 30°N. The air in the lower levels originate from warm locations in the eastern part of Europe. The air parcels at altitudes lower than 1000 m will be discussed in Chapter 7.

6.3.2 Contributing factors

There are not any operational soundings in Southeast Norway, therefore data from the WRF simulation is used to explore the airmasses in the Oslo area at 18 UTC on 3 July. There are high values of convective available potential energy(CAPE)(6.13a) at 18 UTC 2009, and low values of convective inhibition(CIN)(6.13b) at 12 UTC on 3 July. Both of these values are defined in Chapter 2. There are CAPE values between 400 and 600 J/kg. And this amount of CAPE at these latitudes is enough to produce thunderstorms according to Rasmussen (1998). In most places in South Norway, the CIN values are lower than 20 J/kg. A CIN value greater than 100 J/kg significantly inhibiting convective potential(Wallace and Hobbs, 2006). This means that the CIN values in this case, permit thunderstorms in the Southeast Norway.

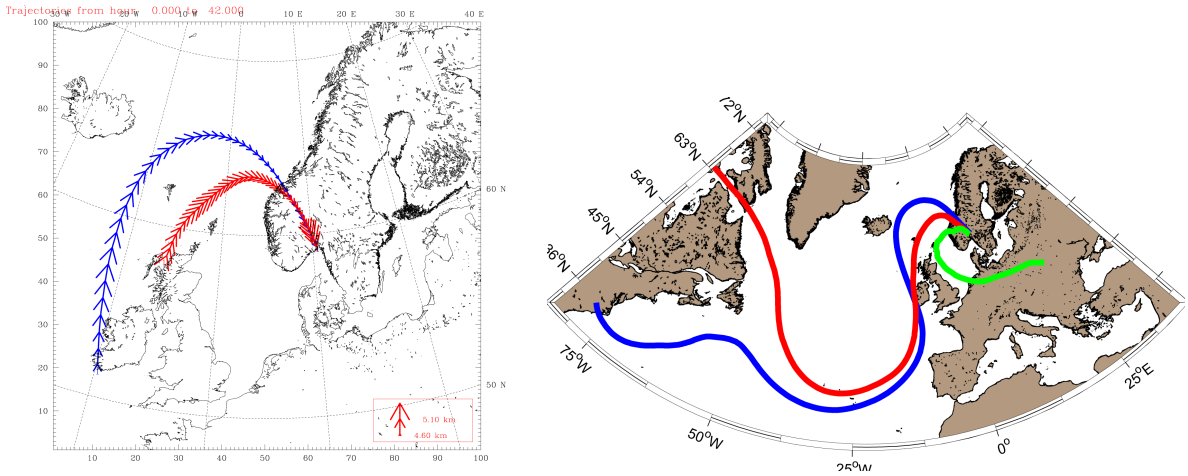

(a) *Trajectories, WRF model.* **(b)** *Trajectories, HYSPLIT model.*

Figure 6.12: *Trajectories calculated backward from 18 UTC 3 July 2009. Trajectories calculated with the WRF model in (a) with beginning time at 00 UTC 2 July 2009, and trajectories from the HYSPLIT model in (b) with beginning time at 00 UTC 25 June 2009. The red line is at 8000 m, the blue line at 5000 m and the green line at 1000 m.*

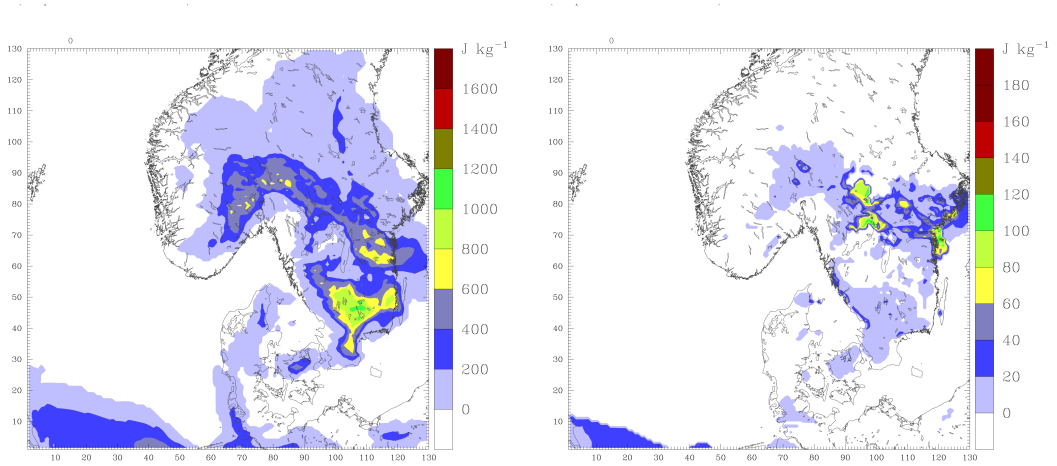

(a) *CAPE, valid at 18 UTC.* **(b)** *CIN, valid at 12 UTC.*

Figure 6.13: *Values of convective available potential energy(CAPE)[J/kg] and convective inhibition(CIN)[J/kg] on 3 July 2009. Both with the WSM3 microphysical parametrization and the Kain-Fritsch scheme activated. Produced with WRF.*

The mixing ratio for the Southeast Norway are high. At 850 hPa(Figure 6.14b), is greater than 7 g/Kg, which is a high amount of moisture.

There are also other factors that contribute to thunderstorms, specially the stability of the atmosphere. For rising air, the potential temperature on the ground must

be higher than the potential temperature of the air aloft. Since the 3 July was a very warm day and the temperature on the ground was nearly 30°C, it can be assumed that the lower part of the atmosphere was in an unstable condition. The simulated precipitation, shown in Figure 6.14a, shows the accumulated 6h precipitation at 18 UTC on 3 July. The precipitation varies from 0 mm to 12 mm, and in general this simulated precipitation is less than the maximum observed.

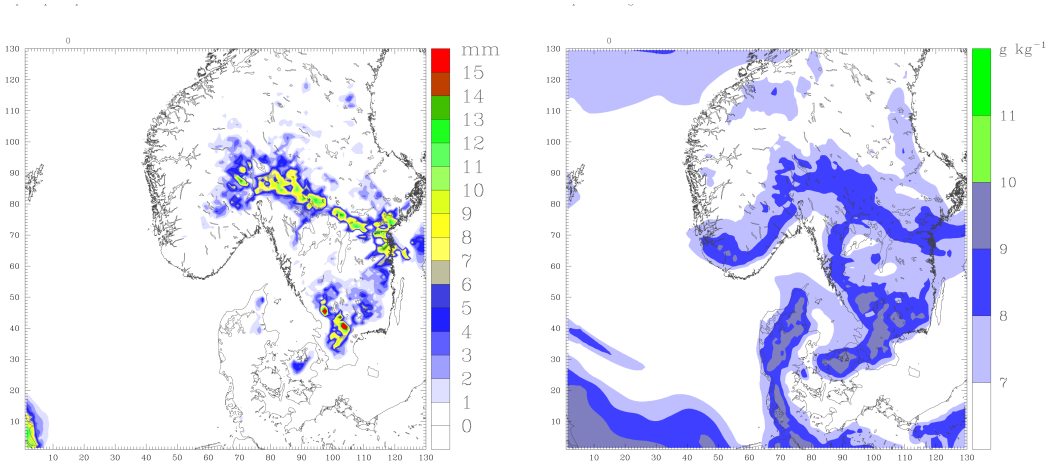

(a) *Accumulated 6h precipitation at 18 UTC.*

(b) *Mixing ratio at 850 hPa at 15 UTC.*

Figure 6.14: *Accumulated 6h Precipitation[mm] valid at 18 UTC on 3 July 2009 in (a) and the mixing ratio[g/kg] valid at 15 UTC on 3 July 2009 at 850 hPa in (b). Both with the WSM3 microphysical parametrization and the Kain-Fritsch scheme activated. Produced with WRF.*

6.4 Configuration of the simulations

6.4.1 Microphysical schemes

To test different configurations of the WRF model, 7 different microphysical schemes are used. In Chapter 4, an explanation of every scheme is given. All of these have been tested with 27 km, 9 km, 3 km and 1 km resolution to see which of them gives the best result. Observations from 45 different precipitation gauges in the Oslo area have been used to compare the observed precipitation with the simulated. Information on the precipitation gauges can be found in Appendix D. An average of all the observed precipitation and all of the simulated precipitation for all of the 7 schemes are compared in Figure 6.15. When comparing the model data with observations, the position of the model grid is important. Since the model data represent big areas,

there will be some errors when comparing the rain gauge point measurement with the precipitation produced by the model(Yates et al., 2006). This type of error is greatest at low horizontal resolutions.

All the schemes that includes ice-phase processes give precipitation in all the runs, but generally none of the simulations gives a very good result. The Kessler scheme is a warm cloud scheme and does not include mixed-phase processes. It is also the one and only scheme that not includes ice-phase processes. This scheme gives the absolute worst results for all the resolutions. From the theory, schemes with mixed-phase processes should be used for grid size less than 10 km. The results in this study gives no indication of that. In fact, the WSM3 scheme gives the best result at all the different resolutions, and this scheme does not include mixed-phase processes. The WSM5 scheme is the other scheme that not takes the mixed-phase processes into account, but this scheme does not produce as much precipitation as the WSM3 scheme. The WSM6 and Eta GCP schemes have ice-phase processes and mixed-phase processes taken into account, but give still a quite bad result at all the different resolutions. The Purdue-Lin scheme and the Thomson schemes include ice-phase and mixed-phase processes. These schemes gives nearly the same amount of precipitation as the WSM3 at the 27 km and the 9 km resolution.

The amounts of precipitation from the 3 km run for all these schemes are shown in Figure 6.16. This shows that much of the precipitation produced by the model is not located where the highest amount of precipitation was observed in the Oslo area. The amount of precipitation is also generally too low.

6.4.2 Cumulus schemes

In WRF, there are 4 different cumulus schemes. Here, all off these schemes are tested in the 27 km and the 9 km run with the WSM3 microphysical parametrization activated to see which of them that gives the best result. The cumulus schemes are not tested on smaller grids because the cumulus schemes should not be used on grids smaller than 5 km(Skamarock et al., 2008). A mean of all the observed precipitation and all of the simulated precipitation from 45 different stations for every 4 schemes is compared in Figure 6.17.

When the cumulus schemes are activated together with the microphysical scheme WSM3, this study has shown that the WRF model produces more precipitation. For the Grell3 scheme this is not the case. The reason can be that the Grell3 scheme is a

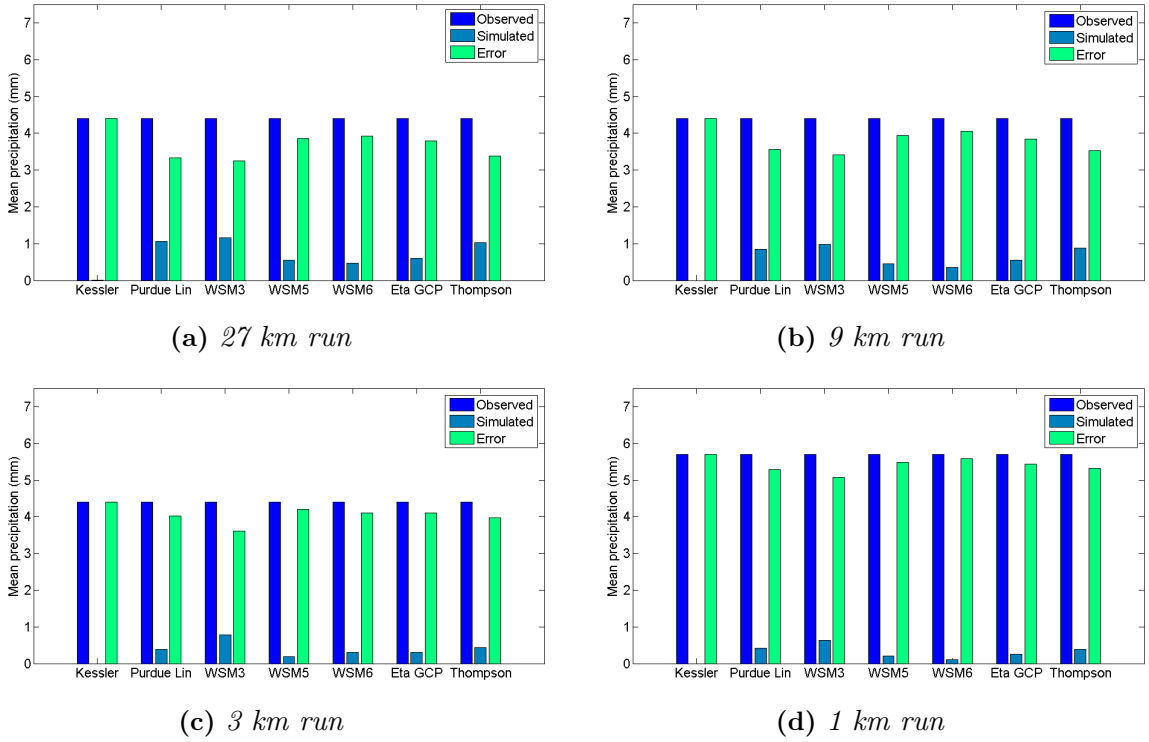

(a) *27 km run* **(b)** *9 km run*

(c) *3 km run* **(d)** *1 km run*

Figure 6.15: *Mean observed precipitation(dark blue column) and mean simulated precipitation(blue column) from the WRF model between 06 UTC on 3 July and 06 UTC on 4 July, 2009, for 7 different microphysical schemes with 27 km, 9 km, 3 km and 1 km resolution. Green column is the difference between the observed and the simulated precipitation(Observed - Simulated). The observations is based on data retrieved from The Norwegian Meteorological Institute for 45 different stations.*

new, not well tested scheme that allows subsidence effects to be spread out to other grid columns. This method is then more suitable for small grid sizes(less than 10 km)(Skamarock et al., 2008). The Grell3 scheme produces nearly the same amount of precipitation in the 27 km and the 9 km run, and not a higher amount of precipitation than without the cumulus scheme. The Grell Devenyi scheme is a mean of different variants of different schemes. This will highly influence the result from this scheme by not producing the highest amount of precipitation, and not producing the lowest amount of precipitation. The Kain-Fritsch scheme and the Betts-Miller-Janjic scheme produce more precipitation in the 27 km run, than in the 9 km run. Overall, the Kain-Fritsch scheme produces more precipitation than the Betts-Miller-Janjic scheme.

The result of the produced precipitation by WRF can be seen in Figure 6.14a. Compared to the results when only the WSM3 microphysical scheme was used, it is easy to see that these cumulus schemes produce more precipitation. To give an overview

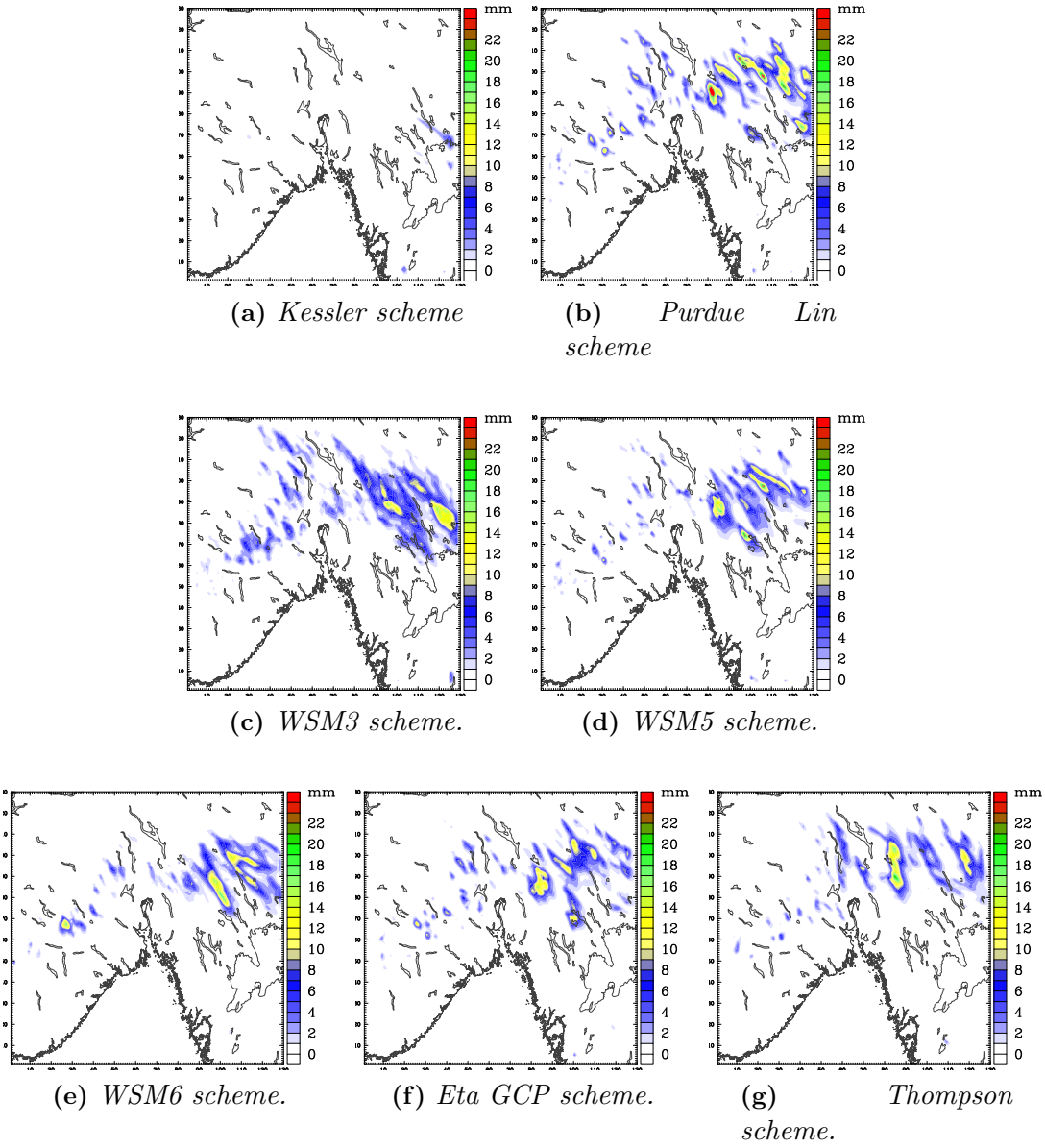

(a) *Kessler scheme* **(b)** *Purdue Lin scheme*

(c) *WSM3 scheme.* **(d)** *WSM5 scheme.*

(e) *WSM6 scheme.* **(f)** *Eta GCP scheme.* **(g)** *Thompson scheme.*

Figure 6.16: *Accumulated 6h precipitation[mm] for 7 different microphysical schemes, valid at 00 UTC 4 July. Produced with the the WRF model with a 3 km resolution.*

of the accuracy of the 27 km model run with the Kain-Fritsch scheme, Figure 6.18 shows the results from all the 45 different stations. In general, the model produces some precipitation at nearly all the stations, but generally, the WRF produces the precipitation at the wrong locations. Where the highest amount of precipitation is observed, the model produces nearly nothing. Further inland, where there is observed less precipitation, the model produces higher amounts of precipitation.

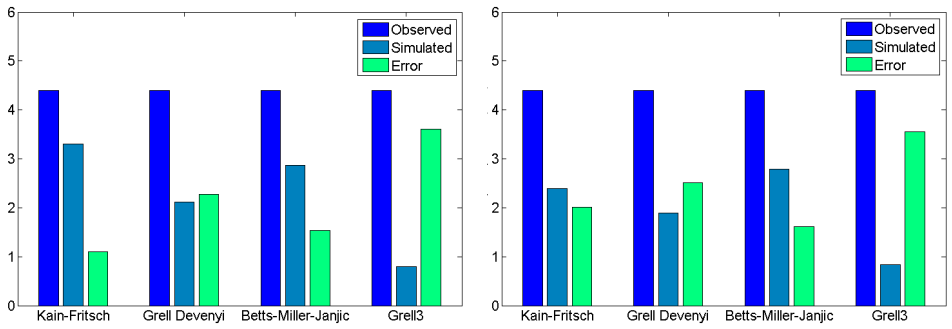

(a) *27 km run.* **(b)** *9 km run.*

Figure 6.17: *Mean observed precipitation(dark blue column) and mean simulated precipitation(blue column) from the WRF simulation between 06 UTC on 3 July and 06 UTC on 4 July, 2009, for 4 different cumulus schemes with 27 km and 9 km resolution. The green column is the difference between the observed and the simulated precipitation(Observed - Simulated). The data is retrieved from The Norwegian Meteorological Institute for 45 different stations.*

6.5 Conclusions

On 3 July 2009, a thunderstorm hit Oslo. There was warm air in the lower, middle and upper troposphere after a long period of warm and dry weather. Several factors derived from the WRF simulation, such as CAPE, CIN, moisture quantity and atmospheric stability indicate a thunderstorm. The temperature difference of 43.4°C between 1000 and 500 hPa is 5.4°C higher than the requirement to produce a thunderstorm.

The WRF model microphysical parametrizations were not good in predicting the amount of precipitation from afternoon summertime showers, and the WSM3 scheme was the most accurate scheme for the microphysical parametrizations. When activating the different cumulus schemes, the model produces a significantly higher amount of precipitation, exept the Grell3 scheme. In general, The Kain-Fritsch scheme gives the most accurate result, and therefore when simulating afternoon summertime showers, this study indicate that cumulus schemes should be used to increase the accuracy of the results.

For both the microphysical and the cumulus schemes, resolution with grid size of 27 km produce more precipitation than model runs with smaller grid size. The model has a tendency in this case to produce the highest amount of precipitation inland, and not where the highest amount is observed.

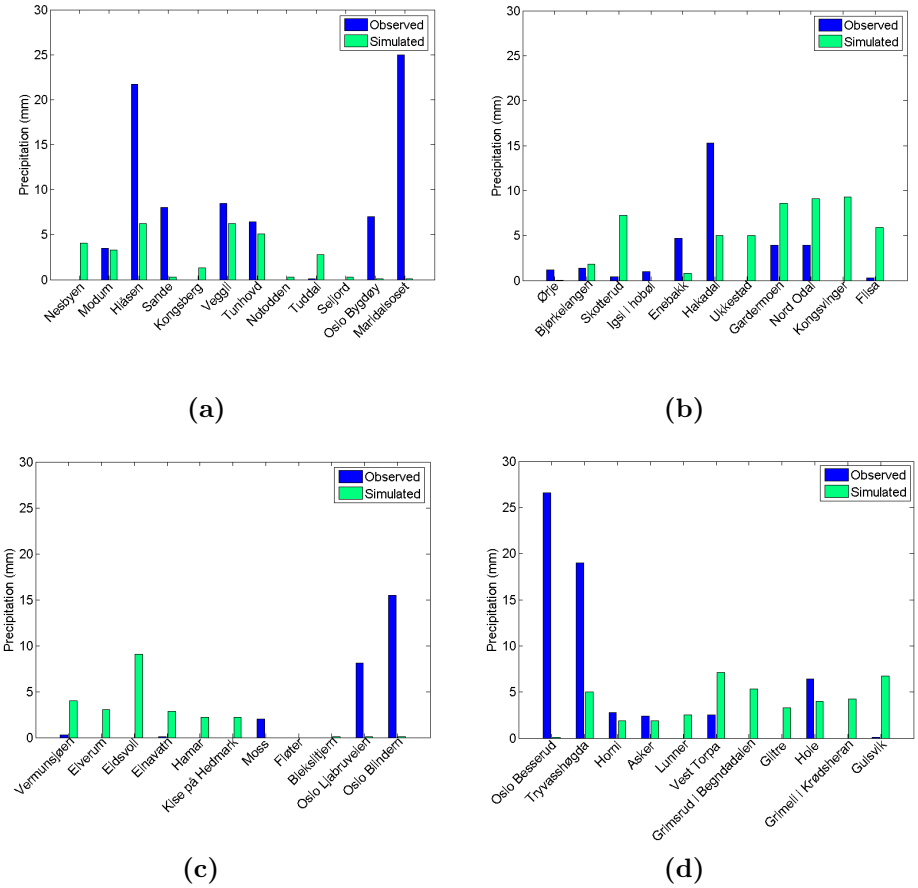

Figure 6.18: *The dark blue column shows the observed precipitation from 06 UTC on 3 July to 06 UTC on 4 July 2009, and the green column shows the accumulated 24h precipitation[mm] at 06 UTC on 4 July 2009 produced with WRF. The Kain-Fritsch scheme and the WSM3 microphysical scheme are activated for 45 different stations in the Oslo area, and the horizontal resolution is 27 km.*

Chapter 7

Predictability analysis

To explore the predictability of the event, 6 simulations with different initial times are run over a large domain with a grid size on 27 km. The simulation domain is large to limit as much as possible information from the lateral boundaries after initialization to reach the area of interest. The figures in this chapter are zoomed in to give better overview of the area this study is focusing on, but the actual domain of the simulations shown in Figure 7.1. The initial times are at 00 UTC from 28 June 2009 to 00 UTC on 3 July 2009. The precipitation in the Oslo area on 4 July was only from convection, shown earlier from satellite pictures. Since the precipitation does not fall over the area at exactly the same time, and the time resolution of the observations are a limiting factor, the total accumulated 24h precipitation at 06 UTC 4 July is used to compare observed and simulated precipitation.

7.1 The GOOD and the BAD run

Figure 7.2 shows the total accumulated 24h precipitation at 06 UTC on 4 July produced by the model for 6 different lead times, together with the observed precipitation in the same period at Blindern(Oslo). The dotted line is the observed precipitation, and the filled line is the precipitation produced by the model. Only one simulation, with a initial time at 00 UTC on 30 June, produces a high amount of precipitation, nearly the same as observed. The simulation initialized 24 hours later at 00 UTC on 1 July, produces much less precipitation. From now on in this study, these two simulations are referred to as the GOOD and the BAD simulations(Figure 7.3). Note that the GOOD forecast from the model is initialized one step further back in time than the BAD forecast. The GOOD is in other words a 96 hours forecast, while the BAD is a 72 hours forecast.

Figure 7.1: *The domain with 27 km resolution used for all the figures in the predictability analysis.*

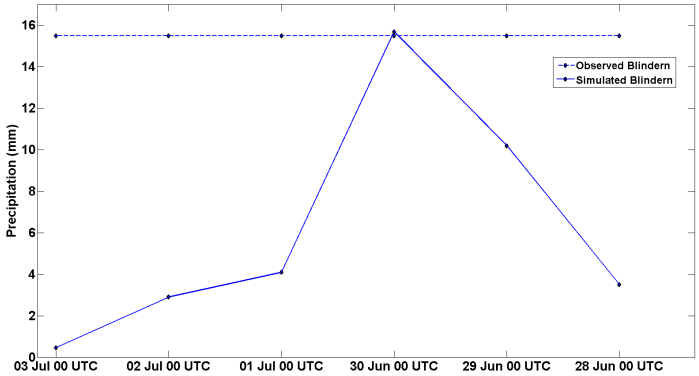

Figure 7.2: *Total accumulated 24h precipitation[mm] at 06 UTC 4 July 2009 produced by the WRF model(filled line) at that lead time, shown together with the observed precipitation at Blindern in Oslo(dotted line). The 6 different lead times are from 00 UTC on 28 June to 00 UTC on 3 July 2009.*

The precipitation produced by WRF goes from approximately 15 mm in the GOOD simulation to approximately 4 mm in the BAD simulation. In the sections below, this big difference in GOOD and BAD will be systematically explored to assess the differences in the two simulations.

7.2 Soundings and trajectories

In order to explore the difference in the output of the two simulations, the airmasses in the simulations are compared and traced back in time. The vertical profile of the

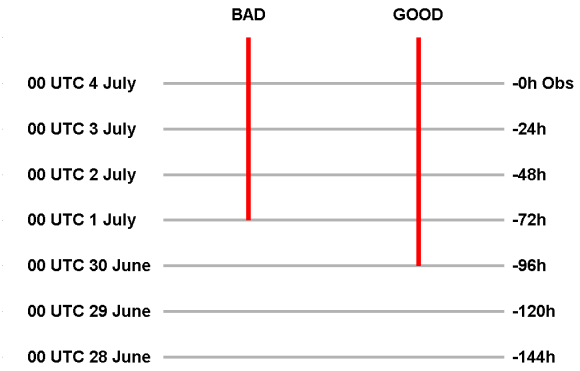

Figure 7.3: *A schematic that shows the initial time for the GOOD and the BAD run for the period from 00 UTC on 28 June to 00 UTC on 4 July 2009.*

atmosphere in the two simulations (GOOD and BAD) are compared in the region where the extreme precipitation over Oslo took place at 15 UTC on 3 July, shown in Figure 7.4. The CAPE differs and indicates a higher probability of convective showers in GOOD, where the GOOD simulation has a CAPE of 338 J/kg, while in the BAD the CAPE value is 194 J/kg. There are only small differences in the temperature, but a much greater difference in humidity at low levels(lower than 750 hPa). The amount of humidity is higher in the GOOD simulation than in the BAD simulation, and the biggest difference is observed at around 500 m above ground level. The water vapour mixing ratio at 500 m above sea level is shown for the GOOD and the BAD simulations together with the difference field(Figure 7.5). Over Oslo and large areas to the south, southeast and west, the GOOD simulation has approximately 1.5-2.5 g/kg more water vapour than the BAD simulation, shown with blue color in Figure 7.5c.

To assess the origin of this difference in humidity, we trace the low level airmasses back in time. Figure 7.7 shows the trajectories from both simulations, calculated backwards from 3 July 18 UTC at 500 meters above ground level in the Oslo area, and back to 18 UTC on 2 July.

In the BAD simulation, the low level airmass has undergone much descending motion over the mountains in South Norway on 2 July. The airmass in the GOOD simulation has not experienced that amount of downward motion and the low level air is therefore more humid than in the BAD simulation. The downward motion in the BAD simulation is associated with the surface flow blowing downhill from the mountains in South Norway. This can clearly be seen in the vertical cross section(Figure 7.8), that shows the vertical circulation at 18 UTC on 2 July. The cross section that is used is

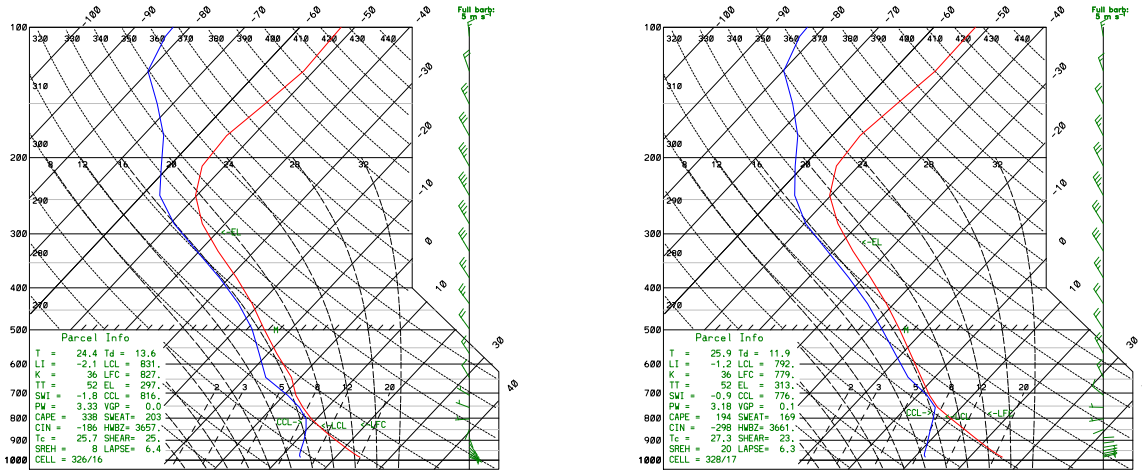

(a) *GOOD* **(b)** *BAD*

Figure 7.4: *Soundings from Fornebu(Oslo) valid at 15 UTC on 3 July 2009 for GOOD in (a), and for BAD in (b). The blue line is the dew point temperature and the red line is the actual temperature. A wind barb on the right side shows the horizontal wind, and parcel information is given in the box to the left. Produced with WRF.*

shown in Figure 7.6 as a red line.

7.3 Mean sea level pressure differences

An obvious question will then be: What drives this downhill flow in BAD? A comparison of the mean sea level pressure(MSLP) in the two simulations, shown in Figure 7.9, shows that the BAD simulation has about 1 hPa higher pressure than the GOOD simulation over Skagerrak.

The maximum difference between these two simulations at 18 UTC on 2 July is located over Western Jutland. This anomaly can be traced back to the Kattegat region, where it appears in the evening of the 1 July(Figure 7.10). The fact that the anomaly can not be traced back to the initial time of the BAD simulation indicates that there is a process in the model that enhances the differences between the two simulations. In other words a small (and practically non-detectable) difference in the initial state grows to be significant in only one and a half day.

Comparing the profiles of the airmasses in the Kattegat region at 00 UTC on 2 July reveals that the BAD simulation is slightly colder (about 1-2°K) in the layer between roughly 600 and 900 hPa(Figure 7.11). This cold air gives a too high sea-level pres-

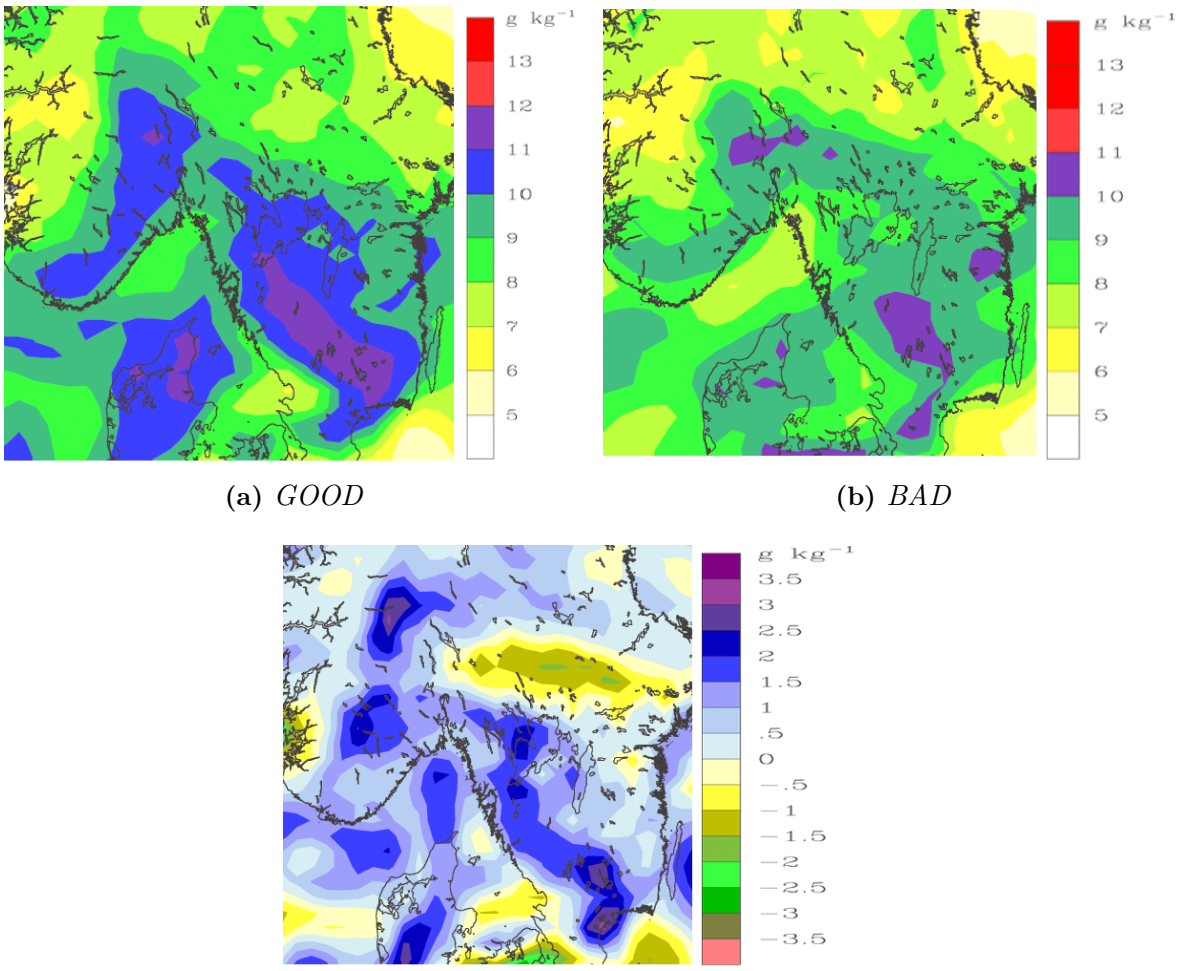

(a) *GOOD* **(b)** *BAD*

(c) *GOOD-BAD*

Figure 7.5: *Water vapour mixing ratio[g/kg] in 500 m height. (a) shows for the GOOD simulation, (b) shows for the BAD simulation and (c) shows the difference field between the GOOD and the BAD simulation(GOOD-BAD). All valid at 18 UTC 3 July 2009. Produced with WRF.*

sure. The GOOD simulation has a positive CAPE of 148 J/kg while in the BAD simulation, the CAPE is zero. This is mainly due to more humidity in the GOOD simulation.

The temperature difference in the two simulations arises in the evening of 1 July, and the GOOD simulation has substantially more precipitation over South Sweden on 1 July. It is then very attempting to attribute the temperature difference to the release of latent heat in the lower to middle troposphere, giving heating of air that is advected slowly to the Kattegat region. There was indeed considerable precipitation over South Sweden on 1 July, but it is not clear whether the GOOD simulation did

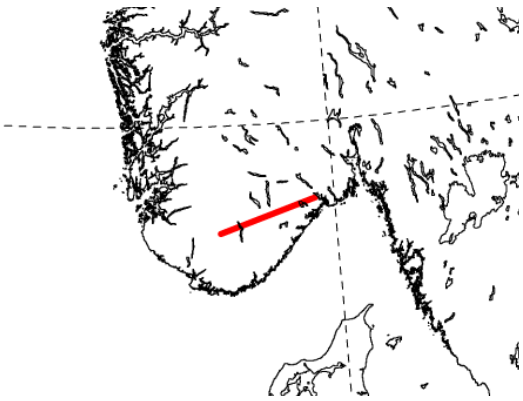

Figure 7.6: *The red line shows the cross section used in the vertical wind sections. Produced with WRF.*

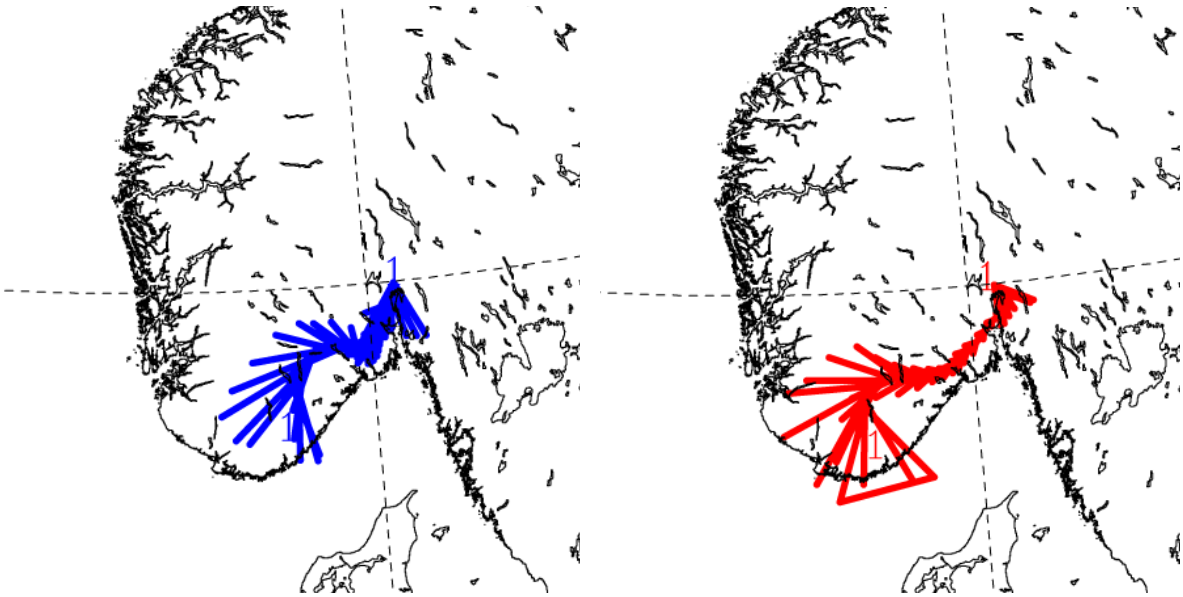

(a) *GOOD* **(b)** *BAD*

Figure 7.7: *Trajectories calculated backwards from 500 m above ground level at 18 UTC on 3 July 2009 over Oslo and back to 18 UTC on 2 July 2009.*

better predicting that precipitation.

7.4 Conclusions

It appears that the BAD simulation gave too little precipitation over the Oslo region on 3 July because it had too dry air that was due to too much descent over the mountains of South Norway. The descent was due to too high sea level pressure over Skagerrak and this pressure anomaly can be traced to too cold air over Kattegat.

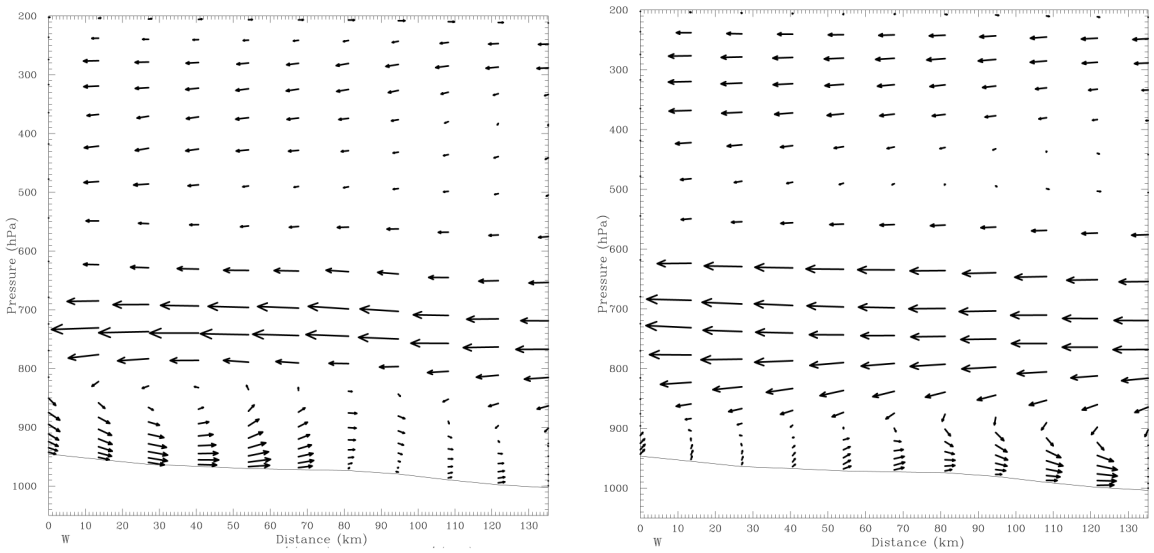

(a) *GOOD* **(b)** *BAD*

Figure 7.8: *Vertical wind field from a chosen cross section between the western point (58.71°N,7.32°E) and the eastern point(59.08°N,9.55°E) for the GOOD(a) and the BAD(b) simulations. Valid at 18 UTC 2 July 2009.*

This air may have been too cold because of too little release of latent heat over South Sweden on 1 July, but that remains quite speculative.

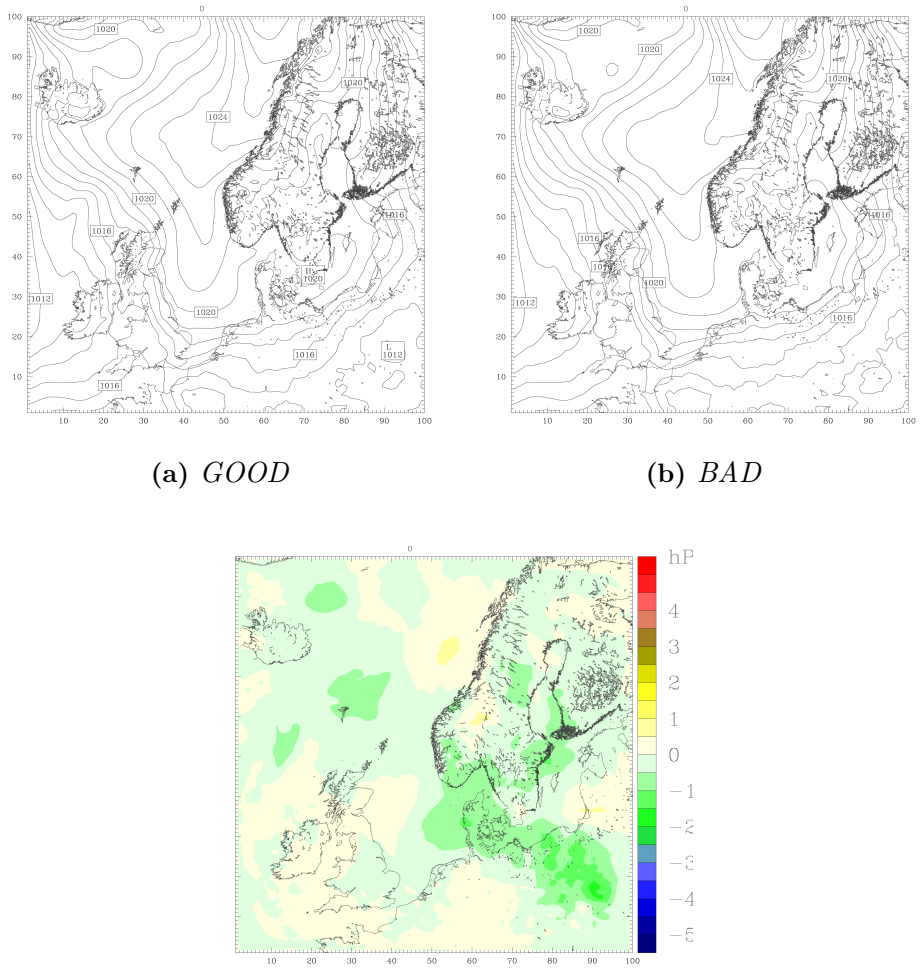

(a) *GOOD* **(b)** *BAD*

(c) *GOOD-BAD*

Figure 7.9: *Mean sea level pressure[hPa] at 18 UTC on 2 July 2009. In (a) the field for the GOOD simulation, in (b) the field for the BAD simulation and in (c) the difference field between the GOOD and the BAD simulation(GOOD-BAD).*

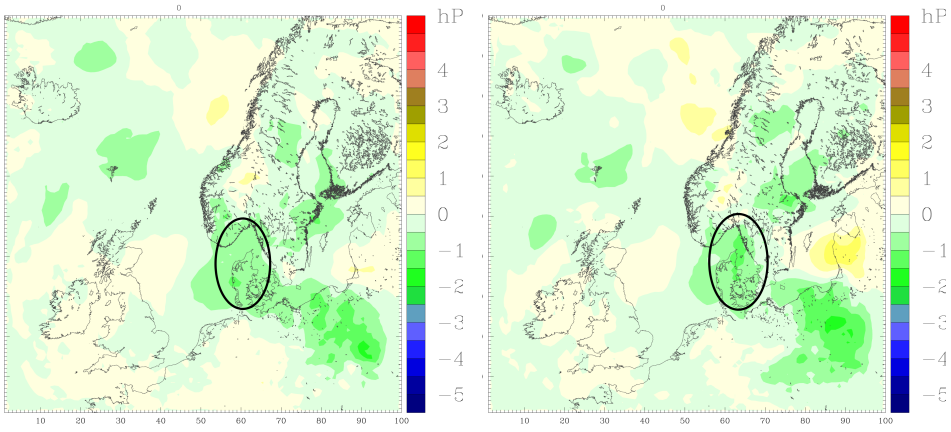

(a) *GOOD-BAD at 18 UTC 2 July.*

(b) *GOOD-BAD at 12 UTC 2 July.*

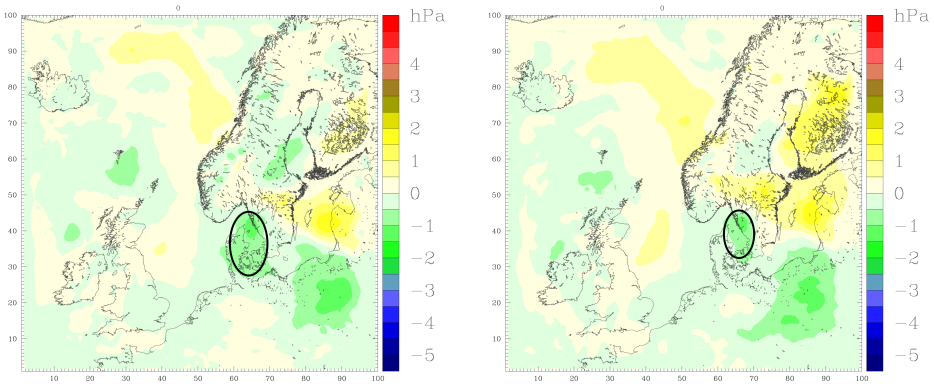

(c) *GOOD-BAD at 06 UTC 2 July.*

(d) *GOOD-BAD at 00 UTC 2 July.*

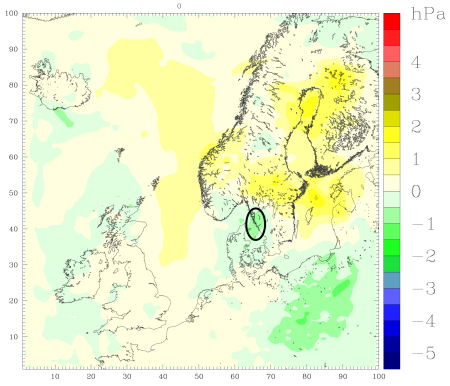

(e) *GOOD-BAD at 18 UTC 1 July.*

Figure 7.10: *Mean sea level pressure difference field[hPa] between GOOD and BAD(GOOD - BAD) from 18 UTC on 2 July to 18 UTC 1 July 2009. The black circle shows the anomaly where BAD has higher pressure than GOOD.*

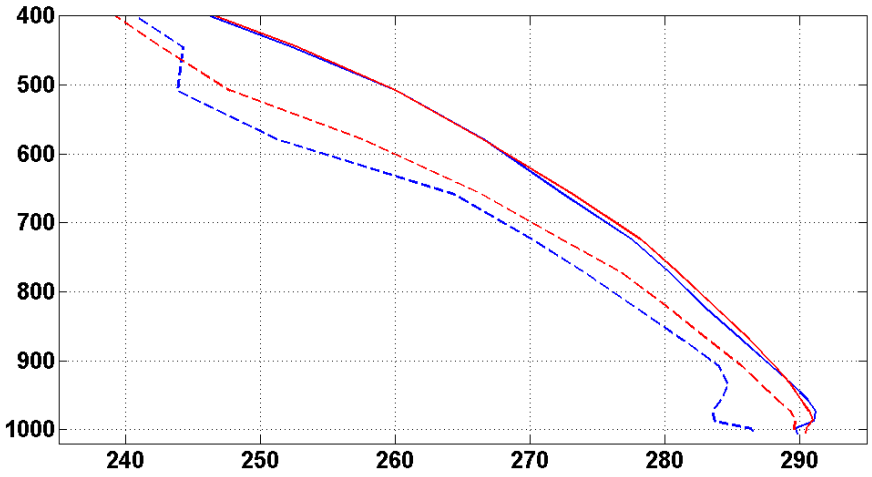

Figure 7.11: *Dew point temperature(dotted lines) and temperature(filled lines) for the GOOD(red) and the BAD(blue) simulations, valid at 00 UTC on 2 July at Landvetter(Gothenburg).*

Chapter 8

Summary

Investigation of the synoptic weather observations in Norway in time and space shows a higher appearance of thunderstorms at low latitudes than at higher latitudes. In the Southeastern part of Norway, thunderstorms are generally observed in the summer months. The study of the diurnal variability indicates that summertime afternoon convection is the main reason for thunderstorms. In the western part of Norway, there is high frequency of thunderstorms throughout the whole year, but inland most of the thunderstorms are observed in the summer months. The west-coast thunderstorms are associated with extratropical cyclones in the autumn and winter or with cold air outbreaks from the north. In the summer months, afternoon convection is important. Apart from the mountains at the west coast, the mountainous areas of South Norway have very few thunderstorms in the winter and autumn, but in the summer there are some observations of thunderstorms due to afternoon convection. Further north, the coastal areas have the same pattern as the west coast, but lower frequency. Inland, most of the thunderstorms are due to afternoon convection in the summer.

A detailed case study of the 3 July 2009 thunderstorm in Oslo shows that the WRF simulations have several factors that indicate high probability of a thunderstorm, such as the positive CAPE and favourable CIN. To investigate different model configurations, a study is done for 7 microphysical parametrizations and 4 cumulus schemes. In general, all the schemes produce too little precipitation, but the model produces a higher amount of precipitation when any of the cumulus schemes is activated, except the Grell3 scheme. The Kain-Fritsch cumulus scheme was most accurate, but still the model produce too little precipitation and much of it at wrong locations. This study indicates that cumulus schemes should be used when simulating summertime afternoon convective storms. It should be underlined that this result is not neces-

sarily a general result for every convective event. A resolution of 27 km was more accurate than model runs with smaller grid size. When the cumulus schemes were not activated, the WSM3 parametrization simulates the highest amount of precipitation. It is not clear whether the error comes from the WRF simulation or the initial or boundary data that is used.

A study on the predictability of the event highlights that the difficulty of simulating an event of this kind. However, in this case, a 96 hour forecast managed to reproduce almost the same amount of precipitation as observed in the Oslo area. The forecast 24 hours later had drier airmasses and it did not reproduce the same amount of precipitation. This error can be traced back to a descent over the mountains in South Norway because of high pressure over Skagerrak and too cold air over Kattegat, that may be due to errors in the production of latent heat over South Sweden on 1 July.

Chapter 9

Future work

A continuation of the exploration the spatial and temporal variability of thunder should include data from automatic detection systems that have been in operation in recent years. This data needs to be processed and made available for the research community. Data from neighbouring countries should also be included. A systematic analysis of the airflow during observations of thunder may reveal a connection between weather systems and thunderstorms.

There are several methods of comparing simulated and observed precipitation, such as comparing at every individual observation site. Some of these methods may contribute to a more complete evaluation of the performance of the numerical simulations. The predictability of the 3 July 2009 case indicated strong sensitivity to the airflow the preceding days. In order to simulate this airflow accurately, more detailed observations are needed. It is in fact of some concern that there are no regular and available observations of the vertical profile of the atmosphere in Southeast Norway. New technology will hopefully provide such observations.

Appendices

Appendix A

An overview of acronyms

CAPE - Convective available potential energy

CAPS - The Center for Analysis and Prediction of Storms

CB - Cumulonimbus cloud

CCL - Cloud condensation level

CIN - Convective Inhibition

ECMWF- The European Center for Medium Range Weather Forecast

ESRL - The Earth System Research Laboratory

FAA - Federal Aviation Administration

HYSPLIT- HYbrid Single-Particle Lagrangian Integrated Trajectory Model

LCL - Lifted condensation level

LFC - Level of free convection

LI - Lifted Index

MET - The Norwegian Meteorological Institute

MSLP - Mean Sea Level Pressure

NCAR - The National Center for Atmospheric Research

NCEP - National Centers for Environmental Prediction

NMM - The Nonhydrostatic and Mesoscale Model

NOAA - The National Oceanic and Atmospheric Administration

RIP4 - Read/Interpolate/Plot

RH - Relative humidity

SMHI - The Swedish Meteorological and Hydrological Institute

WPS - The Weather Research and Forecasting Model preprocessing system

WRF - The Weather Research and Forecasting Model

WSM3 - The Weather Research and Forecasting Model single moment 3-class scheme

WSM5 - The Weather Research and Forecasting Model single moment 5-class scheme

WSM6 - The Weather Research and Forecasting Model single moment 5-class scheme

Appendix B

Station list with synoptic observations of thunderstorms

Table B.1: *A list of all the synoptic stations with latitude and longitude, and information of thunderstorm appearance from 1960-1990 for three annual periods. The three periods are January to April, May to August and September to December. Acquired from The Norwegian Meteorological Institute through http://www.eklima.no, by using a MATLAB script retrieved from Asgeir Sorteberg.*

				Observed thunderstorms		
Station number	Name	Latitude	Longitude	Jan to Apr	May to Aug	Sept to Dec
92700	Loppa	70.33	21.46	2	9	3
93700/93710	Kautokeino	68.99	23.03	0	135	2
94500	Fruholmen Fyr	71.09	23.99	2	14	1
94700	Helnes Fyr	71.06	26.23	0	11	3
96400	Slettnes Fyr	71.08	28.21	2	20	9
96800	Rustefjelbma	70.40	28.20	0	132	4
97250	Karasjok	69.46	25.49	0	165	3
98400	Makkaur Fyr	70.70	30.06	3	19	6
98550	Vardø	70.36	31.08	2	39	6
88900	Gibostad	69.35	18.06	9	23	7
89350	Bardufoss	69.05	18.54	5	88	5
90450	Tromsø	69.65	18.92	16	34	15
90800	Torsvåg Fyr	70.24	19.50	16	14	20
91750	Nordreisa	69.74	21.02	4	52	7
80100	Nord-Solvær	66.36	12.64	9	14	3
80610	Myken	66.76	12.48	26	35	22
82290	Bodø	67.27	14.43	98	60	91
85380	Skrova Fyr	68.15	14.65	8	15	22
86520	Kleiva i Sortland	68.64	15.28	24	20	19
86760	Bø i Vesterålen	68.63	14.46	9	10	15
87110	Andøya	69.29	16.14	45	29	41
69100	Værnes	63.45	10.93	11	197	24
75410	Nordøyan Fyr	64.79	10.54	16	28	25
75600	Leka	65.09	11.70	16	100	30
10400	Røros	62.56	11.38	0	144	0
71540	Ørlandet	63.68	9.6	53	128	75
59800	Svinøy Fyr	62.32	5.27	49	40	64
60500	Tafjord	63.23	7.41	3	20	0
60990	Vigra	62.56	6.11	221	29	184
52860	Takle	61.02	5.38	64	91	117
53100	Vangsnes	61.17	6.64	0	35	6
54130	Lærdal	61.06	7.51	2	64	5

Table B.1: *Continued.*

Station number	Name	Latitude	Longitude	Observed thunderstorms		
				Jan to Apr	May to Aug	Sept to Dec
55160	Fortun	61.5	7.70	0	57	3
59100	Kråkenes Fyr	62.03	4.98	77	43	119
48330	Slåtterøy Fyr	59.90	5.07	28	94	108
50300	Kvamskogen	60.39	5.91	68	124	123
50500	Flesland	60.29	5.23	130	213	239
50540	Bergen Florida	60.38	5.33	257	221	326
51670	Reimegrend Voss	60.68	6.74	5	54	5
52530	Hellisøy Fyr	60.75	4.71	75	96	153
44080	Obrestad Fyr	58.65	5.55	32	200	166
44560	Sola	58.88	5.63	47	235	276
45900	Fister	59.17	6.06	52	145	138
46610	Sauda	59.64	6.36	47	139	136
16600/16610	Fokstua	62.11	9.28	0	118	3
700	Drevsjø	61.88	12.0	2	173	8
6040	Flisa	60.61	12.0	2	398	26
7010	Rena	61.15	11.4	1	217	21
24880	Nesbyen	60.56	9.12	0	205	4
25610	Geilo	60.53	8.21	0	64	15
28800	Lyngdal i Numedal	59.90	9.52	4	277	10
4780	Gardermoen	60.20	11.08	2	510	50
19400	Fornebu	59.89	10.61	9	599	59
17150	Rygge	59.38	10.78	9	524	102
17290	Jæløy	59.43	10.59	2	201	40
27500	Færder Fyr	59.02	10.53	0	207	63
34120	Jomfruland Fyr	58.86	9.59	3	270	88
37230	Tveitsund	50.02	8.52	0	203	21
35860	Lyngør Fyr	58.63	9.15	2	260	112
39040	Kjevik	58.20	8.06	20	307	154

Appendix C

Station list with precipitation observations

Table C.1: *A list of all the precipitation gauges with information of the station number, latitude/longitude and the amount of precipitation[mm] that fell between 06 UTC on 3 July to 06 UTC on 4 July, 2009. Retrieved from The Norwegian Meteorological Institute, through http://www.eklima.no, and from The Swedish Meteorological and Hydrological Institute.*

Station number	Latitude	Longitude	Precipitation
100	61.13	12.50	6.40
180	61.29	12.26	0.30
1080	59.03	11.05	0.10
1130	58.99	11.53	0.10
1230	59.12	11.38	1.50
1400	59.14	11.55	0.50
1650	59.30	11.66	0.10
1950	59.48	11.65	1.20
2610	59.89	11.58	1.40
2650	59.91	11.58	0
2910	59.98	12.13	0.40
3190	59.28	11.11	0.90
3780	59.63	11.04	1
4040	59.75	11.15	4.70
4440	60.09	10.86	15.3
4740	60.17	11.05	0
4780	60.20	11.08	3.90
5223	55.38	12.82	0
5224	55.38	12.81	0
5235	55.57	13.07	0
5343	55.69	13.22	0
5350	60.38	11.56	3.90
5353	55.86	13.66	0
5429	55.48	14.31	0
5590	60.19	12.00	0
6020	60.61	12.01	0.30
6204	56.03	12.76	0
6213	56.22	12.98	0
6226	56.44	12.54	0
6240	56.67	12.92	0
6322	56.37	13.93	0
6328	56.45	13.61	0
6351	56.85	13.88	0.10
6359	56.94	13.06	0
6402	56.01	14.84	0
6403	56.01	14.28	12
6413	56.18	14.85	1.40

Table C.1: *Continued.*

Station number	Latitude	Longitude	Precipitation
6432	56.53	14.90	0
6440	60.69	12.37	0.30
6451	56.84	14.83	0
6611	56.19	16.40	0
6620	60.91	11.59	0
6855	56.92	18.14	0.70
6856	56.92	18.15	0.40
7010	61.15	11.44	0
7138	57.63	11.60	0
7142	57.71	11.99	0
7208	57.11	12.27	0
7209	57.11	12.77	0
7214	57.23	12.70	0
7245	57.76	12.94	9.80
7339	57.64	13.23	7.40
7347	57.80	13.40	5
7348	57.78	13.16	8.70
7430	57.49	14.46	46.7
7442	57.68	14.14	11.2
7524	57.39	15.83	0.90
7525	57.38	15.80	0.70
7552	57.88	15.86	6.40
7616	57.26	16.41	1.40
7642	57.70	16.45	3.30
7660	61.69	11.20	0
7721	57.36	17.09	3.30
7855	57.91	18.95	2.10
7910	62.10	11.04	0
8104	58.05	11.65	0
8105	58.09	11.33	0
8154	58.89	11.00	0
8223	58.35	12.36	3.30
8225	58.44	12.69	0
8236	58.60	12.19	0
8319	58.32	13.04	3.50
8323	58.39	13.84	0.70
8327	58.40	13.44	26.4
8342	58.69	13.11	8.80
8405	58.09	14.40	5.30
8452	58.87	14.39	4.60
8505	58.07	15.23	0.80
8518	58.28	15.23	3.20
8527	58.44	15.37	8.70
8546	58.71	15.03	4.80
8634	58.58	16.15	7.50
8642	58.68	16.31	2.50
8647	58.77	16.12	4.70
8714	58.25	17.01	0.20
8720	61.89	10.14	0
8744	58.74	17.87	4.30
8770	61.97	10.02	0
8923	58.39	19.19	2.70
9213	59.22	12.07	0
9241	59.67	12.63	10.5
9352	59.86	13.11	1.30
9418	59.31	14.10	16.3
9419	59.30	14.89	11
9439	59.66	14.18	3.20
9458	59.93	14.89	10.5
9580	62.26	10.73	0
9600	59.01	16.37	7.90
9604	59.05	16.39	7.20
9619	59.38	16.45	16
9635	59.59	16.60	15.3
9656	59.90	16.68	5.90
9710	59.17	17.91	5.50
9728	59.35	17.52	7.40
9739	59.66	17.92	2
9821	59.34	18.05	3.70
9849	59.83	18.63	0.90
9870	62.43	10.41	0

Table C.1: *Continued.*

Station number	Latitude	Longitude	Precipitation
9927	59.44	19.50	1.70
10219	60.30	12.69	10.3
10308	60.10	12.99	0.20
10310	60.15	13.80	4.50
10341	60.68	13.69	29.2
10458	60.96	14.50	0
10522	60.38	15.14	15.4
10523	60.38	15.23	23.3
10537	60.61	15.66	10.7
10545	60.72	15.01	8
10604	60.09	16.30	9.40
10607	60.14	16.17	10
10616	60.26	16.97	1.60
10657	60.96	16.43	0.30
10714	60.23	17.90	0.10
10742	60.71	17.16	0
10832	60.52	18.37	0.10
11120	60.29	11.16	0
11217	61.27	12.85	0
11414	61.25	14.03	2.20
11436	61.60	14.18	0.30
11441	61.66	14.99	0
11451	61.85	14.09	0
11500	60.70	10.86	0
11522	61.36	15.71	1.50
11643	61.71	16.17	0
11649	61.82	16.54	0.40
11710	60.59	10.64	0.10
11743	61.70	17.52	1.50
11744	61.71	17.08	0.20
12200	60.75	11.20	0
12226	62.45	12.67	0
12233	62.54	12.60	0
12290	60.80	11.09	0
12306	62.09	13.61	1.90
12320	60.81	11.06	0
12334	62.41	13.67	0
12346	62.75	13.84	0
12402	62.01	14.19	2
12411	62.18	14.95	1.20
12430	62.49	14.15	0
12520	60.79	10.95	0
12544	62.75	15.08	0
12550	60.77	10.80	0
12600	60.95	10.68	0
12629	62.49	16.27	0
12680	61.09	10.47	0
12713	62.22	17.74	0.80
12738	62.62	17.94	2.70
12800	61.11	10.67	0
12839	62.64	18.09	4.60
13050	61.27	10.20	0
13310	61.46	10.31	0
13450	61.66	9.976	0
13640	61.51	9.408	0
13670	61.51	9.382	0
13700	61.41	9.534	0
14050	61.67	9.558	0
14550	61.92	9.013	0
14580	61.87	9.092	0
14711	61.81	9.013	0
15430	61.72	8.244	0
15480	61.87	8.467	0
15660	61.90	8.172	0
15730	61.89	7.896	0
15890	62.01	7.663	0.30
16270	61.89	9.471	0
16560	62.07	9.116	0
16610	62.11	9.286	0
16790	62.10	8.919	0
17000	59.15	10.82	0.30

Table C.1: *Continued.*

Station number	Latitude	Longitude	Precipitation
17150	59.38	10.78	0
17251	59.44	10.68	2
17500	59.49	11.01	0
17980	59.84	10.82	8.10
18020	59.87	10.78	0.30
18160	59.87	10.79	6.10
18210	59.92	10.80	0
18269	59.95	10.90	6
18320	59.93	10.75	21.1
18420	59.94	10.79	24.3
18450	59.96	10.79	25
18500	60.05	10.68	16.6
18700	59.94	10.72	15.5
18701	59.94	10.72	19.4
18815	59.90	10.68	7
18920	59.95	10.70	26.6
18950	59.98	10.66	19
18980	59.92	10.63	5.10
19610	59.91	10.46	2.80
19710	59.85	10.43	2.40
20250	60.10	10.29	6.40
20301	60.16	10.24	2.70
21680	60.93	10.03	2.50
23500	61.12	9.063	0.10
23560	61.24	8.855	0
23720	61.12	8.582	0.10
24100	60.13	10.17	0
24210	60.23	9.926	0
24600	60.13	9.597	0
24710	60.38	9.605	0.10
24890	60.56	9.133	0
25100	60.87	8.532	0
25260	60.67	8.278	0
25630	60.53	8.194	0
25830	60.59	7.530	0.10
26161	59.91	9.860	3.50
26240	60.01	9.510	21.7
26380	60.24	9.346	0
26990	59.61	10.21	8
27140	59.41	10.44	5.20
27270	59.27	10.43	0
27301	59.08	10.44	1.10
27450	59.23	10.34	9.70
27600	59.13	10.21	9.50
27770	59.27	10.20	6.50
27800	59.19	9.968	3.50
28922	60.04	9.148	8.50
29600	60.46	8.752	6.40
30000	59.05	10.02	1
30320	59.19	9.589	0
30530	59.55	9.264	0
31080	60.12	8.703	0
31410	59.87	8.576	0
31570	59.81	8.136	4.50
31620	59.83	8.179	0
31660	60.01	7.914	0
31850	59.60	8.713	0
31900	59.74	8.810	0.10
32200	59.45	9.037	0
32320	59.51	8.645	0
32350	59.64	8.376	0
32780	59.14	9.267	2.50
32850	59.40	8.475	0
32890	59.49	8.199	0
33250	59.70	8.036	0
34800	59.14	8.775	3
34900	59.26	8.775	2
35090	58.80	9.099	0
35200	58.88	8.948	0
35340	58.71	9.211	0
36060	58.46	8.759	0

Table C.1: *Continued.*

Station number	Latitude	Longitude	Precipitation
36200	58.39	8.789	0
36490	58.59	8.718	0
37230	59.02	8.520	0
37300	59.16	8.395	0
37500	59.32	8.152	2
37650	59.00	8.273	0
37740	59.16	8.039	7.50
38140	58.34	8.522	0
38380	58.52	8.041	0
38421	58.42	8.289	0
38450	58.51	8.353	0
38600	58.63	8.281	0
38800	58.79	8.234	0
39040	58.20	8.068	0.10
39220	58.21	7.890	0
39690	58.66	7.801	0
40200	59.12	7.510	0
40271	59.23	7.539	0.30
40420	59.35	7.346	1.50
40880	59.59	7.410	0
41200	58.31	7.593	0
41480	58.61	7.407	0
41550	58.78	7.352	0
41670	58.26	7.380	0
41770	57.98	7.047	0
41820	58.13	7.048	0
41860	58.24	6.982	0
42160	58.11	6.568	0
42250	58.28	6.818	0
42520	58.65	6.946	0
42650	58.28	6.649	0
42720	58.41	6.658	0
42810	58.66	6.710	0
42940	58.92	6.909	0.20
42950	58.94	6.919	0
43010	58.50	6.500	0
43360	58.45	6.003	0
43810	58.76	6.369	0
44160	58.69	5.641	0
44300	58.76	5.650	0.10
44480	58.68	5.984	0
44520	58.75	6.014	0
44560	58.88	5.637	0
44610	59.07	5.412	0
44640	58.95	5.730	0
44760	58.90	5.967	0
44800	58.81	5.920	0
44900	58.83	6.056	0
45350	59.05	6.649	0
45600	59.07	6.020	0
45870	59.16	6.036	0
46150	59.47	6.278	0
46300	59.58	6.809	0
46450	59.82	6.825	0
46850	59.55	5.995	0
46910	59.48	5.750	0
47090	59.50	5.625	0
47300	59.30	4.878	0.20
47450	59.65	5.433	0
47600	59.65	5.259	0
47820	59.85	6.282	0
47890	59.85	6.018	0
48250	59.91	5.316	0
48450	59.86	5.769	0
48500	59.99	6.024	0
48780	60.13	6.330	0
49351	60.11	6.560	0
49490	60.31	6.650	0.20
49750	60.42	7.273	0
49800	60.40	7.279	0
50070	60.35	6.274	0.40

Table C.1: *Continued.*

Station number	Latitude	Longitude	Precipitation
50080	60.37	6.192	0
50150	60.04	5.905	0
50310	60.38	5.964	0
50450	60.27	5.331	0
50500	60.28	5.226	0
50540	60.38	5.333	0
51250	60.68	5.964	0
51470	60.64	6.223	0
51530	60.62	6.426	0.40
52170	60.80	6.146	0
52220	60.82	6.264	0
52310	60.85	5.973	0
52400	60.62	5.380	0
52601	60.83	5.583	0
52750	60.84	5.217	0
53160	60.90	6.724	0
53180	60.79	6.692	0

Appendix D

Station list for compared precipitation

Table D.1: *A list of all the precipitation gauges that is used when comparing precipitation produced by the model with the observations, between 06 UTC on 3 July to 06 UTC on 4 July, 2009. Retrieved from The Norwegian Meteorological Institute, through http://www.eklima.no*

Station number	Name	m.a.s.l	Latitude	Longitude
1950	ØRJE	123	59.48	11.65
2610	BJØRKELANGEN II	135	59.89	11.58
2910	SKOTTERUD - BERGSTAD	153	59.98	12.13
3780	IGSI I HOBØL	144	59.63	11.04
4040	ENEBAKK - BARBØL	164	59.75	11.15
4440	HAKADAL - BLIKSRUDHAGAN	174	60.09	10.86
4740	UKKESTAD	187	60.17	11.05
4780	GARDERMOEN	202	60.20	11.08
5350	NORD-ODAL	147	60.38	11.56
5590	KONGSVINGER	148	60.19	12.00
6020	FLISA II	185	60.61	12.01
6440	VERMUNDSJØEN	230	60.69	12.37
6620	ELVERUM - FAGERTUN	230	60.91	11.59
11120	EIDSVOLL VERK	181	60.29	11.16
11710	EINAVATN	406	60.59	10.64
12290	HAMAR II	132	60.80	11.09
12550	KISE PA HEDMARK	128	60.77	10.80
17251	MOSS BRANNSTASJON	32	59.44	10.68
17500	FLØTER	131	59.49	11.01
17780	BLEKSLITJERN	104	59.80	10.63
17980	OSLO - LJABRUVEIEN	92	59.84	10.82
18700	OSLO - BLINDERN	94	59.94	10.72
18920	OSLO - BESSERUD	240	59.95	10.70
18950	TRYVASSHØGDA	514	59.98	10.66
19610	HORNI	81	59.91	10.46
19710	ASKER	163	59.85	10.43
20520	LUNNER	372	60.29	10.58
21680	VEST-TORPA II	542	60.93	10.03
22790	GRIMSRUD I BEGNADALEN	172	60.66	9.74
19930	GLITRE	375	59,86	10,05
20250	HOLE	66	60,10	10,29
24600	GRIMELI I KRØDSHERAD	367	60,13	9,59
24710	GULSVIK II	142	60,38	9,60
24890	NESBYEN - TODOKK	166	60,56	9,13
26161	MODUM - S. KOPLAND	80	59,91	9,86
26240	HIÅSEN	402	60,01	9,51
26990	SANDE - GALLEBERG	60	59,61	10,21
28380	KONGSBERG BRANNSTASJON	170	59,62	9,63
28922	VEGGLI II	276	60,04	9,14
29600	TUNHOVD	870	60,46	8,75
30530	NOTODDEN	34	59,55	9,26
31900	TUDDAL	464	59,74	8,81
32320	SELJORD - LØNNESTAD	162	59,51	8,64
18815	OSLO - BYGDØY	15	59.90	10.68
18450	MARIDALSOSET	173	59.96	10.79

Bibliography

Betts, A. K. (1986). A new convective adjustment scheme. part i: Observational and theoretical basis. *Quarterly journal of the Royal Meteorological Society*, 112(473):677.

Betts, A. K. and Miller, M. J. (1986). A new convective adjustment scheme. part ii: Single column tests using gate wave, bomex, atex and arctic air-mass data sets. *Quarterly journal of the Royal Meteorological Society*, 112(473):693.

Bielec-Bkowska, Z. (2003). Long-term variability of thunderstorm occurrence in poland in the 20th century. *Atmospheric research*, 67:35.

Calwagen, E. G. (1926). Zur diagnose und prognose lokaler sommerschauer. *Geofysiske publikasjoner*.

Comet (2002). Buoyancy and cape. retrieved from: `http://www.meted.ucar.edu/mesoprim/cape/index.htm`. Online accessed: February-2011. The source of this material is the Comet®Website at http://meted.ucar.edu/ of the University Corporation for Atmospheric Research, sponsored in part through cooperative agreements with the National Oceanic and Atmospheric Administration(NOAA), U.S. Department of Commerce(DOC). ©1997-2011 University Corporation for atmospheric research. All rights reserved.

Comet (2009). Blocking patterns. retrieved from: `http://www.meted.ucar.edu/norlat/sat_features/blocking_patterns/`. Online accessed: April-2011. The source of this material is the Comet®Website at http://meted.ucar.edu/ of the University Corporation for Atmospheric Research, sponsored in part through cooperative agreements with the National Oceanic and Atmospheric Administration(NOAA), U.S. Department of Commerce(DOC). ©1997-2011 University Corporation for atmospheric research. All rights reserved.

Cotton, W. R. and Anthes, R. A. (1989). *Storm and cloud dynamics : International geophysics*. International Geophysics Series. Academic Press Inc., San Diego, New York, Berkeley, London, Sidney, Tokyo, Toronto.

Delden, A. v. (2001). "the synoptic setting of thunderstorms in western europe". *Atmospheric research*, 56:89–110.

Didone, M. (2007). Some factors in the design of a regional prediction model: an examination based upon two map events. *Meteorologische Zeitschrift*, 16(3):261.

Draxler, R. R. (1992). *Hybrid single-particle Lagrangian integrated trajectories (HY-SPLIT), Version 3.0: User's guide and model description.*

Draxler, R. R. and Hess, G. D. (1997). *Description of the HYSPLIT4 modeling system.*

Draxler, R. R. and Taylor, A. D. (1982). Horizontal dispersion parameters for long-range transport modeling. *Journal of applied meteorology*, 21(3):367.

Dudhia, J. (1989). Numerical study of convection observed during the winter monsoon experiment using a mesoscale two-dimensional model. *J. Atmos. Sci.*, 46:3077–3107.

Godske, C. L., Bergeron, T., Bjerknes, J., and Bundgaard, R. C. (1957). *Dynamical meteorology and Weather Forecasting.* Am. Met. Soc. Boston.

Grell, G. and Devenyi, D. (2002). A generalized approach to parameterizing convection combining ensemble and data assimilation techniques. *Geophysical research letters*, 29(14):38.

Grzeschik, M., Bauer, H.-S., Wulfmeyer, V., Engelbart, D., Wandinger, U., Mattis, I., Althausen, D., Engelmann, R., Tesche, M., and Reide, A. (2008). Four-dimensional variational data analysis of water vapor raman lidar data and their impact on mesoscale forecasts. *J. Atmos. Oceanic Technol.*, 25:1437–1453.

Haby, J. (2010). The difference between the lcl and ccl. Retrieved from: `http://www.theweatherprediction.com/habyhints/160/`. Online accessed: April-2011.

Hobbs, P. V. (1991). Research on clouds and precipitation: past, present and future. ii. *Bulletin of the American Meteorological Society*, 72(2):184.

Hohenegger, C. (2006). Predictability mysteries in cloud-resolving models. *Monthly weather review*, 134(8):2095.

Holton, J. R. (2004). *An introduction to dynamic meteorology.* International geophysics series. Elsevier academic press, London.

Hong, S.-Y., Dudhia, J., and Chen, S.-H. (2004). A revised approach to ice microphysical processes for the bulk parameterization of clouds and precipitation. *Monthly Weather Review*, 132:103–120.

Hong, S.-Y. and Lim, J.-O. J. (2006). The wrf single-moment 6-class microphysics scheme (wsm6). *J. Korean Meteor. Soc.*, 42:129–151.

Janjic, Z. I. (1994). The step-mountain eta coordinate model: further developments of the convection, viscous sublayer, and turbulence closure schemes. *Monthly weather review*, 122(5):927.

Kain, J. S. (2004). The kain−fritsch convective parameterization: An update. *Journal of Applied Meteorology*, 43(1):170–181.

Kain, J. S. and Fritsch, J. M. (1990). A one-dimensional entraining/detraining plume model and its application in convective parameterization. *Journal of the Atmospheric Sciences*, 47(23):2784.

Kain, J. S. and Fritsch, J. M. (1993). Convective parameterization for mesoscale models: The kain-fritsch scheme, the representation of cumuluc convection in numerical models. *American meteorological society*.

Kessler, E. (1969). On the distribution and continuity of water substance in atmospheric circulation. *American Meteorological Society*, 32:84.

Knudsen, J. (1974). Winter thunderstorms in southern norway. *Meteorologiske Annaler*, 6(9).

Kunz, M. (2009). Recent trends of thunderstorm and hailstorm frequency and their relation to atmospheric characteristics in southwest germany. *International journal of climatology*, 29(15):2283.

Ólafsson, H. and Økland, H. (1994). Precipitation from convective boundary layers in arctic air masses. *Tellus. Series A, Dynamic meteorology and oceanography*, 46(1):4.

Laprise, R. (1992). The euler equation of motion with hydrostatic pressure as an independent variable. *Monthly weather review*, 120(1):197.

Leuenberger, D. and Rossa, A. (2007). Revisiting the latent heat nudging scheme for the rainfall assimilation of a simulated convective storm. *Meteorology and atmospheric physics*, 98(3-4):195.

Lin, Y. L., Farley, R. D., and Kuo, Y.-H. (1983). Bulk parameterization of the snow field in a cloud model. *Journal of climate and applied meteorology*, 22(6):1065.

McIlveen, J. F. R. (1992). *Fundamentals of weather and climate*. Chapman and Hall, London.

Orlanski, I. (1975). A rational subdivision of scales for atmospheric processes. *Bulletin of the American Meteorological Society*, 56(5):527.

Rasmussen, E. N. (1998). A baseline climatology of sounding-derived supercell and-tornado forecast parameters. *Weather and forecasting*, 13(4):1148.

Rogers, R. R. and Yau, M. K. (1989). *A short course in cloud physics*. International Series in Natural Philosophy. Perganmon Press, Oxford.

Rott, G. (1963). *"Luftelektrisches Feld und Wetter"*, volume Vol. 11 of *Geofisica e Meteorologica*. Genova.

Rutledge, S. A. and Hobbs, P. V. (1984). The mesoscale and microscale structure and organization of clouds and precipitation in midlatitude cyclones. xii- a diagnostic modeling study of precipitation development in narrow cold-frontal rainbands. *Journal of the Atmospheric Sciences*, 41(20):2949.

Sibson, R. (1981). A brief description of natural neighbor interpolation.

Skamarock, W. C., Klemp, J. B., Dudhia, J., Gill, D. O., Barker, D. M., Duda, M. G., Huang, X. Y., Wang, W., and Powers, J. G. (2008). A description of the advanced research wrf version 3. NCAR technical note.

Spinnangr, F. (1941). *"On Thunderstorm Forecasting in Western Norway"*. Bergens museums årbok. Bergen.

Spinnangr, G. (1942). On local summer showers in southeast norway. *Meteorologiska annaler*, 1(8):150–205.

Sumner, G. (1988). *Precipitation: process and analysis*.

Thompson, G., Rasmussen, R. M., and Manning, K. (2004). Explicit forecasts of winter precipitation using an improved bulk microphysics scheme. part i: Description and sensitivity analysis. *Monthly weather review*, 132(2):519.

Trentmann, J. (2009). Multi-model simulations of a convective situation in low-mountain terrain in central europe. *Meteorology and atmospheric physics*, 103(1-4):95.

Tuomi, T. J. and Mäkelä, A. (2009). Flash cells in thunderstorms. In Betz, H. D., Schumann, Pierre, U., and Laroche, editors, *Lightning: Principles , Instruments and Applications*, pages 509–520. Springer Netherlands.

Vaidya, S. S. (2007). Simulation of weather systems over indian region using mesoscale models. *Meteorology and atmospheric physics*, 95(1-2):15.

Wallace, J. M. and Hobbs, P. V. (2006). *Atmospheric science, an introductory survey*. International Geophysics Series. Elsevier, Washington, 6 edition.

Wulfmeyer, V. (2006). Four-dimensional variational assimilation of water vapor differential absorption lidar data: The first case study within ihop2002. *Monthly weather review*, 134(1):209.

Yamada, H. (2008). Numerical simulations of the role of land surface conditions in the evolution and structure of summertime thunderstorms over a flat highland. *Monthly weather review*, 136(1):173.

Yates, E., Anguetin, S., Ducrocq, V., Creutin, J. D., Richard, D., and K., C. (2006). "points and areal validation of forecast precipitation fields! *Meteorological Applications*, 13(01):1–20.